Numerical and experimental multi-linear modelling of wave energy devices

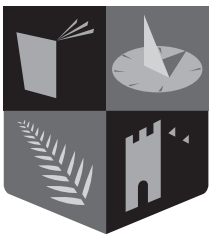

Ollscoil
Mhá Nuad
Ollscoil na hÉireann
Má Nuad

Mahdiyeh Farajvand

A thesis submitted for the degree of
Doctor of Philosophy

Maynooth University

Faculty of Science and Engineering, Electronic Engineering Department
Centre for Ocean Energy Research

September 2024

Head of the department: Prof. Gerard Lacey
Supervisor: **Prof. John V. Ringwood**
Co-Supervisor: **Dr. Demián García-Violini**,
Quilmes University, Argentina.

Contents

Abstract

The escalating demand in global energy requirements and the soaring price of traditional fossil fuels, in combination with global awareness to follow a pathway toward decarbonisation, are fuelling research and development into novel technologies to harness renewable energy sources. Ocean wave energy, a significant and untapped source of renewable energy, if economically viable, can make a promising avenue for sustainable energy generation. In the drive for the development and more efficient operation of wave energy converters (WECs), effective control systems, which can maximise converted energy for a given capital cost, are crucial. Model-based control systems contribute to the majority of energy-maximising control systems of WECs, with a need for a suitable mathematical model. Physics-based models, numerical simulations, full-scale tests, or laboratory-scale tests can be used to develop WEC models, each presenting distinct methodologies and challenges, yielding models with a diverse range of accuracy. The effectiveness of model-based control relies on the precision of the WEC model upon which the controller is based, given that WEC controllers have shown considerable sensitivity to inaccuracies in their underlying models. Among the distinct WEC modelling techniques, the determination of models from data (using either physical or numerical experiments) is an effective route to derive representative (linear and nonlinear) WEC models. In this thesis, both numerical wave tank (NWT) and physical wave tank (PWT) experiments are considered to estimate a range of adequate linear WEC models capable of meeting the requirements of a control system by the employment of the proper test signals (specific to each test setup) to cover the full operational space of the system. Many uncertainty parameters in the data-driven models with sources differing significantly in NWT and PWT experiments, may hinder accurate WEC model determination for efficient (model-based) control strategies. Within this scope, the current study considers the range of tests that can be performed, the uncertainty sources, and the range of post-processing techniques that can be applied in NWT and PWT tests for a point-absorber type system, with an aim to get the most realistic hydrodynamic WEC models. Moreover, in NWT testing, a comprehensive representation of input signal synthesis and characterisation is carried out, to provide sufficient fidelity in Computational Fluid Dynamics (CFD)- based NWT tests and, in PWT testing, specific focus is directed towards the quantification of uncertainty and external disturbance, specifically tailored to the PWT under study, with the corresponding effects are mitigated by applying effective data-processing steps.

Multi-linear hydrodynamic WEC models (obtained either from NWT or PWT testing), serve as a starting point for model-based linear WEC controller synthesis. Finally, with a view to robust WEC control, a (single) nominal model and uncertainty bound are quantified from multi-linear models obtained from NWT tests, and robust control results are provided to demonstrate the efficacy of the modelling and control philosophy.

Declaration of authorship

I, Mahdiyeh Farajvand, declare that this thesis entitled 'Estimation of wave energy model uncertainty bounds in the optimal control of wave energy devices' and the work presented in it are my own. I confirm that:

- This work was done wholly while in candidature for a research degree at this University.
- Where I have consulted the published work of others, this is always clearly attributed.
- Where I have quoted from the work of others, the source is always given. With the exception of such quotations, this thesis is entirely my own work.
- I have acknowledged all main sources of help.

This thesis includes three papers that introduce novel contributions. These papers were co-authored with several collaborators, and I would like to clarify the specific roles of each contributor below.

- *Paper I: Uncertainty estimation in wave energy systems with application to robust energy maximising control*

  This article was written by me, with significant contributions by *Valerio Grazioso* and *Demián García-Violini* under supervision of *John V. Ringwood*. *Valerio Grazioso* contributed to the CFD-based NWT mesh refinement and simulations, while *Demián García-Violini* contributed to the robust control design.

- *Paper II: Representative linearised models for a wave energy converter using various levels of force excitation*

  This work was carried out and reported by me, with oral and written inputs from *Demián García-Violini* and *John V. Ringwood*.

- *Paper III: Non-parametric multi-linear frequency-domain modelling of a wave energy device from experimental data*

  The data used in this work was provided by *Demián García-Violini* during an experimental campaign at Aalborg University, Denmark. The work was conducted and reported by me, with oral and written input from *Demián García-Violini* and *John V. Ringwood*.

Date: 30/11/2024

Signature: 

Acknowledgements

Personal

First, I would like to express my deepest gratitude to Prof. John Ringwood, my supervisor at COER, for the opportunity to pursue my PhD and for his invaluable guidance on my research, writing, and presentation skills. I am also sincerely thankful to my co-supervisor, Dr. Demián García-Violini, for his insightful guidance and technical expertise, particularly in theoretical concepts and coding. This thesis would not have been possible without their consistent advice and unwavering support. Special thanks to Dr. Valerio Grazioso for his guidance and fruitful collaboration during my PhD. My appreciation also extends to the Electronic Engineering Department staff, especially Carrie Anne Barry, Ann Dempsey, Denis Buckley, and John Maloco, for their administrative and technical support.

To the current and former members of COER: Yerai Peña-Sanchez, Christian Windt, Bingyong Guo, Andrei Ermakov, Hafiz Ahsan Said, Iain McLeod, Pedro Foraro, Augusto Sarda, Marco Rosati, Josefredo Gadelha da Silva, Agustina Skiarski, Sandra Carina Noble, Ilias Stasinopoulos, Nahia Iturricastillo, Eugenio Martin, Manal Mekelleche, Thalita Nazaré, Facundo Mosquera, and others, thank you for the invaluable discussions and making lab life enjoyable.

To the current and former members of COER: Yerai Peña-Sanchez, Christian Windt, Bingyong Guo, Andrei Ermakov, Hafiz Ahsan Said, Iain McLeod, Pedro Foraro, Augusto Sarda, Marco Rosati, Josefredo Gadelha da Silva, Agustina Skiarski, Sandra Carina Noble, Nahia Iturricastillo, Eugenio Martin, Manal Mekelleche, Thalita Nazaré, Facundo Mosquera, Pietro Desole, and others, thank you for the invaluable discussions and making lab life enjoyable.

I would like to express my deepest gratitude to my family—my parents, Kobra and Esfandiar, and my siblings, Mehrnoush and Ali—for their constant support, patience, and encouragement throughout this journey. I am also truly thankful to my friends, Hasti, Ali, Faezeh, Amir, Abtin, Fereshteh, and Pouya, whose friendship, despite the distance, has always warmed my heart. Additionally, I extend my sincere appreciation to my friends in Ireland, Solmaz, Saba, Dani, Milad(s), Yashar, Mohsen, Mehdi, Keivan, Faezeh, Sutoudeh, Mohammad, Minou, Negar, Tim, and Isaiah, for their companionship and support during my PhD.

Institutional

I sincerely thank Maynooth University for supporting my PhD through the *John and Pat Hume Doctoral (WISH) Award*. I am also grateful to the *Irish Centre for High-End Computing (ICHEC)* for providing HPC facilities and support.

List of Figures

List of Tables

List of abbreviations

AIC . . . . . Akaike Information Criterion

AR . . . . . Autoregressive

BPF . . . . . Band-Pass Filter

BEM . . . . . Boundary Element Methods

CF . . . . . Crest Factor

CFD . . . . . Computational Fluid Dynamic

CNWT . . . . . CFD-based Numerical Wave Tank

DTFT . . . . . Discrete-Time Fourier Transform

ECMWF . . . . European Center for Medium-Range Weather Forecasts

ETFE . . . . . Empirical Transfer Function Estimate

FFT . . . . . Fast Fourier Transform

FRA . . . . . Frequency response analysis

GHG . . . . . Greenhouse Gas

gPC . . . . . Generalised Polynomial Chaos

ITTC . . . . . International Towing Tank Conference

LFM . . . . . Linear Frequency Modulated

LiTe-Con . . . . Linear Time-Invariant Controller

LTI . . . . . Linear Time Invariant

MAPE . . . . . Mean Absolute Percentage Error

MPC . . . . . Model Predictive Control

NLFM . . . . . Nonlinear Frequency Modulated

NRMS . . . . . Normalised Root Mean Square

NWT . . . . . Numerical Wave Tank

RANS . . . . . Reynolds Averaged Navier-Stokes

RMS . . . . . Root Mean Square

PCHIP . . . . . Piecewise Cubic Hermite Interpolating Polynomial

PI . . . . . Proportional-Integral

PPR . . . . . Peak-to-Peak Ratio

PS . . . . . Pseudospectral

PTO . . . . . Power Take-Off

PWT . . . . . Physical Wave Tank

SG . . . . . Savitzky-Golay

SNR . . . . . Signal-to-Noise Ratio

SPH . . . . . Smoothed Particle Hydrodynamics

SWL . . . . . Still Water Level

WEC . . . . . Wave Energy Converter

1 Introduction

Contents

The sharp energy demand of industrialised nations, compounded with human-induced climate change, is one of the greatest challenges facing modern society. There have been continuous investments in greenhouse gas (GHG) emissions reduction, such as a binding target of net zero GHG emissions by 2050 based on European Commissions [1], and to achieve that, secure and sustainable energy systems need to be developed in an efficient way [2]. The use of renewables, is among the most important actions needed to reduce energy-related emissions, which would also bring other benefits, such as economical growth, sustainable development of rural regions, and reduction of dependence on energy imports [3]. Moreover, the shift towards sustainable and efficient energy systems in the EU would increase the security of the energy supply [4]. Renewable energy from seas (offshore renewable energy), has the potential for the vast increase in the volume of renewable electricity generation, due to availability of different sources (like wind, wave and tidal) that are abundant. The EU commission published strategy on offshore renewable energy sets targets of installing the capacity of 60 GW of offshore wind complemented by 1 GW of ocean energy by 2030 [5]. Ocean wave energy, a concentrated form of energy, generated through the transformation of solar radiation (by causing atmospheric pressure differential to generate wind and wind, in turn, creates waves by flowing across the water surface), is a widely acknowledged offshore renewable energy source with a potential to contribute to a sustainable global energy mix. Several studies in the literature estimated the global wave energy potential to be around 16000-18500 TWh/year [6, 7, 8]. The map showing global distribution of mean wave power for the 30-year time interval (1989-2018) is shown in Fig. 1.1 [9], which is calculated using the latest re-analysis data from European Center for Medium-Range Weather Forecasts (ECMWF) [10]. It can be seen, from Fig. 1.1, that between the latitudes of 40° and 60° of both northern and southern hemispheres have the higher mean wave power.

1.1 Wave energy technology and control

Despite being a vast resource and advantageous in the sense of having high energy density, research in wave energy conversion moves at a slow pace, due to the need to build robust devices, high installation costs, challenges related to integration into existing electrical grid, operation, and maintenance, and the technology has not yet reached the commercialisation stage. Developing wave energy converter (WEC) devices, used to harvest energy from ocean waves, is a highly cross-disciplinary

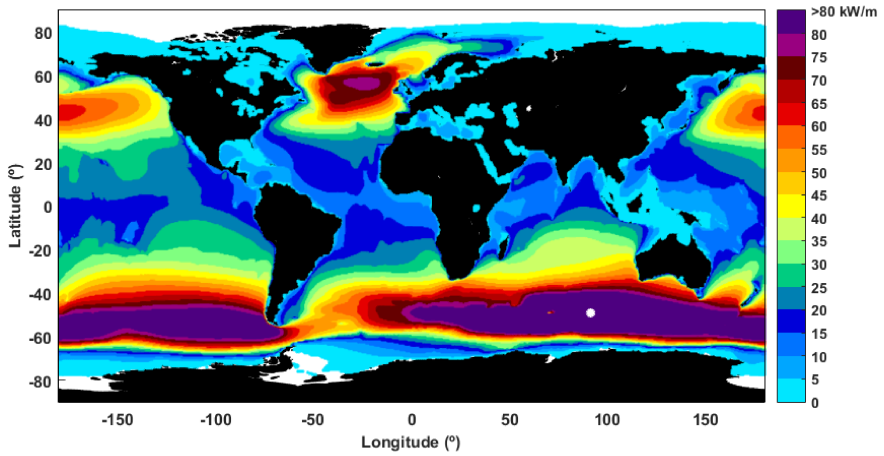

Figure 1.1: Mean wave power over the 30-year time interval considered (1989–2018) based on date from ECMWF [9].

task, met by a wide range of (aforementioned) challenges. Moreover, due to existence of a thousand different designs and patterns for WEC devices, clear technology convergence is absent in WEC technology development, and there is attempt to identify the best designs; analogous to three-bladed design of wind turbines. The various WEC types can be classified using different categories based on installed location, power take-off (PTO) system type, or based on shape and orientation with regard to the wave field [11, 12]. Among the various WEC devices, the point absorber WEC is one of the simplest and most promising concepts. It has been extensively investigated both theoretically and experimentally, with several review papers discussing its development in the literature [13, 14, 15]. This concept is also considered in the current study.

All WECs, regardless of their type, pursue a singular, fundamental goal: to achieve energy conversion with utmost economic efficiency. This entails finding good solutions for installation, structural robustness, and effective operation of the WEC across wide range of sea conditions, while minimising the overall cost of delivered energy. Optimisation of the WEC shape, maximising energy extraction from waves, and optimising energy conversion in the PTO system through dynamic analysis and control system technology can crucially impact many aspects of WEC operation. Maximising captured power of WECs through the PTO system generally involves a control problem where the load force (or torque) on the PTO system is manipulated, with consideration of physical device constraints [16].

Model-based control systems contribute to the majority of WEC control strategies, with a wide variety reported in the literature, since the early studies on reactive and latching control by Budal and Falnes [17]. Important control strategies that have been developed include impedance-matching-based control [18], model predictive

control (MPC) [19], optimal reference tracking control [20], linear time invariant (LTI) control [21], moment-matching-based control [22], and spectral/pseudospectral-based control [23]. Since WECs are typically subjected to nonlinear dynamics, considerable energy maximising control approaches have been also developed based on nonlinear WEC models, such as nonlinear MPC [24, 25] and MPC-based nonlinear optimal control [26], and nonlinear WEC control methodology based on pseudospectral methods.

For model-based control problems, using a linear WEC model under the assumption of small displacement is challenged due to the requirement for exaggerated device oscillations to maximise power absorption [27], thus affecting the control performance. On the other hand, nonlinear WEC control methodologies have the drawback of high computational burden [28]. Moreover, even high fidelity WEC models include uncertainty [29]. A robust control of WECs, based on a linear model and an uncertainty bound, is an effective control methodology which enhances the complexity compared to nonlinear WEC controllers, while improving the controller performance by dealing with distinct sources of modelling uncertainty and nonlinearity [23].

1.2 Motivation

WEC models are essential for development, power production assessment, optimisation, and model-based control design. There are diverse modelling routes; obtaining WEC models using mathematical/physics principles, determining the models from data by conducting numerical simulations or performing physical tests at laboratory or full-scale setups. The various approaches yield models characterised by a range of accuracy levels, affecting the performance of the (model-based) control strategies [30, 31]. Under control actions, due to required exaggerated motion of the WECs, linear WEC models (using first principles) fail to represent proper WEC behaviour, since their validity is limited to small motions around an equilibrium point. It has been shown that using data from high-fidelity wave tank experiments (either physical or numerical) are effective routes to derive (representative) linear or nonlinear WEC models. By appropriately selecting the system exciting signals and taking into account the specific limitations of the wave tank setups, the WEC model can be characterised to meet the dynamic requirements of the control system [29, 32]. Numerical wave tanks (NWTs) and lab-scale physical wave tanks (PWTs) are of the most important test setups for obtaining data-driven models, which can be used for dynamic behaviour assessment and control of WECs. In this study, frequency-domain non-parametric multi-linear WEC models are characterised using NWT for

robust control design, as detailed in 2, with a comprehensive assessment of the dominant dynamics of the linearised models presented in 3. In Chapter 4, PWT testing is employed to derive multi-linear WEC models. The range of tests that can be performed, and the parameters that contaminate the data-driven models, differ significantly between NWT and PWT experiments, impacting the accuracy of WEC models. Some of the key contributions of this study is the analysis of suitable input signals, the quantification of uncertainty in WEC hydrodynamic modelling, and the implementation of appropriate data-processing techniques that can be applied with an aim to get the most realistic WEC models. More specifically, a comprehensive representation of input signal synthesis and characterisation is provided in Chapter 2 to ensure sufficient fidelity in NWT tests, while satisfying the passivity condition of the system by applying post-processing techniques. In Chapter 4, more focus is given to characterise uncertainty and external disturbances inherent to the experimental setup under study, and the application of suitable data-processing techniques specific to the PWT setup and signal types, to attenuate the contamination effects on the data and preserve physical properties of the system. The multi-linear models derived from the NWT (Chapter 2) or PWT (Chapter 3) can serve as a foundation for model-based linear WEC robust controller design, where a single nominal model, surrounded by an uncertainty region, can be characterised using a range of representative linear models. An application to robust WEC control (using NWT experiments) is also presented in Chapter 2, including an analysis of the controller conservatism and absorbed energy based on different selections of the nominal model and uncertainty bound sizes. Non-parametric multi-linear models, obtained from either NWT or PWT tests, can be parameterised through system identification techniques, allowing for dynamic investigation and analysis of the system behavior. One of the main contributions of this study, presented in Chapter 3, includes the tracking of dominant dynamics of the WEC system at different operating points. This is achieved by analysing the dynamics of parametric WEC models obtained from force-input experiments in NWT setup, in addition to comparing the observed dynamics with the dynamics of a boundary element methods (BEM) based linear WEC model.

1.3 Overview of thesis

This section presents the detailed methodologies that form the foundation of this thesis. It covers the multi-linear modeling of WECs, uncertainty quantification based on both numerical and physical testing, and the robust control strategies applied to WECs under model uncertainty.

1.3.1 Multi-linear modelling of WECs

In this particular study, non-parametric multi-linear WEC models are referred to as representative linearised WEC models at various operating points, characterised in the frequency domain. Force-input experiments in a wave tank, by applying an exciting force through the PTO system (in the absence of incoming waves), can provide required data for WEC model characterisation. Properly selecting test signals, that cover the system dynamic frequency and amplitude, ensures model validity within the operational space, meeting the requirements of a control system. Due to the dynamical nonlinearities of WECs, the linearised WEC model parameters will vary with excitations at different input amplitude levels. Furthermore, the presence of uncertainty will affect the accuracy of these models. In this study, multi-linear WEC models are derived from NWT and PWT experiments, using the so-called *force-to-velocity* mapping, as detailed in Chapters 2 and 4, respectively. A key application of a multi-linear model is linear robust control of WECs. In this context, a multi-linear model is used to determine a single nominal linear WEC model and to quantify the uncertainty bound, which also includes model nonlinearities. Various approaches for determining the nominal model and different type of uncertainty sets can be explored to address the robust control problem. These choices influence the final absorbed energy of WECs under control actions. Section 2.6.2 details the various approaches for selecting the nominal model and specifying uncertainty. Section 2.8.3 discusses the resulting uncertainty regions, based on different choices of nominal models, and examines the impact of these choices on the final absorbed energy of the WEC under study.

One of the primary applications of multilinear WEC models is to effectively investigate the dominant dynamics of the WEC by considering the linearised models at various input amplitude levels and comparing them with the dynamics of a WEC system obtained using classical BEM methods. Multilinear WEC models, derived from force-input experiments, can provide sufficiently representative models of the overall system dynamics. As the force is applied through the PTO system, these linear models can be utilised for linear model-based WEC control design. A detailed analysis of the tracking of dominant dynamics in the multi-linear WEC model, obtained from force-input experiments in NWT setting, is presented in Chapter 3. Specifically, the resonance frequency trend and the bandwidth of the empirical transfer function estimates (ETFEs) at different input amplitude levels are first investigated using non-parametric frequency-domain linearised WEC models. Subsequently, parametric models are derived from these non-parametric frequency-domain models at different input amplitude levels using a system identification

tool. The dominant dynamics, particularly, dominant pole locations (real and imaginary parts) are analysed at various input amplitude levels and compared with the results using BEM method. The same dominant dynamic analysis from multi-linear WEC model can be done using the multilinear WEC model obtained from PWT experiments presented in Chapter 4.

1.3.2 Quantification of hydrodynamic model uncertainty in NWT testing

NWT testing is an important wave tank setup for characterising WEC models. Among the various methodologies to simulate a wave tank numerically, CFD-based NWTs are particularly effective at providing high-fidelity WEC models by capturing complex hydrodynamic interactions [27]. This capability makes them invaluable for model-based control approaches as well as research and development purposes.

Despite the advantages of numerical modeling, including CFD-based NWTs, a range of uncertainty sources has been documented in the literature that can impact accuracy and reliability [33]. One key source of uncertainty arises from the limitations of the governing equations used to predict the behavior of WECs. Assumptions and simplifications necessary for computational feasibility, such as the assumption of an incompressible fluid in the Navier-Stokes equations, can restrict the model's ability to accurately represent the complex phenomena surrounding WECs. Another significant source of uncertainty stems from numerical errors related to spatial and temporal discretisation. Proper mesh and time step resolutions, which are crucial for minimising these errors, can be determined through a convergence study [34].

It has been shown that even fully nonlinear WEC models obtained from CFD simulations contain numerical errors and uncertainties [29, 35], which can impact the performance of model-based controllers. One way to deal with distinct sources of nondeterminism in the WEC model with an aim of improving the controller efficiency is to consider an uncertainty bound around the WEC model, addressing a robust control methodology. Additionally, to manage the complexity of nonlinear WEC controllers, a linear WEC model can be employed, where the nonlinearities are also included in the uncertainty bound. Given the importance of accurately modeling both the nominal model and the uncertainty bound in CFD-based NWT (CNWT) experiments, Chapter 2 explores a range of linear models to determine a sensible representation of the nominal model and a minimised uncertainty region, while also satisfying the passivity condition necessary for robust control design. The limitations of the NWT under study has been taken into account for designing appropriate input signals to achieve a sensible representation of the nominal model and a minimized uncertainty region, while also satisfying the passivity condition necessary for robust control design.

1.3.3 Characterisation of uncertainty and external disturbance sources in PWT testing

PWT testing is a critical methodology for evaluating the performance, validating models, and as a basis for the (model-based) control of WECs. PWT tests offer essential insights into the WEC behaviour in full-scale testing, however, the accuracy of the WEC models obtained from PWT testing can be compromised by various sources of uncertainty and external disturbances. The range of tests that can be performed and contamination nature differ significantly in NWT and PWT tests, necessitating a comprehensive understanding of the uncertainty associated with PWT tests to enhance model fidelity. Additionally, the range of post-processing techniques that can be applied may vary based on the experiment type and the exciting signals used, requiring the proper adoption of data processing methods.

Moreover, within a specific PWT setup, contamination effects can vary under different operating conditions, as reported in the literature by analysing the discrepancy between simulated and experimental results. For instance, increasing discrepancies have been observed when moving from small to severe sea states due to heightened nonlinear effects in the experiments, as noted by [36, 37, 38]. On the other hand, some studies have reported significant experimental uncertainty at low levels of excitation. For example, [39] attributed this to low signal-to-noise ratio at these levels, and [40] identified dominant data contamination from non-hydrodynamic experimental load measurements at low-speed velocities of a WEC.

The studies highlight the importance of identifying uncertainty and external disturbance sources in PWT testing for accurate WEC model characterisation. It is also crucial to determine the techniques for eliminating artifacts from the captured data. Moreover, special attention should be given to understanding the level of contamination effects under various operating conditions.

Within this aim, the current study considers force-input experiments in a PWT setup (Chapter 4), and identifies the contamination sources, which are classified in three categories of electromechanical, hydrodynamic, and structural parts, and provides quantitative measure of their effect. Considering the wave tank setup and the exciting input signal type, proper data processing techniques are applied to exclude the artifacts from the data and obtain the most realistic WEC characterisation.

Similar to NWT testing, multilinear model can be obtained from force-input tests in PWT setup, with a particularly important potential application to determine a single nominal model and quantify the uncertainty bound from the family of models for robust control design of WECs. Using proper data-processing techniques will be helpful to get an adequate nominal model and correct uncertainty size.

1.3.4 Addressing and solving robust control of WECs under model uncertainty

A key contribution of this study is the development of a robust control strategy employed to WEC models derived from NWT testing, as detailed in Chapter 2, which is also applicable to the multilinear WEC models obtained from PWT testing provided in Chapter 4. The robust control addresses the solution to approach the optimal performance of nonlinear WECs including model uncertainty by using a linear control strategy, which is robust to linear model mismatches. The methodology, originally developed by [23], utilises linear nominal models and uncertainty bounds, having the advantage of less computational complexity compared to nonlinear WEC controllers while enhancing controller efficiency (considering the overall absorbed energy) by effectively dealing with various sources of nonlinearity and uncertainty.

Accurate characterisation of the nominal model and the determination of uncertainty bounds are crucial factors influencing robust control performance. Consequently, a comprehensive analysis of input signals and the application of appropriate data-processing techniques are conducted to obtain the most accurate ETFEs, providing the basis for nominal model selection. Additionally, various methods for determining the nominal model are employed to identify the minimised uncertainty region. The impact of different nominal models and their associated uncertainty sizes on the final absorbed energy using robust control is detailed in Chapter 2.

1.4 WEC modelling: techniques and fidelity considerations

WEC models can be developed through diverse methodologies, each presenting distinct assumptions, complexities, fidelity, and levels of uncertainty. The accuracy of the WEC model, and levels of uncertainty in the model has direct consequences for (model-based) control strategies [30, 31] which should be considered carefully.

Among different methods, linear WEC models, based on first principles, are valid only for small motions around the equilibrium point and generally fail to accurately capture the behaviour of WECs during the exaggerated motions needed for maximising energy extraction [27]. On the other hand, developing models based on data from physical or numerical experiments has been demonstrated as an effective approach for providing accurate representations of both linear and nonlinear WEC dynamics [41, 42, 43]. The following sections detail three main approaches for developing WEC models.

1.4.1 WEC model development approaches

Extensive effort has been carried out to implement models describing the hydrodynamic interaction between the fluid and the WEC [44]. To achieve an accurate wave-to-wire representation of a WEC, it is essential to also incorporate the dynamics of its power take-off (PTO) system, which can include linear PTOs (e.g., direct drive), nonlinear PTOs (e.g., impulse turbine), or coulomb PTOs (e.g., hydraulic cylinder), [45]. The physics-based modelling methods for WECs can be classified into two main categories: those based on CFD (used to solve the Navier–Stokes equations) and those based on potential flow theory (which solve the Laplace and Bernoulli equations) [46]. Models based on potential flow theory, such as BEM analysis [47], represent a simpler class of hydrodynamic WEC models, ranging from basic linearised representations to fully nonlinear approaches, but ignore fluid viscosity. Given the need for exaggerated WEC motion to enhance power absorption [27], incorporating models that capture relevant hydrodynamic nonlinearities results in more accurate WEC simulations.

The experiments to develop WEC models can be categorised in three main categories including numerical, full-scale, and laboratory-scale testing, each method offering specific challenges in terms of fidelity, computational demands, and practical applicability.

1. **Numerical tests:** Numerical methods are extensively utilised tools for modelling WECs, crucial for device design, optimisation, and control. The accuracy of these models depends heavily on the assumptions made. Numerical wave tank testing, based on CFD, for solving the fundamental Navier-Stokes equations whether using mesh-based methods like OpenFOAM [48] or meshless approaches like smoothed particle hydrodynamics (SPH) [49], can provide a fully nonlinear simulation. Compared to potential flow theory, CFD methods account for fluid viscosity implicitly and inherently, providing high-fidelity modeling results, particularly when nonlinear factors play a significant role in the dynamics of WECs [46]. Despite the high fidelity of CFD simulations, they come with significant computational costs. However, advancements in modern computing resources are gradually providing more computing power.

   CFD-based NWT simulations provide several important benefits [50]:

   - Effective control over reflections from the 'tank' walls.
   - The ability to perform full-scale device testing, thereby eliminating the challenges associated with scaling effects.

- Flexibility in applying a wide range of excitation signals, including incident waves, direct forces, and free response tests.
- Passive measurement of signals without physical sensors, preventing interference with the device or fluid dynamics and avoiding measurement errors.
- Elimination of the need for specialised equipment, such as a prototype WEC device.

In the current study, a three-dimensional, mesh-based NWT using CFD as the basis for its numerical simulations is utilised to characterise WEC models in Chapters 2 and 3. When conducting CFD-based simulations, careful attention must be paid to the design of the computational domain to accurately replicate the physical environment of the WEC. This includes specifying the wave tank and buoy geometry, boundary conditions, mesh resolution, and time steps.

2. **Laboratory-scale tests:** Laboratory-scale tests conducted in wave tanks offer a controlled environment for evaluating WEC models and understanding of the dynamic process, making them particularly valuable during the early development stages of WECs. Relevant similarities, such as geometric, kinematic, and dynamic similarities, must be partially or fully satisfied to ensure the meaningful and useful scaling and modelling of scaled prototypes [51]. In this thesis, these tests are referred to as PWT (physical wave tank) tests, and they are crucial for assessing performance, validating models, and control strategies. These tests are essential for verifying the accuracy of numerical models across different wave conditions and WEC designs [52, 53, 54, 55]. Additionally, model invalidation, enabling the independent analysis of dynamic uncertainty and external noise within experimental datasets, by comparing simulated responses with experimental data [56] have been topics of focus for some researchers. Chapter 4 of this study, analyses physical wave tank data obtained from an experimental campaign (at Aalborg University) involving a 1/20 scale Wavestar prototype device [57].

   PWTs come with their own challenges. Physical limitations, such as wave reflections and boundary effects, as well as components of the experimental setup (e.g., structure, mooring lines, and electromechanical parts), can introduce errors into the data. Another significant issue is the challenge of scaling results from laboratory tests to full-scale applications, which requires careful attention to scaling laws.

3. **Full-scale tests:**

   Full-scale testing is a crucial phase in the development and commercialisation of WEC technology, offering the most realistic validation of models by testing devices in real ocean environments. These tests deliver invaluable data on the actual performance of WECs under a wide range of sea conditions, including extreme events that are difficult to replicate in simulations or laboratory settings. A key advantage of full-scale testing is that it captures the realistic fluid dynamics around the device,which is often turbulent due to the large Reynolds number. In contrast, in PWT testing, using a very small model with a small Reynolds number (under Froude similarity) may result in laminar flow, which does not accurately represent real-world conditions [58].

   However, full-scale tests are expensive, logistically complex, and provide limited control over the experimental conditions. Deploying and maintaining WECs in the ocean requires significant resources, and the data collection process is complicated by the variability of sea states and environmental conditions.

Experimental methods, both numerical and physical, can be employed to derive empirical models and gather data for system identification. In this study, both high-fidelity CFD-based NWT tests and laboratory-scale PWT tests are utilised to develop empirical models. The WEC modeling methods are summarised in Fig. 1.2, with a focus on the approaches used in this study to derive empirical models from NWT and PWT, which are highlighted in the figure.

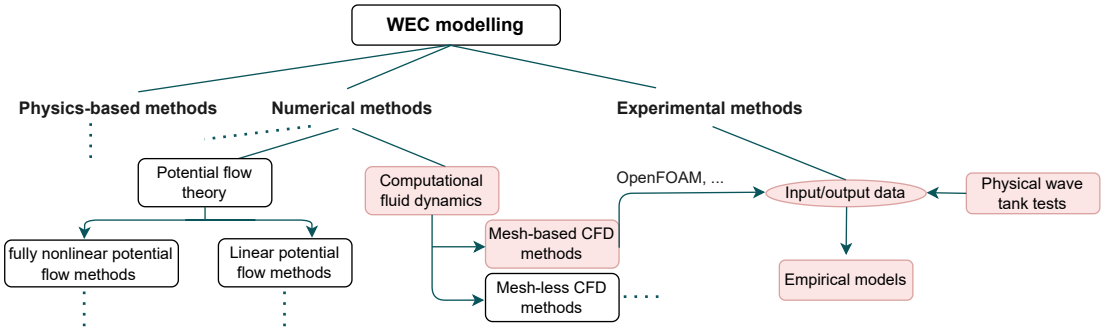

Figure 1.2: WEC modeling methods, with an emphasis on the approaches used in this study to derive empirical models from NWT and PWT testing (highlighted in red).

1.4.2 WEC system properties

In this study, where WEC models are charcterised from data with a particular application in robust control of WECs, it is crucial to ensure that the essential physical properties of the WEC device are met. Stability and passivity are particularly fundamental characteristics of physical WEC systems [59] that should be considered.

1.4.2.1 Stability

Stability, a well-established concept in dynamical systems, ensures that the system exhibits bounded-input bounded-output behavior. For WECs, stability refers to maintaining the structural integrity of the device when subjected to external forces with varying frequencies and amplitudes. Several methods have been developed to analyse and guarantee the stability of WEC systems. One such approach, involves imposing constraints on model parameters to ensure stability [50]. Another approach involves reconstructing the model to ensure stability by reflecting unstable poles from the right-hand side to the left-hand side of the complex plane when instability occurs in identified linear models [60].

The internal stability of WEC systems, particularly when modeled using the Cummins' equation, can be ensured by accurately defining parameters based on the physical properties of the WEC device [61]. This highlights the importance of accurate parameter selection in achieving and maintaining system stability.

1.4.2.2 Passivity

Passivity is a key characteristic of a physical WEC system, formalised around the principle that any increase in system energy comes solely from external sources, with the system itself unable to generate energy internally. In LTI systems, passivity is equivalent to the transfer function being positive across all frequencies [62, 59], or, equivalently, the system frequency response is confined to the right-hand side of the Nyquist plot.

Although passivity is intrinsic to physical WEC systems, it has been demonstrated that complete passivity cannot always be achieved. This limitation is observed in certain cases, such as models derived from high-fidelity CNWT or PWT experiments, as discussed in Chapters 2 and 4, respectively. One practical approach to ensure passivity involves applying ETFE phase correction. This correction is based on the asymptotic behavior of ETFE to align the system with passive behaviour. This post-processing technique for passivisation is employed in the studies detailed in Chapters 2, 3, and 4, to render a nonpassive system passive.

Moreover, in the study in Chapter 2, where a nominal model and uncertainty bounds are developed for robust control implementation, a critical passivity issue is identified from the analysis and estimation of uncertainty sets in WEC systems. To address this issue in the context of spectral-based control methodologies, a method for eliminating spectral components that violate passivity is implemented, as described in [29]. However, this elimination negatively impacts on the resulting performance because the power associated with the removed spectral components no longer contributes to the system's output. To address this issue, a recent practical passivisation methodology has been proposed, which considers the passivity of both nominal linear and uncertainty models for the application of a robust spectral-based control methodology, as outlined in [63].

By ensuring both stability and passivity, WEC systems can be effectively modeled and controlled to operate safely and efficiently in real-world conditions.

1.4.3 Wave tank setup for system identification

Wave tank setups play a crucial role in the system identification of WECs. These tests help in characterising the dynamic behavior of WECs by capturing their responses to various inputs. Two primary types of system identification tests are commonly conducted: free decay tests and force input tests.

1.4.3.1 Free-decay tests

The free-decay experiment is a methodology used to provide output data for the system identification process. In free decay tests, no external input is required; instead, a body is initially displaced from its equilibrium position against a restoring force, thereby imparting potential energy. Once released, the body moves back towards its equilibrium position. These tests can be conducted in both NWTs and PWTs and focus on identifying parameters related to inertia, restoring forces, and damping forces [50]. Depending on the level of damping, the body typically oscillates around its equilibrium position until all energy is dissipated, eventually coming to rest at equilibrium.

1.4.3.2 Force-input tests

The force-input test is a fundamental approach for identifying key dynamic parameters of a WEC, as it captures the broader dynamic behaviour of the system under various operational conditions. The models derived from force-input tests are capable of providing a sufficiently representative depiction of the total system dynamics.

Additionally, by applying external forces to the WEC, typically through the PTO system in the absence of waves, these tests become particularly valuable for model-based WEC control design. Various excitation signals can be used, as documented in [64], each with its own advantages and disadvantages, influencing the models that can be developed and their potential applications. The input forces are designed to cover a range of frequencies and amplitudes, allowing for a comprehensive evaluation of the WEC's response across its entire operational range.

For system identification to effectively capture the full dynamic behavior of the WEC, the input signal must be designed to excite the system across the frequency range where it exhibits significant response, while also covering the complete input amplitude (dynamic) range, while balancing efficiency and accuracy. Analysing the ETFE in terms of variability, resolution, and asymptotic behaviour based on physical characteristics of the system helps determine the optimal set of excitation signals for system identification.

In this study, force-input experiments are conducted both in NWT experiments (Chapters 2 and 3) and PWT experiments (Chapter 4) for system identification purposes. Specifically, a comprehensive approach to input signal synthesis and characterisation is presented in Chapter 2 to ensure sufficient fidelity in CFD-based NWT tests.

1.4.4 Wave tank setup for evaluation test

Evaluation tests in wave tanks are conducted to assess the performance of WECs by replicating realistic wave conditions as closely as possible. In wave tank testing for evaluation (either numerical or physical wave tank), the buoy is subjected to incoming waves generated by a wave maker in the tank. The goals of these tests include observing the WEC response to various wave states, evaluating energy capture, stability, and control performance. To prevent wave reflections during wave tank operations in wave flume mode, tanks are usually equipped with wave absorbers on the opposite side of the wave maker boundaries.

In Chapter 2 of this study, a robust control case study is presented using data from NWT experiments. This case study demonstrates the effectiveness of the WEC modeling (and the associated uncertainty set) and the control strategy. The wave tank setup for evaluation tests is used to extract time-domain excitation forces from numerical simulation data, which are then utilised in MATLAB to assess the performance of the robust controller.

1.4.5 System identification techniques

The objective of system identification is to derive the model of the system based on the measured input and output signals. This process can be broadly categorised into non-parametric and parametric approaches.

1.4.5.1 Non-parametric techniques

In non-parametric modeling, the system response is directly or indirectly derived from experimental data, either in the time domain (through impulse response) or in the frequency domain (through frequency response).

One common non-parametric model characterisation, following standard frequency domain techniques, is the so-called empirical transfer function estimate (ETFE). By considering an input/output (time-domain) pair, which are a measurable finite set of signals, the ETFE, representing the system frequency response, can be formulated as the ratio of the output signal Fourier transform to the input signal Fourier transform, under the assumption of periodic motion. An ETFE allows a straightforward way to analyse the frequency-dependent behavior of the system.

In specific applications, the discrete-time Fourier transform (DTFT) can simplify the calculation of the ETFE by focusing on the required frequency for spectral analysis. For instance, with a purely sinusoidal input signal, the amplitude and phase of the input are already known, and the DTFT of the output at that single frequency point can be used to obtain the frequency-domain representation of the output signal.

Additionally, windowing functions, such as the Tukey window (tapered cosine window) [65], are applied for the Fourier transform calculation to mitigate the effects of spectral leakage, which occurs due to the finite duration of the data records. The choice of window function is crucial, as it influences the accuracy of the frequency-domain representation, particularly for signals with abrupt starts and stops.

1.4.5.2 Parametric techniques

In parametric modeling, the system dynamic behavior is captured using partial or ordinary differential equations. The parametric identification results in a model where the system dynamics are described by a set of parameters, which can be related to physical quantities in some cases [66].

A frequency-domain system identification method specifically designed for WEC modelling is the FOAMM toolbox [67], which generates parametric models in state-space form through a moment-matching approach. A key feature of the toolbox is its ability to precisely match specific frequency points between the parametric

model and the non-parametric ETFE, including the device's resonant frequency. Based on finite-order hydrodynamic approximations, the FOAMM toolbox offers a user-friendly platform for parametric system identification, whether for the radiation convolution term or the complete force-to-motion dynamics of WECs. In Chapter 3 of this study, for analysing the dominant dynamics of WEC, the FOAMM toolbox is utilised to derive a state-space model for the entire force-to-motion WEC dynamics at different input amplitude levels. It has been suggested that using a 6^{th} order parametric model, and matching the frequency points at low- and high asymptotes, and resonance frequency, the ETFEs can be well approximated [68].

1.5 Uncertainty sources affecting data-based WEC models

In the development and optimisation of WECs, accurate modelling is critical to ensuring efficient energy extraction and optimal control system performance. WECs operate under dynamic conditions involving multiple stages of energy conversion and complex fluid-structure interactions. Control actions can augment these dynamics, leading to nonlinear hydrodynamic behaviour. These complexities make WEC modeling a challenging task, particularly when designing model-based, energy-maximising control strategies.

The methodology used to develop the WEC model can introduce various sources of uncertainty, impacting its accuracy and reliability, with significant implications for the performance and robustness of model-based control strategies [30, 31]. Identifying these uncertainty sources and understanding their impact at different operating points is crucial to prevent model misestimation. Neglecting uncertainties can significantly impair control performance, underscoring the importance of effectively managing these uncertainties in model-based control strategy development.

Accurate characterisation of the uncertainty bounds around the nominal model is essential for the controller to effectively capture the full extent of the uncertainty without becoming overly conservative due to overestimation of uncertainty size [23, 69, 29]. By applying appropriate data-processing techniques, artifacts can be mitigated, and the physical properties of the system can be preserved, resulting in more precise characterisation of the WEC system.

Although uncertainty analysis is a well-established practice in maritime fields such as ship design [70], offshore structures [33], and coastal engineering [51], it has not been widely adopted or thoroughly explored in WEC model testing, with its integration into wave energy studies remaining inadequate [71]. The exaggerated

motion required for WEC power capture, along with their exposure to extreme wave-induced forces, renders conventional uncertainty analysis techniques both risky and insufficient. Furthermore, WEC systems present unique challenges, often involving novel geometries, complex mooring systems, and PTO mechanisms, all of which significantly influence their motion and further complicate uncertainty analysis. In the field of WECs, some studies have investigated parameters contributing to uncertainty, including environmental conditions and the inherent characteristics of test setups. These studies explore various aspects of both numerical and experimental setups, such as the physical properties of fluids, initial conditions, model definitions, environmental influences, scaling effects, instrumentation accuracy, and human factors [33].

Studies addressing the uncertainty of environmental conditions include [72], which provides quantitative uncertainty bounds for different wave and environmental conditions. This work emphasises the importance of minimising uncertainty in power output and mooring line tension predictions. Similarly, [73] investigate uncertainty quantification in numerical ocean wave simulations using a stochastic framework based on generalised polynomial chaos.

The primary parameters contributing to uncertainty in the two main approaches of WEC modeling development—NWT and PWT testing—are discussed below and shown in Fig. 1.3.

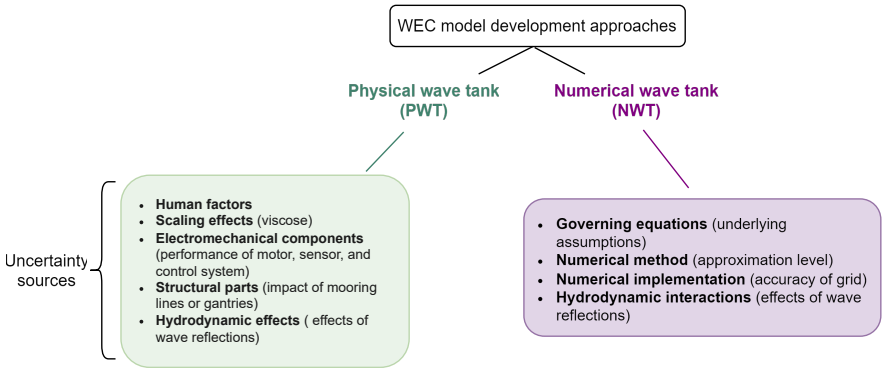

Figure 1.3: Potential sources of uncertainty in NWT and PWT testing.

In numerical wave tank simulation, uncertainties primarily arise from the limitations of the governing equations in accurately capturing the underlying physics, the approximations inherent in numerical methods, and the specifics of numerical implementation, such as the setup of the numerical wave tank model and grid generation [33]. Additionally, wave reflections from the tank walls can contribute to uncertainty in NWT testing.

In lab-scale wave tank tests, key sources of uncertainty include human factors, such as calibration and experimental setup, as well as scale effects like viscosity,

water depth truncation, and the non-similitude between Froude and Reynolds numbers [33, 51, 71, 74, 75]. Measurement uncertainties, including those from direct measurements and calibration, are also significant, along with electromechanical components, which can introduce issues like motor nonlinearity, hysteresis, noise, sensor positioning, and control system inaccuracies [33]. Additionally, tank setup biases, such as boundary effects and facility limitations, and model-related factors, including geometry, installation, mooring lines, and PTO systems, further contribute to uncertainties [71]. In particular, wave reflections from the tank walls present a major challenge in PWT testing. Furthermore, [76] identifies friction losses within the PTO system as a significant source of uncertainty in lab-scale wave tank testing, emphasising that these losses are neither easily scalable nor linear. To address the lacking WEC-specific knowledge of experimental uncertainty, the International Towing Tank Conference (ITTC) offers practical guidance on conducting formal uncertainty analysis in experimental WEC research [77, 78].

Generally, the contamination nature and the range of tests that can be performed differ significantly in NWT and PWT tests. In order to accurately perform model validation or invalidation, it is of paramount importance to have knowledge of the uncertainty associated with NWT and PWT tests. Considering different wave conditions and WEC types,WEC model validation, focussing on the accuracy of numerical models [52, 53, 54, 55], and model invalidation, enabling the independent analysis of dynamic uncertainty and external noise within experimental data sets, by comparing simulated responses with experimental data [56] have been topics of focus for some researchers.

It is generally believed that agreement between simulation and experiments is usually good in small to moderate sea states, as noted in studies such as [36, 37, 38], with discrepancy increasing in severe sea states, or in wave conditions that excite resonances (due to non-linear effects). Such discrepancies can result in overestimation of the dynamic response, and energy absorption [36]. Nevertheless, some studies have noted large experimental uncertainty at low levels of excitation as in [40], where the dominant level of (non-hydrodynamic) experimental load measurements contaminates data at low-speed foil velocity of a WEC. Similarly, [39] identifies deviations between simulation and experimental results in absorbed energy for a linear time-invariant controller (LiTe-Con) in small sea states, which are attributed to low signal-to-noise ratios.

Further exploration of uncertainty in experimental tests is provided in [79], which highlights the impact of measurement errors and filter characteristics on PTO friction damping force and mooring line force measurements, although precise quantification is not offered. In a recent study, [80] investigates experimental modeling uncertainty

quantification for a prototype wave energy converter by generating a family of WEC models using additive uncertainty. However, this study does not detail the sources of uncertainty, nor does it attempt to reduce variability in frequency-domain force-to-motion mapping or apply post-processing techniques to preserve the physical properties of the system.

Across all noted studies, there is a clear understanding that the fidelity of WEC models is critical for accurate performance evaluation, model validation, and control of WECs. However, to the best available knowledge, no studies in NWT testing have provided a comprehensive approach to input signal synthesis and characterisation that ensures sufficient fidelity in CNWT tests. This is essential for developing a reliable nominal model with minimised uncertainty while satisfying the passivity condition necessary for robust control design. Accordingly, a key contribution of this study (detailed in Chapter 2) is to address this gap by developing a representative nominal model and quantifying a minimised uncertainty region. This is achieved by selecting the optimal set of excitation signals for the NWT setup and applying appropriate data-processing techniques, all with the aim of supporting robust control design for WECs.

Additionally, within PWT testing, there is a lack of detailed evidence identifying the significant sources of uncertainty and their characteristics across different operating conditions. Additionally, techniques for eliminating artifacts from captured data to obtain accurate WEC model characteristics are not well-defined. In this context, the current study (detailed in Chapter 4) addresses these issues by focusing on a PWT setup involving a point absorber WEC, utilising chirp-type force input experiments. From these experiments, representative linearised WEC models are derived. The study characterises uncertainty and external noise at different operating points inherent to the experimental setup. Furthermore, tailored pre-processing (in the time domain) and post-processing (in the frequency domain) techniques are employed to preserve the physical characteristics of the WEC system and extract valuable information from the multi-linear models derived from PWT testing. Quantitative results are presented to highlight the dominance of contamination at various operating points, providing essential insights for realistic WEC modeling.

In this study, the term 'uncertainty' is used broadly. In NWT testing, it encompasses hydrodynamic WEC model nonlinearities and numerical uncertainty, while in PWT testing, it includes hydrodynamic WEC model nonlinearities, external disturbances and the effects of electromechanical and structural components.

1.6 Data pre- and post-processing techniques

To achieve realistic WEC characterisation from experimental data, the application of appropriate data-processing techniques is critical. These techniques must be tailored to the specific type of experiment (NWT or PWT), the wave tank setup, the nature of the signals used, and the inherent contamination present in the data. Proper data-processing can be applied that preserve the physical properties of the WEC system and reduce variability in frequency-domain models, leading to more accurate WEC models and better quantification of uncertainty regions.

In this study, data pre-processing and post-processing refer to data-processing techniques applied before and after the calculation of the ETFE, respectively. These processes are designed to ensure the authenticity of the ETFE results and to extract valuable information from the experimental data, ultimately contributing to a more precise and reliable characterisation of the WEC system.

1.6.1 Data pre-processing techniques (time-domain)

Data pre-processing refers to the application of techniques to time-domain data aimed at mitigating the effects of contamination before calculating the ETFE. The goal is to ensure that the signals used for system identification are as accurate and clean as possible. One effective approach for reducing distortion of a sampled signal is applying a discrete-time band-pass filter (BPF), which allows only frequencies within a specified range to pass through, based on the filter's frequency-domain characteristics. In cases where the contamination predominantly consists of high-frequency content, a low-pass filter can be employed to recover the underlying signal by attenuating the unwanted high-frequency components.

In this study, a BPF is applied to data from the NWT testing (as detailed in Chapter 2) to reduce distortion in output signals when sinusoidal and chirp-type excitation signals are used for system identification. In contrast, the pre-processing of PWT testing data (discussed in Chapter 4) involves a low-pass filtering approach combined with outlier removal, tailored to address the specific nature of contamination in that setup.

1.6.1.1 Application of a band- and low-pass filters to chirp signals

Filtering chirp-type signals presents a unique challenge due to their time-varying frequency characteristics, requiring careful consideration of filter design parameters to ensure effective data processing.

1. *Band-pass filtering*: For chirp-type signals, a BPF can be implemented in a frequency-varying manner, where the center frequency of the filter adapts to the instantaneous frequency of the chirp signal. This approach helps to reduce distortion while preserving the key signal content. However, as discussed in Chapter 2, this method presents challenges, particularly in the correct initialisation of the filter, which can introduce unwanted transient artifacts into the filtered data.

2. *Savitzky-Golay filtering*: The Savitzky-Golay (SG) filter [81], a low-pass filter, is widely used in signal processing applications for data smoothing. It operates by applying a local polynomial regression to a set of input samples in a least-squares sense. The cut-off frequency of the SG filter can be reasonably approximated based on the frame length and polynomial order [82]. When applying the SG filter to a linear chirp signal, a moving SG filter can be employed, with a fixed polynomial order but a varying window length (and corresponding cut-off frequency) to adapt to the changing frequency content of the signal. A detailed analysis of different design approaches for a moving SG filter, along with the optimal set of SG parameters for linear chirp-type signals, is presented in Chapter 4.

1.6.1.2 Outlier removal

Measurement force records from load cells often contain outliers that can degrade the quality of the data, obscuring meaningful information. It is crucial to assess the impact of outliers, the extent of contamination, and any issues related to missing data resulting from outlier occurrences. If necessary, outliers should be detected and appropriate data-cleaning techniques applied. Outliers can be identified visually or through statistical methods, such as using the standard deviation around the mean [83] or median absolute deviation [84]. Alternatively, they can be detected by examining their connection to the physical behavior of the test setup components, as discussed in this study (detailed in Chapter 4).

Once outliers are identified, removing them and reconstructing the missing portions of the signal are essential steps to preserve the integrity of the data. Static interpolation methods [85] are commonly used to fill data gaps, though they come with certain drawbacks, as detailed in Chapter 4. In this study, an autoregressive (AR) bi-directional model extrapolation [86] is employed to fill in the gaps in the recorded data, given the predominantly sinusoidal (chirp) nature of the excitation signals contaminated by external disturbance sources. This method helps maintain the accuracy and continuity of the data.

1.6.2 Data post-processing techniques (frequency domain)

In this study, data post-processing refers to signal-processing techniques applied in the frequency domain to the ETFE results. The goal is to enforce the physical properties of the WEC, reduce variability in the ETFE outcomes, and address issues that may arise from the mathematical implementation of ETFE calculations.

1. *ETFE phase correction*: To ensure passivity—a fundamental characteristic of the WEC system discussed in Section 1.4.2.2—a phase limit restriction on the ETFE can be enforced to maintain the correct asymptotic behavior. In this study, phase correction of the ETFE is a crucial step in data post-processing. For the data presented in Chapters 2 and 3, where ETFE is defined as a velocity-to-force mapping, the phase is constrained to the range of $[-90\ \ 90]^\circ$. However, in Chapter 4, where the ETFE is defined as a motion-to-force mapping, the phase is restricted to $[-180\ \ 0]^\circ$ across all frequencies.

2. *ETFE filtering*: To reduce variations in ETFE, while preserving the signal properties, and to facilitate the extraction of key information (such as the exact resonance frequency), ETFE filtering is employed as a post-processing technique. The moving average method, a commonly used statistical filter, calculates the average of a specified number of adjacent time-domain data points. Selecting an appropriate window size for this filter is crucial. This technique is applied to ETFE results obtained from both NWT and PWT tests in Chapters 2 and 4.

3. *ETFE phase unwrapping*: Phase unwrapping is another post-processing technique used when phase wrapping, defined as phase jumps (modulo 2π) between consecutive frequency bins, occurs in the ETFE phase. Such wrapping can result from specific software implementations of the fast Fourier transform (FFT) or from significant noise or distortion in the signal. This technique is applied to ETFE results from the PWT experiments in Chapter 4.

1.7 A thesis 'path'

This section provides an overview of how the papers included in this thesis connect to the various topics introduced in the introduction. Together, these papers form a cohesive narrative that examines the development of representative linear WEC models from NWT and PWT experiments, with careful consideration of the inherent differences between numerical and physical tests in both the range of tests and data

processing techniques. The analysis delves into the dominant dynamics of linear WEC models across different methodologies, effective strategies for determining nominal models, quantifying uncertainties, and designing robust control systems for NWT tests. These insights are also applicable to the multilinear WEC models developed from PWT experiments.

1. ***Paper I****: 'Uncertainty estimation in wave energy systems with application to robust energy maximising control'*:

   The study begins by detailing the numerical model development process described in Section 1.4.1, including the setup of various CFD-based numerical wave tanks for system identification and evaluation tests, as outlined in Sections 1.4.3 and 1.4.4, respectively. To ensure accurate and efficient simulations during NWT testing, mesh refinement is implemented.

   To achieve high-fidelity simulation results while accounting for the characteristics of the wave tank setup and the limitations of computing resources, a variety of input signals—such as sine, multisine, and chirp signals—are synthesised for force-input testing (Section 1.4.3.2), and data pre-processing techniques, tailored to each signal type, are then analysed as discussed in Section 1.6.1.1. The proper test signals are subsequently used to calculate the ETFEs, as detailed in Section 1.4.5.1.

   After applying post-processing techniques to the ETFEs (Section 1.6.2), the nominal model is determined, and the uncertainty is quantified. The study carefully considers the fundamental properties of WEC systems, ensuring that the nominal model and uncertainty bounds meet the passivity criteria outlined in Section 1.4.2. Finally, energy-maximising robust control strategies are developed based on the nominal model and its uncertainty bounds, as discussed in Section 4.7.

2. ***Paper II****: 'Representative linearised models for a wave energy converter using various levels of force excitation'*:

   This study implements system identification through force-input CFD-based NWT experiments (Section 1.4.3.2), utilising carefully designed sinusoidal excitation signals to cover the full range of frequencies and amplitudes likely to be encountered during system operation, providing a representative set of linear models for dynamic assessment and model-based control design of WECs. For ETFE calculation, the DTFT is employed to generate a frequency-domain representation of the signals, as sinusoidal inputs correspond to specific frequency points

(explained in Section 1.4.5.1). Additionally, a Tukey window function is applied to reduce spectral leakage and mitigate the impact of transients in the output signals (also detailed in Section 1.4.5.1).

The post-processing of ETFE includes phase correction to ensure the physical principles articulated in Section 1.6.2. Parametric models of the ETFEs derived from force-input experiments, along with a zero-input force model obtained from WAMIT, are developed using the FOAMM toolbox (outlined in Section 1.4.5.2). These models enable the tracking of dominant dynamics in the multilinear WEC model, as described in Section 1.3.1. Furthermore, the study compares the dynamic behavior obtained from this method with that derived from equivalent free-decay NWT experiments (Section 1.4.3.1).

3. ***Paper III****: 'Non-parametric multi-linear frequency-domain modelling of a wave energy device from experimental data'*:

   The study begins by detailing the WEC model development process through PWT testing, focusing on force-input experiments as described in Section 1.4.1 and Section 1.4.3.2. A significant contribution of this research is the identification and characterisation of contamination sources specific to the PWT setup, within the electromechanical, hydrodynamic, and structural components. The study provides quantitative measures of these contamination sources and analyses their dominance at various operating points.

   Another key aspect of this research is the development of advanced preprocessing techniques in the time domain, such as outlier removal from force signals (Section 1.6.1.2) and data gap reconstruction. Additionally, the study proposes an innovative application of the SG filter (Section 1.6.1.1) with a nonlinearly varying window length, designed to adjust the filter's cutoff frequency in alignment with the linearly varying frequency of the chirp-type signals used.

   Furthermore, post-processing techniques including ETFE phase correction, ETFE filtering, and ETFE phase unwrapping (Section 1.6.2) are applied, all aimed at achieving a realistic characterisation of the WEC.

To provide a clear overview of the research methodology and the interrelationships between the different papers included in this thesis, the flowchart in Fig. 1.4 is presented. This diagram visually represents the process flow, highlighting the key contributions of each paper and their integration within the overall research framework. The use of color coding within the chart distinguishes between the specific focus areas of each paper, as well as the shared methodologies and

processes that underpin the collective findings of the thesis. The following colour code is used:

Blue for Paper I, red for Paper II, with the purple sections indicating the methodologies and processes that are common to both papers, and green for Paper III.

1.8 List of publications

A list of peer-reviewed studies, that either make up the thesis core, or are the outcome of work done during my Ph.D., is provided in this section. The studies are arranged in chronological order. The abbreviated notation that follows indicates the status of a publication: (P) published, and (UR) under review. Additionally, the three paper, which make the main body of this thesis, are addressed by referencing a specific chapter that they are included.

Journal publications:

Status	Publication	Chapter
(P)	**Farajvand, M.**, Grazioso, V., Garcia-Violini, D. and Ringwood, J.V. *Uncertainty estimation in wave energy systems with application to robust energy maximising control*, Renewable Energy, Vol.203, pp 194-204, 2023.	2
(P)	**Farajvand, M.**, Garcia-Violini, D. and Ringwood, J.V. *Identification of representative linearised models for a wave energy converter using various levels of force excitation*, Ocean Engineering, Vol.270, Paper 113635, pp 1-9, 2023.	3
(UR)	**Farajvand, M.**, Garcia-Violini, D. and Ringwood, J.V. *Non-parametric multi-linear frequency-domain modelling of a wave energy device from experimental data*, Ocean Engineering,	4

Conference publications:

Status	Publication
(P)	**Farajvand, M.**, Garcia-Violini, D., Grazioso, V., Windt, C. and Ringwood, J.V., *Quantifying hydrodynamic model uncertainty for robust control of wave energy devices*, Proc. 14^{th} European Wave and Tidal Energy Conference, Plymouth, Sept. 2021, pp 2251-1:2251-10.
(P)	Garcia-Violini, D., **Farajvand, M.**, Windt, C., Grazioso, V. and Ringwood, J.V., *Passivity considerations in robust spectral-based controllers for wave energy converters*, Proc. RPIC2021 (XIX Reunion de Trabajo en Procesamiento de la Informacion y Control), San Juan, Argentina, 3-5 Nov. 2021.
(P)	**Farajvand, M.**, Garc-a-Violini, D. and Ringwood, J.V., *Characterising uncertainty and external disturbances in wave tank experiments for wave energy converter modelling*, Proc. 15^{th} European Wave and Tidal Energy Conference, Bilbao, Sept. 2023, Paper 376, pp 1-10.
(P)	Ringwood, J.V.,**Farajvand, M.**, Garc-a-Violini, D., *Takagi-Sugeno fuzzy modelling for wave energy converters*, accepted, Proceedings of the Trends in Renewable Energies Offshore (RENEW), 2024.

1.9 Thesis layout

This thesis is structured into five main chapters: an introduction, three papers (each presented in a separate chapter from Chapter 2 to Chapter 4), and a concluding chapter. The contents of each chapter are outlined as follows:

- Chapter 1 serves as the introduction to the thesis, beginning with a brief overview of wave energy technology and control, followed by the motivation for the research. This chapter also covers key topics such as WEC modeling techniques, sources of uncertainty impacting WEC models, and relevant data processing methods. Additionally, a "Thesis Path" section outlines how the papers included in the thesis are connected to the topics discussed in the introduction. The chapter concludes with a list of publications related to the thesis work.

- Chapter 2 includes the paper entitled 'Uncertainty estimation in wave energy systems with application to robust energy maximising control', which focuses on the accurate development of a nominal linear empirical transfer function

model, along with a precise estimation of the uncertainty bounds within that model, stemming from hydrodynamic uncertainties in NWT testing. A robust control case study is presented, demonstrating the effectiveness of the control strategy based on the nominal model estimation process and its associated uncertainty set.

- Chapter 3 includes the paper entitled 'Representative linearised models for a wave energy converter using various levels of force excitation' which focuses on investigating the dynamic behavior of a WEC system using fully nonlinear CFD-based NWT experiments, building on the findings from Paper I. Specifically, it utilises the optimal input signals and effective signal processing techniques identified in the previous study. The goal is to accurately track the dominant dynamics of the WEC across various force-input amplitude levels in the NWT setup and compare these results with those obtained using the classical linear BEM.

- Chapter 4 includes the paper entitled 'Non-parametric multi-linear frequency-domain modelling of a wave energy device from experimental data', which focuses on developing a realistic multilinear WEC model using force-input tests, addressing uncertainties and external disturbances in the PWT setup, which involves a 1/20 scale Wavestar prototype. To preserve the integrity of the physical system while managing data contamination, effective processing steps are applied in both the time and frequency domains. The research culminates in determining a single nominal model with an associated uncertainty bound, forming a foundation for robust WEC control.

- Chapter 5 synthesises the key findings of the thesis, providing a critical analysis of the results presented in each paper. This chapter also integrates the insights from the individual studies to draw overarching conclusions, highlighting the collective contributions of the research.

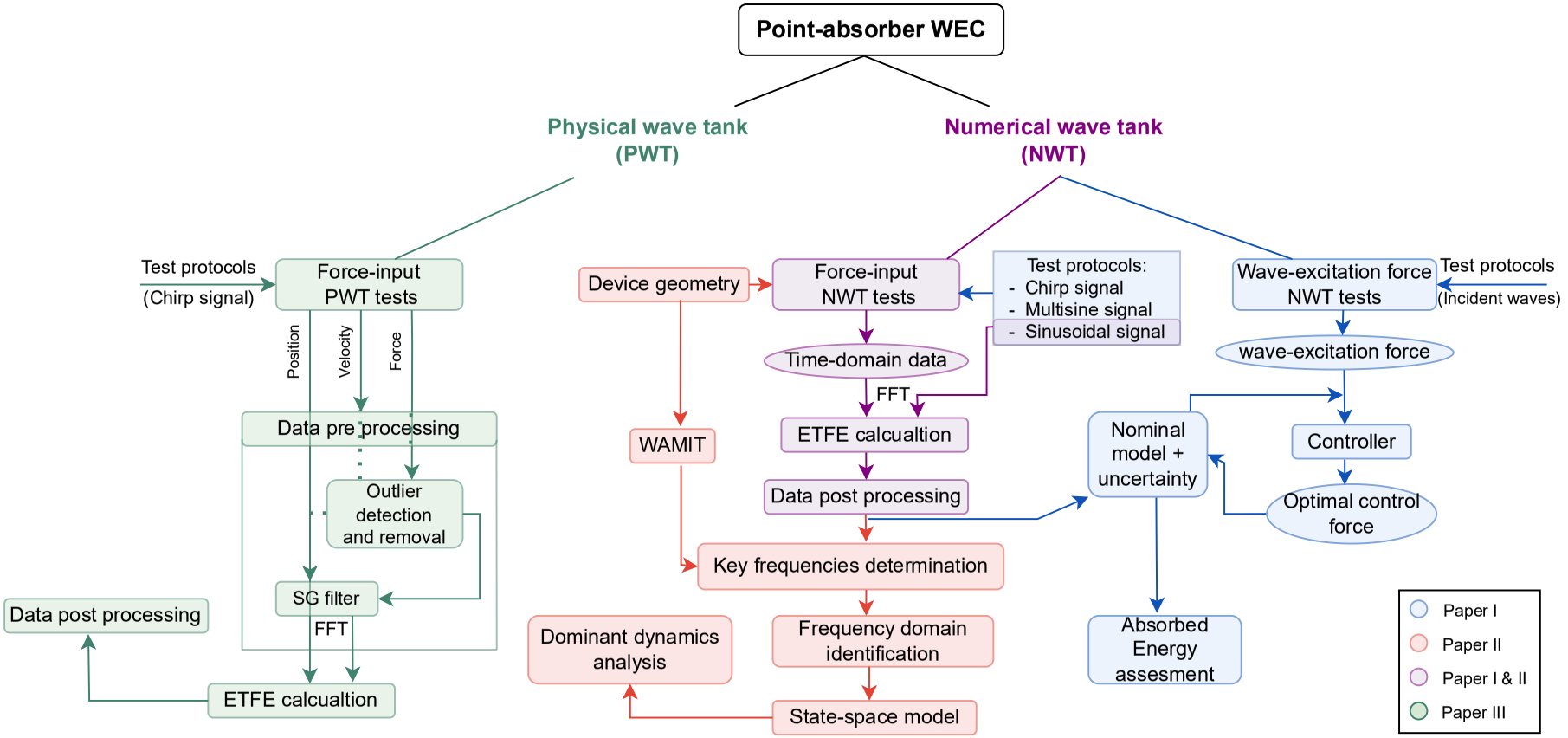

Figure 1.4: Flowchart depicting the research process, with each paper represented by a distinct color: blue for Paper I, red for Paper II, purple for elements common to both Papers I and II, and green for Paper III. This color scheme emphasises the connections and shared methodologies between the papers, as well as their individual contributions to the overall thesis.

2

Uncertainty estimation in wave energy systems with application to robust energy maximising control

Contents

2.1 Abstract

Under control action, wave energy devices typically display nonlinear hydrodynamic behaviour, making the design of energy maximising control somewhat onerous.

One solution to approach the optimal performance for nonlinear control problem under model mismatches is to employ a linear control strategy, which can be robust to linear model mismatches. However, accurate characterisation of the uncertainty in the linear model is vital, if the controller is to adequately capture the full extent of the uncertainty, while not being overly conservative due to overestimation of the uncertainty. This paper describes a procedure, employing CFD-based numerical tank experiments, to accurately produce a nominal linear empirical transfer function model, along with an accurate estimate of the uncertainty bounds in that linear model, due to hydrodynamic uncertainty. A robust control case study is provided, illustrating the nominal model estimation process, and its corresponding uncertainty set, including the complete procedure, required to generate the robust controller. Robust control results, on the fully nonlinear CFD model, are provided to demonstrate the efficacy of the modelling and control philosophy.

2.2 Introduction

Electrification, based on renewables, is a key solution to cater for increasing energy demand and tackle climate change. Among the renewable energy modalities, the exploitation of energy from the ocean waves, due to their high power density and relatively untapped potential, is key. However, economic competitiveness of wave energy converters (WECs) needs to be improved, in which energy-maximising control systems can play an important role.

Model-based control systems contribute to the majority of WEC control strategies, where the system model has a significant influence on the control efficiency. WECs are commonly modelled considering linearity assumptions, i.e. small displacements, based on Cummin's equation [87], with linearised hydrodynamic coefficients. However, linear models, under the linearising assumption of small movements, are challenged due to the requirement for exaggerated device oscillations to maximise power absorption [27]. Thus, the WEC models capturing possible nonlinearities, such as viscous drag, flow separation, vortex shedding [27], power take-off (PTO) nonlinearities [88], and complex hydrodynamic interactions, should be considered for the design and implementation of model-based control approaches. Nonlinear hydrodynamic modeling of WECs have been reviewed in [48, 89, 90]. Among nonlinear WEC models, computational fluid dynamics (CFD)–based numerical wave tanks (NWTs), capturing relevant hydrodynamic non-linearities, have proven to be of high-fidelity in research and development [27, 91].

A considerable number of energy maximising control approaches have been developed to deal with nonlinear WEC models. Nonlinear model predictive control

(NMPC) is a popular model-based control strategy, which obtains an optimal control input (in theory), while handling motion and force constraints systematically over a finite future time horizon [24, 25, 92]. Moment-based nonlinear optimal control, subjected to nonlinear dynamics of the WECs, is another particular energy-maximising strategy, using model order reduction theory by matching the frequency response of the device at specific spectral components (discrete frequencies) [22, 26]. Pseudospectral (PS)-based methods are another class of nonlinear WEC control methodology where the continuous-time energy maximisation problem is transcribed into a finite-dimensional optimisation problem. Application of the PS method for a nonlinear WEC control dealing with viscous drag and PTO nonlinearity is reviewed in [93].

Despite the development of different nonlinear control methodologies for WECs, the computational burden of the optimisation problems is a significative aspect [28, 24]. In addition, even fully nonlinear WEC models obtained from CFD simulations include numerical errors and uncertainty [35]. To enhance the computational complexity of nonlinear WEC controllers, while improving controller efficiency by dealing with distinct sources of nondeterminism in the WEC model, a robust control methodology, based on a linear nominal WEC model and uncertainty bound, has been developed in [23]. Precise nominal models and small uncertainty bounds are the key roles to reduce conservatism in the robust control design of WECs. Recent efforts have been aimed at accurately characterising the nominal and uncertainty models based on CFD simulations for the optimal robust control design of WECs [94]. However, a particularly important issue of the potential non-passive representation of the nominal and uncertainty model arises from CFD-based NWT modelling, which inherently discards intrinsic valuable information and degrades power absorption [94]. In order to best support robust control objectives, there is motivation for passivising a system by means of different approaches, most notably, feedback passivity, practical passivity, and frequency domain passivisation methodology [95]. A recent practical passivisation methodology, proposed by García et al. [63], can be considered for an efficient application of the robust spectral-based control methodology [23], when the system nominal description, or the corresponding uncertainty bounds, violate the intrinsic physical passivity of the system.

In the field of WECs, uncertainty quantification has been addressed in different studies. To briefly summarise, in [72] uncertainty in wave and environmental conditions is quantified and parameterised with the objective of minimising uncertainty towards the impact on power and mooring line tension prediction. Numerical uncertainty estimation for passive control of WECs, focusing on the spatial and temporal discretisation of CFD simulation, is studied by Wang et al. [35]. Online

estimation of dynamic uncertainty, for robust adaptive optimal control of WECs, is presented in [96]. Recently, a generalised polynomial chaos (gPC) methodology has been utilised for uncertainty estimation, where the studies in [97] and [73] address the gPC in WEC applications.

Consistent across all the noted studies is the implicit understanding that the fidelity of nominal and uncertainty models plays a crucial role in the effective robust control design for WECs. However, in wave energy robust control, none of the studies to date includes a comprehensive representation of input signal synthesis and characterisation, to give sufficient fidelity in CFD-based NWT tests, for a sensible representation of a nominal model and minimised uncertainty region, while satisfying the passivity condition with the goal of robust control design. Within this context, the latter is tackled in this study, representing a novel and original contribution to the state-of-the-art.

The layout of the remainder of this paper is as follows: First, the CFD-based numerical wave tank setup for system identification and wave excitation force tests, as well as CFD mesh refinement of the set-up, is presented in Section 2.3. Section 2.4 details input signal synthesis, including empirical transfer function estimate (ETFE) definition and details on the three types of input signals considered for system identification. Next, data post-processing, related to each input signal type and determination of the the best input signal choice for robust model-based control design of the WEC, is presented in Section 2.5. In Section 2.6, nominal model determination and uncertainty quantification from ETFE with consideration of ETFE refinement, and ETFE interpolation methodology is presented. A robust control design procedure, with a focus on the input signal required for the control design, is presented in Section 2.7. Section 2.8 demonstrates the application example, working through determination of the nominal model, uncertainty region, and robust control design for the case study. The results are presented in Section 2.8.3 and, finally, conclusions on the overall application are drawn in Section 2.9.

2.3 CFD model construction

CFD-based numerical wave tanks (CNWTs), offering complete nonlinear hydrodynamic models, are important tools for analysing WECs. The interaction of the waves and a submerged WEC can be simulated using well-established numerical tools, such as the open-source CFD toolbox OpenFOAM [98], where the fluid behaviour is analysed by numerically solving the Navier-Stokes equations. Under

the assumption of incompressible fluid, Reynolds averaged Navier-Stokes (RANS) equations, describing the conservation of mass and momentum, can be written as:

$$\frac{\partial \rho(t,x)}{\partial t} + \nabla.(\rho(t,x)U(t,x)) = 0, \tag{2.1}$$

$$\frac{\partial \rho(t,x)U(t,x)}{\partial t} + \nabla.\rho U(t,x)U(t,x) = -\nabla p(t,x) + \nabla.(\mu \nabla U(t,x)) + \rho f_b(t,x) + f_u(t,x), \tag{2.2}$$

where Equations (2.1) and (2.2) represent the conservation equations for mass and momentum, respectively, with t and x denoting the time and spatial variables, respectively, $U(t,x)$ the fluid velocity field, $p(t,x)$ the fluid pressure, ρ the fluid density, μ the dynamic viscosity, and $f_b(t,x)$ the field of external forces, such as gravity.

2.3.1 NWT configurations

CFD–based NWTs, depending on the modelling objectives, can be designed and equipped in different ways. In this study, two 3D NWT configurations are proposed, based on two different experiment types, i.e. system identification and evaluation tests. The WEC structure with a single degree of freedom, in the heave direction, is considered in our NWT.

2.3.1.1 NWT for system identification

The three-dimensional CFD–based NWT for system identification tests is designed in a tank with equal span in the x and y-directions, perpendicular to the tank depth (z-direction), with the buoy located in the centre of the tank corresponding to $(x,y,z) = (0,0,0)$. The tank is equipped with a wave absorber at the left and right boundaries ($x = \pm L_{T1}/2$). In the system identification tests, the WEC is driven into motion by applying a defined input force (excitation signal) $f_u(t)$ directly to the WEC, which are notionally applied through the PTO system ($f_u(t)$ is the actual force generated by the PTO). Due to symmetry in both x- and y-directions, the NWT configuration allows the CFD simulation to be carried out on a *quarter of the full NWT*, with a significant advantage in terms of computation time. The side view of the NWT schematic for system identification tests is shown in Fig. 3.2(a), where D and d are the tank and water depths, respectively, and L_{T1} is the tank length.

For the numerical experiments analysed in this study, the NWT setup is designed in a 6m deep tank with a water depth of 3m. The NWT for system identification spanning a length of $L_{T1} = 14$m in the x-direction and 14m in the y–direction, which is designed to be six wavelengths of the most significant radiated waves (occurring at peak frequency of the radiation damping of the WEC).

2.3.1.2 NWT for evaluation tests

The three-dimensional CFD–based NWT, for evaluation tests, is designed in a tank spanning the x (wave propagation direction) and y-directions, perpendicular to the tank depth (z-direction), and the buoy's location corresponding to $(x, y, z) = (0, 0, 0)$. The tank is equipped with a wave generation mechanism (at $x = -c$) and a wave absorber at the down-wave domain boundary (at $x = L_{T2} - c$) specified in [27], where incoming waves alone induce the WEC motion. The side view of the NWT schematic for evaluation tests is shown in Fig. 3.2 (b), where L_{T2} is the tank length, and c is the buoy distance from the wave generation boundary. The NWT configuration is symmetric in the y-direction, allowing *a half of the full NWT* for the CFD simulation, which is computationally efficient.

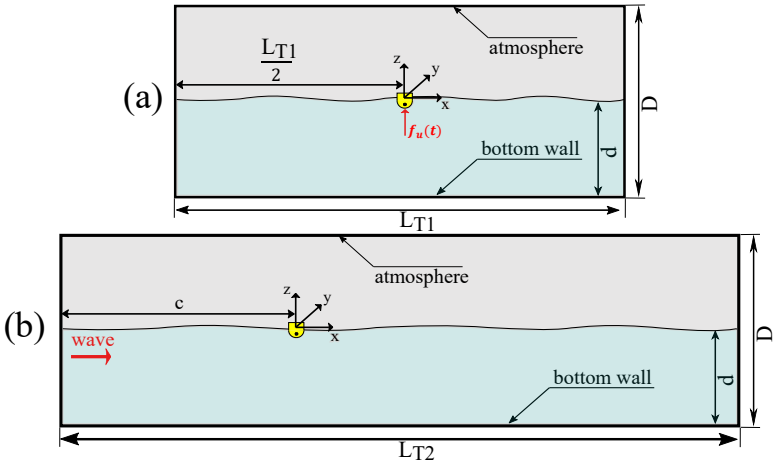

Figure 2.1: Schematic of the numerical wave tank for (a) system identification tests and (b) evaluation tests: Side view

The NWT, for evaluation tests, spans a length of $L_{T2} = 21.1$m in x-direction and 15.6m in the y-directions, and the buoy location is $c = 7.2$m down–wave (at least one wavelength distance) from the wave generation boundary, and $L_{T2} - c = 13.9$m from wave absorption boundary (at least two wavelengths distance).

2.3.2 CFD mesh refinement

The spatial discretisation of the NWT is implemented via a mesh; based on the CNWT setup presented in [27], ensuring the efficient and accurate simulations. With the aim of reducing the potential numerical uncertainty effects, additional mesh refinement of the NWT geometry, for system identification tests, is performed to ensure high fidelity. The buoy displacement resulting from the smallest input force is considered to generate the smallest mesh size around the buoy. Meshes are denser

around the buoy boundary and gradually increase in size toward the NWT boundary. Mesh refinement is performed on the existing mesh generated in [27] and [94] by adding more cells and, therefore, decreasing the dimension of the cells around the buoy. Fig. 2.2 shows a snapshot of the computational mesh of the side view of the quarter NWT using ParaView, an open-source software utility for visualising the data from OpenFOAM. As a result of mesh refinement, the total number of cells

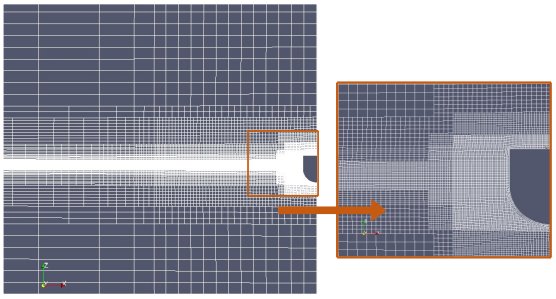

Figure 2.2: Paraview snapshots of computational mesh of geometry

increases from the initial number of 1.3 million to 4.06 million, and the cell dimension around the buoy has reduced from 0.013m to 0.0054m.

2.4 Input signal synthesis

Frequency response analysis (FRA) of systems, defined as the ratio of the Fourier transform of the output response to the Fourier transform of the input excitation, is a well-researched area which is used to characterise the system. In this study, based on well-known optimal conditions for the maximisation of energy absorption [61], the so-called *force-to-velocity* mapping is computed from the set of input excitation forces (PTO force), and their corresponding outputs (velocity) to identify the system. The specification of the system input is one important issue in system identification. The input signal must excite the system over the frequency range where the system has a significant frequency response, while, at the same time, covers the full input amplitude (dynamical) range. Three input signal types and their FRA are considered for this study: Sinusoidal signals, chirp signals, and multisine signals. In order to effectively describe the type of calculation required for the analysis and the use of the input signal, we begin with a definition of the empirical transfer function estimate (ETFE).

2.4.1 EFTE definition

The linear control design model for the current study is identified via a frequency-domain black-box-identification methodology, aiming to characterise the *force-to-velocity* mapping, i.e. the mapping $f(t) \rightarrow v(t)$, where $(f(t), v(t))$ is the input-output pair, defined in the time-domain. By defining $F(j\omega)$ and $V(j\omega)$ as the Fourier transform of the $f(t)$ and $v(t)$, respectively, the ETFE, $H(j\omega)$, is computed as:

$$H(j\omega) = \frac{V(j\omega)}{F(j\omega)}. \tag{2.3}$$

2.4.2 Sinusoidal signals

A sinusoidal input, with a single frequency, can be represented by:

$$x(t) = A\sin(\omega t + \phi), \qquad \text{for } t \geq 0, \tag{2.4}$$

where A, ω, and ϕ are the amplitude, frequency and phase of the sinusoid, respectively. To obtain a complete frequency domain characterisation of the system, for each considered amplitude, 'sufficient'[1] frequency values, ω, should be selected for the system identification tests, as follows: Asymptotic frequency values (low and high frequency limits), as well as the resonance frequency of the device, are of paramount importance. Considering the high variability of the frequency response around the resonance frequency of the system, selection of frequency points around the resonance frequency is advantageous in terms of efficiently capturing the main dynamical behaviour of the system in spectral domain. Using a series of sinusoids as input signal generates a line-spectral characterisation of the system, with a large experimentation time (with sufficient individual sinusoids) to cover the required frequency range.

2.4.3 Chirp signals

A chirp signal is a signal with a time-varying frequency. Due to the possibility of defining a so-called *instantaneous frequency*, chirp signals are of particular interest. Assigning a specific frequency to every time point in the input signal allows for a one-to-one mapping between time and frequency domains for linear systems.

[1] According to the specified target spectral discretisation.

2.4.3.1 Linear frequency modulated chirp signal

In a linear frequency modulated (LFM) chirp signal, the instantaneous frequency $f(t)$ varies linearly with time:

$$f(t) = ct + f_0 \tag{2.5}$$

where f_0 is the initial frequency and c is the chirp rate. A chirp signal in which the frequency *increases* with time is termed 'up-chirp' ($c > 0$ for LFM up-chirp), and a chirp signal in which the frequency *decreases* with time is termed 'down-chirp' ($c < 0$ for LFM down-chirp).

The corresponding time-domain function for a sinusoidal linear chirp can be formulated as:

$$x(t) = A\sin\left(\phi_0 + 2\pi\left(\frac{c}{2}t^2 + f_0 t\right)\right), \quad \text{for } t \geq 0, \tag{2.6}$$

where, A and ϕ_0 are the amplitude and initial phase of the LFM chirp signal, respectively. In a standard LFM chirp signal, A is a constant value while, in an amplitude modulated LFM chirp signal, A is a function of time.

2.4.3.2 Nonlinear frequency modulation chirp

In a nonlinear frequency modulated (NLFM) chirp signal, the instantaneous frequency $f(t)$ varies nonlinearly with time. A NLFM chirp signal can be defined, for example, by assigning equal, or balanced, permanency time to each frequency where the instantaneous frequency $f(t)$ is calculated as:

$$f(t) = \frac{c}{t} + f_0 \tag{2.7}$$

2.4.4 Multisine signals

Multisine signals consist of a sum of several simultaneously generated sinusoids, denoted as:

$$x(t) = \sum_{k=1}^{N} A_k \sin\left(\omega_k t + \phi_k\right), \tag{2.8}$$

where A_k is the amplitude and ϕ_k the phase of the k-th sinusoid, with N the number of sinusoidal components. $\omega_k = \omega_0 + (k-1)\Delta\omega$ is defined for harmonic multisine signals, where ω_0 is the initial frequency and $\Delta\omega$ the constant frequency interval. ω_k, for non-harmonic multisines, is based on user selected frequency points. While A_k and ω_k are normally not chosen independently, in the case of present study we use an open choice on the combination of A_k and ω_k.

Combining sinusoids increases the signal amplitude, which is generally undesirable in NWT experiments, where specific amplitude excitation is desired. In order to produce a specific amplitude multisine, the crest factor (CF), i.e. the ratio of the peak value of a signal to it's root mean square level, should be minimised. A well-known frequency-domain CF minimisation methodology, for uniformly spaced frequency components, is Schroeder's method [99], which optimises the ϕ_k to minimise the CF.

2.5 Data postprocessing

Typically, the NWT output signals show a level of distortion, adversely affecting the system identification process. The primary source of distortion relate to issues associated with limitations of the NWT itself. Most notably, the limitation in NWT length causes wave reflection, and, due to the computational burden, there is also a limitation in the time duration of the excitation signal. A level of post-processing is therefore carried out to mitigate the resulting distortion. A sample CFD-based input/output time domain analysis, based on an input signal with a maximum force amplitude of 20N and signal duration of 25s is considered, to illustrate the post-processing methodology.

2.5.1 Sinusoidal signal

Sinusoidal CFD-based NWT experiments for the system identification are processed in the time domain data for specific frequency points in the frequency range. Output signal distortion, corresponding to low-frequency input sinusoidal signals, are particularly noticeable, resulting from short signal duration. A potential methodology to reduce such distortion involves the application of a band pass filter (BPF) which passes only frequencies within a specific (narrow) frequency range. The transfer function of a second-order BPF is formulated from the standard continuous-time form:

$$T_{BP}(s) = G_o . \frac{(\frac{\omega_o}{Q_p})s}{s^2 + (\frac{\omega_o}{Q})s + \omega_o^2} \tag{2.9}$$

where G_o is the filter gain, ω_o the centre frequency of the filter, and Q the quality factor, determining the sharpness of the resonance in the filter frequency response. The filter bandwidth, defined as the difference between the higher and lower 3dB cut-off frequencies, is inversely proportional to Q. A bandpass filter, with a centre frequency of exactly the same frequency as the sinusoidal signal, is employed. To work with the sampled signals, a discrete-time version of the filter is obtained using

a matched z-Transform equivalent, with zero initial conditions, and is applied to both input and output signals. Fig. 2.3 shows sample unfiltered and filtered (using the BPF) input/output time-domain signals from a CFD simulation. The input signal is a single sinusoid with an amplitude of 20N and frequency of 0.2rad/s (low frequency asymptote), and sampling period of 0.001s, over the time interval of $[0, 25]$s. A direct consequence of the short signal duration is the incomplete period of the signal in this specific case. Considering sinusoidal signals, the ETFE for three different cases, including unfiltered input/unfiltered output, unfiltered input/filtered output, and filtered input/filtered output is computed, with results shown in Fig. 2.4. The discrete (in both time and frequency) ETFE is obtained using the Fast Fourier transform (FFT), with zero-padding to bring the number of calculation points to the next 2^j (j an integer), as required by the FFT. Based on the phase plot in Fig. 2.4, applying the BPF to the output signal, or input and output signals for the system identification process, results in even more distortion as the phases diverge from the expected (due to the passive nature of the device) value of 90° at the low frequency asymptote. As a result, BPF was abandoned as a post-processing technique for input/output time domain data using sinusoidal input force experiments.

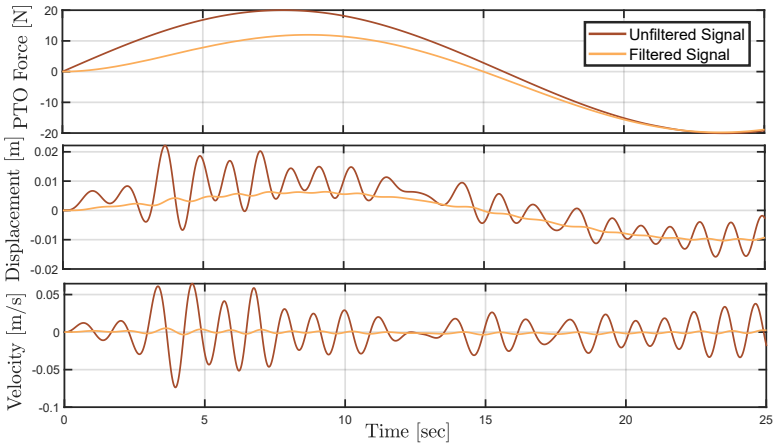

Figure 2.3: Time trace of unfiltered and filtered input/output signals for input sinusoidal signal

2.5.2 Chirp signal

Chirp CNWT experiments for system identification are simulated at different amplitude levels. Fig. 2.5 shows the input/output time-domain signals and their corresponding spectrograms. Based on the output spectrogram analysis in Fig. 2.5, distortion is evident, with the presence of parasitic low-frequency components. One possibility, to diminish this distortion, involves the application of a frequency-varying

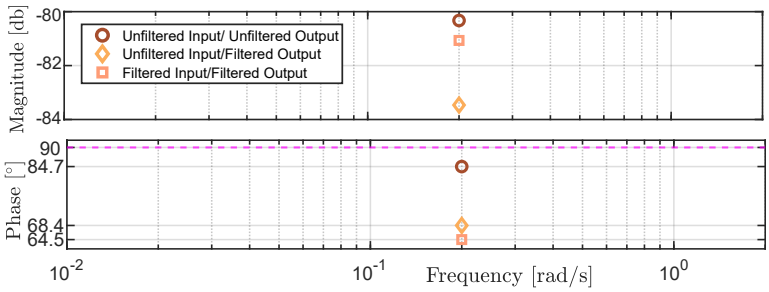

Figure 2.4: ETFE for sinusoidal input force

BPF, where the centre frequency of the filter varies with the instantaneous frequency of the chirp. The transfer function of the frequency-varying second-order BPF can be formulated as in (2.9), where ω is the time-varying frequency of the filter.

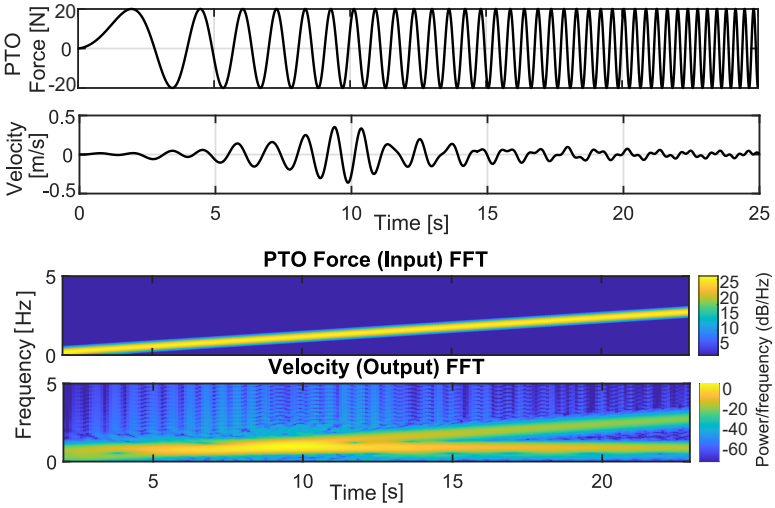

Figure 2.5: Time trace and spectrogram of the input/output signals for input LFM up-chirp signal (unfiltered)

Fig. 2.6 shows sample unfiltered and filtered input/output time-domain signal from the CFD simulation using a frequency-varying BPF. The input signal is a linear (frequency with time) up-chirp with maximum amplitude of 20N, where the frequency is linearly varying from 0.06rad/s to 18.89rad/s over a time interval of $[0, 25]$s, with a sampling period of 0.001s. The bandpass filter, with the centre frequency coincident with the signal frequency, is again discretised using a matched z-Transform equivalent and applied to both input and output signals. The ETFE for three different cases, including unfiltered input/unfiltered output, unfiltered input/filtered output, and filtered input/filtered output is computed, and results are shown in Fig. 2.7. Based on the phase plot in the ETFE, applying the BPF to the output signal, or input and output signals, for the system identification process, results in even more distortion as the phases diverge from the expected value

of 90° at the low-frequency asymptote. As a result, BPF was abandoned as a post-processing technique using chirp input force experiments.

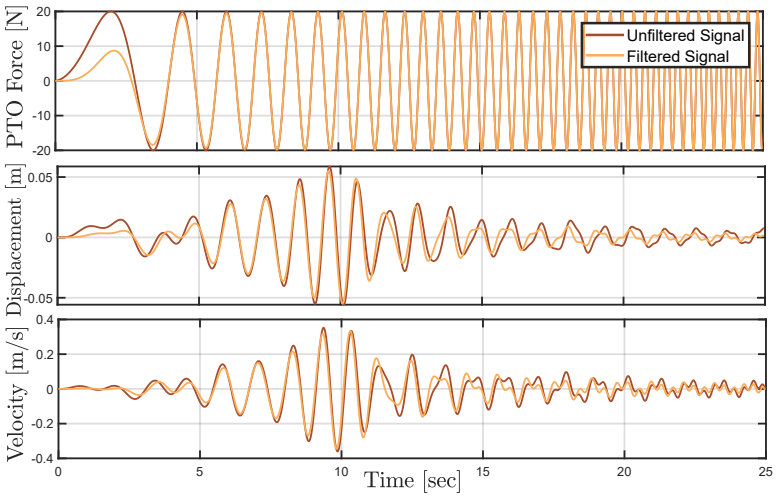

Figure 2.6: Time trace of unfiltered and filtered input/output signals based on LFM up-chirp input force.

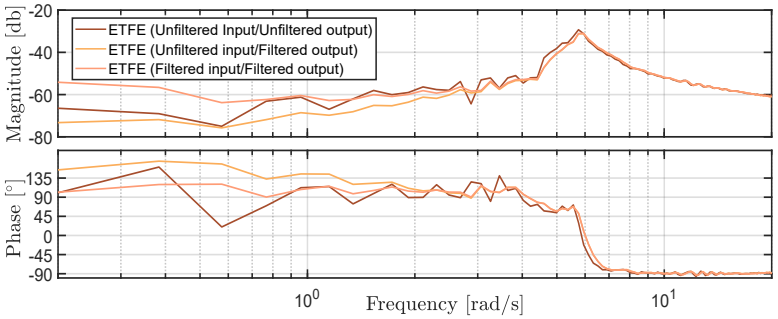

Figure 2.7: ETFEs computed from unfiltered input/unfiltered output, unfiltered input/filtered output, and filtered input/filtered output based on LFM up-chirp input force.

2.5.3 Final choice of input signal

In this section, the potential signal types and their corresponding ETFEs will be examined to choose the best set of input signals for system identification, leading to the most effective control of the WEC. Smaller ETFE variance values, resulting in a correspondingly small uncertainty bound, will lead to the less conservative control of WEC with corresponding improvement in control performance over the full operational space [23]. For comparison, five input signals, and their corresponding ETFEs, are presented in Fig. 2.8 and Fig. 2.9, respectively. The time-domain simulations are performed over the interval $[0,\ 25]$s. Fig. 2.8(a) shows a LFM up-chirp signal, specified in Section 2.4.3.1. Fig. 2.8(b) shows an amplitude-modulated

LFM up-chirp signal (Section 2.4.3.1), which is obtained by multiplying the LFM up-chirp signal in Fig. 2.8(a) by the half parabola starting from the value of 7.5 at $t = 0$s and finishing with the value of 1 at resonance time $t = 7.65$s. The NLFM down-chirp signal (Section 2.4.3.2), with maximum amplitude of 20N, and frequency function according to Equation (2.7), which varies from 18.89rad/s to 0.06rad/s, is shown in Fig. 2.8(c). A sample of a sinusoidal signal (Section 2.4.2) with an amplitude of 20N and frequency of 5.7rad/s is shown in Fig. 2.8(d), and finally, the non-harmonic multisine signal (Section 2.4.4), defined with flat amplitude spectra of 20N and the frequency set of $\Omega = \{0.2, 1, 2, 3, 4, 5, 5.5, 5.7, 6, 6.5, 7, 8, 9, 10, 18.89\}$rad/s and CF optimised using Schroeder's method [99] is presented in Fig. 2.8(e). The ETFEs, calculated from the various input/output time-domain signals, is presented in Fig. 2.9. The ETFEs obtained from LFM up-chirp, amplitude-modulated LFM up-chirp, and NLFM down-chirp input signals are shown in red, yellow, and orange lines, respectively. The individual circular and diamond markers represent the ETFE calculated from single sinusoidal signals and the multisine signal with frequencies contained in Ω, respectively.

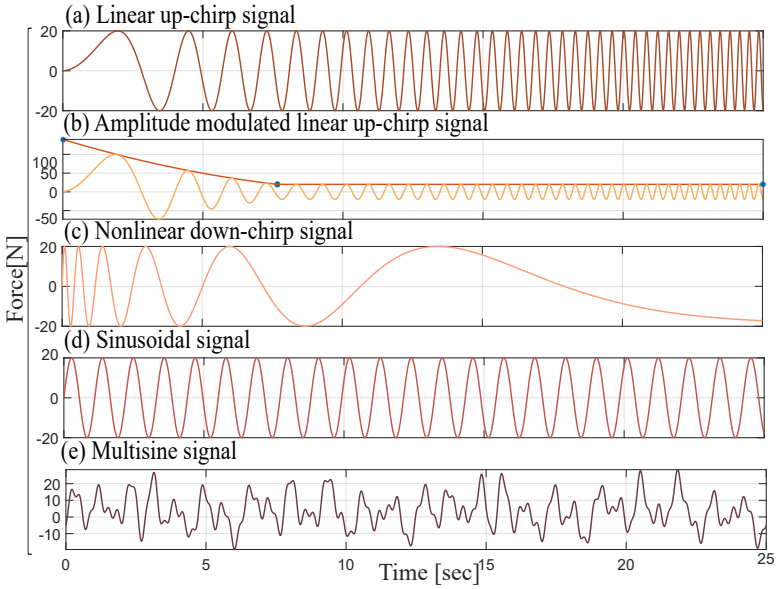

Figure 2.8: Time series of potential identification signals

Based on the ETFEs obtained for the five different input signal types (Fig. 2.9), the following conclusions can be drawn:

- The ETFE from the LFM up-chirp input signal has high variability, both in magnitude and phase. The main issue arises from the limitation of the simulation time length, which is designed to avoid wave reflections from the tank and also to reduce the computational complexity of the simulations. The

limited-time length results in a very short effective time duration spent at each frequency. LFM up-chirp input signals clearly result in considerable phase values above 90° violating the passivity requirement [94].

- The ETFE from the amplitude modulated LFM up-chirp input signal results in a smoother ETFE compared, with the standard linear up-chirp signal, at frequencies up to the resonance frequency of the device, and the overall signal-to-noise ratio is improved. However, passivity issues with this input signal are also evident, and the ETFE shows high variability at frequencies higher than the resonance frequency of the device.

- The ETFE from a NLFM down-chirp shows poor resolution and high variability at the resonance frequency and at high frequency, which will result in a large uncertainty bound. However, this experiment results in a relatively good low-frequency asymptote, which is around 90°.

- The ETFE from a non-harmonic multisine signal results in very large variations in the magnitude and phase. One possibility cause may be from distortion of the unequal amounts of time spent at each frequency by the CF optimisation algorithm.

- The ETFE from the sinusoidal input signals is smooth and has low variance, which is a direct result of spending more time at each frequency. This is the best compromise between the 25s time limit from reflections and the need to spend sufficient time at each frequency to resolve the ETFE.

In summary, the drawbacks associated with the LFM up-chirp, amplitude modulated LFM up-chirp, NLFM down-chirp signals reduce the value of their use in a system identification context. Ultimately, consistent amplitude sinusoidal signals at specific frequency set plus an additional frequency point at resonance were used to excite the system, repeated for different amplitude levels. However, some data from other experiment types, e.g. asymptotic values, are valuable in overall calibration of the data. As a result, these signal characteristics are considered to be a good compromise between time domain data resolution and computational requirements.

In the following, CFD simulations with sinusoidal input types will be exclusively adopted for ETFE calculation.

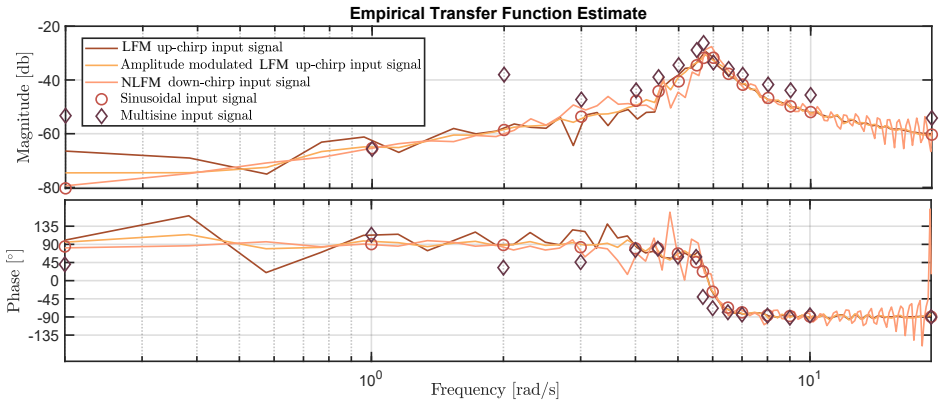

Figure 2.9: Empirical transfer function estimate obtained from five different input signals: LFM up-chirp input signal, amplitude modulated LFM up-chirp signal, NLFM down-chirp input signal, sinusoidal input signals, and multisine input signal. Note that the multisine and individual sinusoids are only defined at discrete frequency points.

2.6 Uncertainty quantification using the EFTE

ETFEs obtained from the CNWT experiments are now used to select both the nominal model and quantify the uncertainty for robust control design. ETFE refinement is performed prior to nominal and uncertainty model selection to ensure the correct asymptotic nature of the ETFE and passivity of the WEC model. Ultimately, the total uncertainty measured is a combination of nonlinearity in the (linear) nominal model, together with some minor phenomena resulting from imperfect simulation in the NWT.

2.6.1 EFTE refinement

ETFE refinement refers to mitigation of ETFE distortion arising from the CNWT experimental errors. ETFE refinement is carried out based on the satisfaction of two fundamental physical properties of the system:

2.6.1.1 Asymptotic nature of the ETFE

In order to ensure asymptotic behaviour consistent with a passive system, the ETFE phase components are forced to 90° and -90° at the low and high-frequency asymptotes, respectively.

2.6.1.2 Passive nature of the WEC

Considering the passive behaviour, which is formulated based on physical energy processes of the device, a passivisation methodology, based on Bode plot shaping,

is applied. In this study, ETFE refinement is performed by means of forcing the phase within $\pm 90^{\circ}$ degrees *for all frequencies*.

2.6.2 Uncertainty quantification

The methodology for determining the nominal model and specifying uncertainty, based on the ETFEs calculated from the NWT experimental data, is presented in this section.

2.6.2.1 Nominal model determination

The nominal model, based on the calculated ETFEs, can be determined using different approaches. Three possible choices are:

1. *Nominal model based on average ETFE:* In this methodology, the nominal model is calculated by taking the average of all ETFEs.

2. *Nominal model based on the most linear case:* This approach uses the ETFE corresponding to the smallest input force amplitude. The nominal model based on the smallest force will result in the closest model calculated by linear boundary element methods (BEMs) [50]. However, nominal model selection based on a linear approach may result in a large uncertainty region, with resulting conservative control [94].

3. *Nominal model based on minimum radius circles:* This method produces a synthetically built nominal model, which is formulated to minimise the uncertainty region. At each frequency point, the nominal model is located at the centre of a minimum radius circle which includes the extremities of the uncertainty region [23, 94].

2.6.2.2 Uncertainty specification

The uncertainty region, at a specific frequency point, is calculated based on the minimum distance between the nominal model and experimental models of different amplitude levels at that frequency. The multiplicative uncertainty, $\Delta_m(\omega)$, is defined :

$$\max_{1 \leqslant i \leqslant n} \{|\Delta_m^i(\omega)|\} = \max_{1 \leqslant i \leqslant n} \left\{ \left| \frac{H^i(\omega) - G_o(\omega)}{G_o(\omega)} \right| \right\} \tag{2.10}$$

where n is the number of experiment sets and G_o is the nominal model.

2.6.3 ETFE interpolation

Since the number of frequency points returned in the ETFE is limited by the number of individual sinusoids used for excitation (16 points), some level of interpolation is required to provide an adequate number of frequency points for robust control design. This is due to the pseudospectral nature of the control design, where a number of pseudospectral *basis functions* considerably in excess of 16 is required. Such an interpolation can be carried out using two methods: *(A)* Interpolation of the ETFEs based on the basis function frequency points and determination of the nominal model and uncertainty bounds at these points *OR (B)* Determination of the nominal model and uncertainty bounds from the raw ETFEs *and then interpolate* the nominal model and uncertainty bound at the basis function frequency points. Methodology *(A)* is adopted since, by first interpolating the sinusoidal based ETFEs, smoother interpolation is obtained.

2.7 Robust control design

The control objective for the WEC system is to maximise the total absorbed energy, J, defined as:

$$J \equiv E = -\int_0^T P dt = -\int_0^T v^T(t)u(t)dt, \tag{2.11}$$

which, in spectral and pseudospectral form, can be reformulated as:

$$J \approx J_N = \int_0^T \hat{\mathrm{u}}^T \Phi^T(t)\Phi(t)\hat{\mathrm{v}} = -\frac{T}{2}\hat{\mathrm{u}}^T\hat{\mathrm{v}}, \tag{2.12}$$

In (2.11) and (2.12), E represents the absorbed power over the time interval $[0 \quad T]$, P the instantaneous power, $u(t)$ the control force applied through the PTO system, and $v(t)$ the device velocity. $\hat{\mathrm{u}}$ and $\hat{\mathrm{v}}$ are approximations of $u(t)$ and $v(t)$ using an orthogonal set of basis functions Φ [23]. Substituting the approximation of the equation of motion of the WEC, $\hat{\mathrm{v}} = G(\hat{\mathrm{u}} + \hat{\mathrm{e}})$, into the approximate absorbed energy expression in (2.12), the following equality is obtained:

$$J_N = -\frac{T}{2}\hat{\mathrm{u}}^T G(\hat{\mathrm{u}} + \hat{\mathrm{e}}), \tag{2.13}$$

which is a quadratic function in the control variable $\hat{\mathrm{u}}$ alone. In (2.13), G is defined as the system model and $\hat{\mathrm{e}}$ is an approximation of the wave excitation force. If the concavity of Equation (2.13) can be guaranteed, there will exist a global maximum for the optimisation problem, with optimal solution:

$$\hat{u}_o^\star = -(G + G^T)^{-1}G\hat{\mathrm{e}}. \tag{2.14}$$

The optimal value of J_N, with (2.14) is substituted into (2.12), is then

$$J_N^\star = \frac{T}{2}\hat{\mathrm{u}}_o^{\star T} G(\hat{\mathrm{u}}_o^\star + \mathrm{e}). \tag{2.15}$$

For application of the robust control approach, the system model, G should represent a family of models which includes the nominal plus uncertainty model, defined as:

$$G = G_o + \Delta_a, \tag{2.16}$$

with G_o representing the nominal model of the system and $\Delta_a \in \mathbb{R}^{N\times N}$ the uncertainty model, formulated as:

$$G_o = \bigoplus_{k=1}^{N/2} \begin{bmatrix} \mathcal{R}_k^o & \mathcal{I}_k^o \\ -\mathcal{I}_k^o & \mathcal{R}_k^o \end{bmatrix} \tag{2.17}$$

and

$$\Delta_a = \bigoplus_{k=1}^{N/2} \begin{bmatrix} \delta_k^{\mathcal{R}} & \delta_k^{\mathcal{I}} \\ -\delta_k^{\mathcal{I}} & \delta_k^{\mathcal{R}} \end{bmatrix},$$

where

$$\mathcal{R}_k^o = \mathbb{R}e\{g_o(j\omega_k)\}, \mathcal{I}_k^o = \mathbb{I}m\{g_o(j\omega_k)\}$$

and

$$\delta_k^{\mathcal{R}} = \mathbb{R}e\{\delta_k\}, \delta_k^{\mathcal{I}} = \mathbb{I}m\{\delta_k\}.$$

$\mathcal{R}_k^o, \mathcal{I}_k^o \in \mathbb{R}$, and $g_o(j\omega_k)$ represent the nominal frequency response, while $\delta_k \in \mathbb{C}$ represents the uncertainty level at frequency ω_k. Considering the feasibility (passivity) condition for the real system, G must be positive real:

$$\mathcal{R}_k = \mathcal{R}_k^o + \delta_k^{\mathcal{R}} > 0, \tag{2.18}$$

where $\mathcal{R}_k$ is the real part of the system model.

Using the feasibility condition and defining the best worst-case performance (best-WCP) solution as the input that minimises the performance degradation when the system under study is affected by a bounded uncertainty set Δ, the robust control problem statement can be defined as:

$$\hat{\mathrm{u}}_r^\star \leftarrow \max_{\hat{\mathrm{u}}\in\mathbb{R}^N} \min_{\Delta\in\mathcal{U}} J_N. \tag{2.19}$$

Equation (2.19) represents a robust quadratic formulation where $\mathcal{U}$ indicates the set of all possible uncertainty.

2.8 Case study

2.8.1 System setup

The point absorber-type WEC considered for this study has an axisymmetric cylindrical geometry and hemispherical bottom. A schematic of the structure, including all relevant physical properties, are shown in Fig. 2.10. The radius of the hemispherical and cylindrical sections is 0.25m, with the height of the cylindrical section also 0.25m. The mass of the device is 43.67kg, with the centre of the mass located at a vertical distance of 0.191m from the bottom-most point of the buoy.

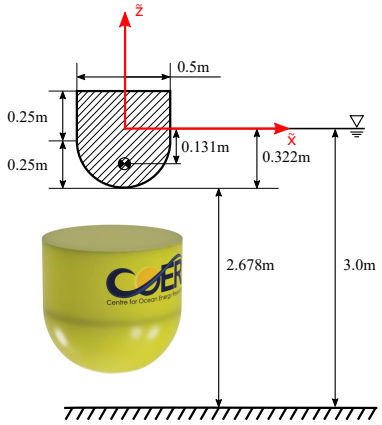

Figure 2.10: Schematic of the considered WEC structure

2.8.2 ETFE evaluation

The ETFEs resulting from the complete set of sinusoidal exciting signals are shown in Fig 2.11. ETFE determination is based on the NWT configuration presented in Section 2.3.1.1. The sinusoidal PTO force excitation signals consist of a total of 96 experiments combining the amplitude set $A_i = \{20, 40, 60, 80, 100, 120\}$N using a set of individual frequencies $w_j \in \{0.2, 1, 2, 3, 4, 5, 5.5, 5.7, 6, 6.5, 7, 8, 9, 10, 18.89\}$ rad/s plus a resonance frequency specific to each amplitude set. This selection of frequencies and amplitudes gives a smooth representation transition between the ETFE points corresponding to discrete values of amplitude/frequency. In particular, the amplitude range selection ranging from linear behaviour (smallest amplitude) to amplitudes forcing the device out of the water (largest amplitude) and intermediate values, covers a full dynamical characterisation of the nonlinear system. Each experiment is driven by a finite set of N exciting force signals that generate a corresponding set of velocity signals. The simulation time of the sinusoidal experiments is the interval $[0,\ 25]$s. The ETFEs for each of the A_i amplitudes, after

the employment of ETFE refinement as explained in Section 2.6.1, and interpolation across frequency points using piecewise cubic Hermite interpolating polynomials (PCHIPs), are shown in Fig. 2.11.

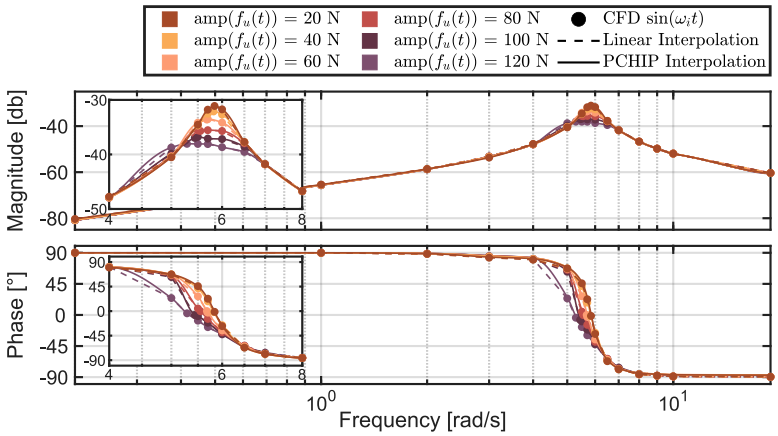

Figure 2.11: Empirical transfer function estimates (ETFEs) for the 6 amplitude levels, using sinusoidal signal excitation (based on unfiltered data).

In this study, three nominal model candidates are considered for robust control design. Fig. 2.12 shows the interpolated ETFEs, along with the three nominal model possibilities; $\hat{G}(\omega)$ is the nominal model based on the average ETFE, $G_{lin}(\omega)$ is the nominal model based on a linear BEM approach, and $G_{circ}(\omega)$ is based on the minimum radius uncertainty circles as detailed in Section 2.6.2.1 (1-3). The

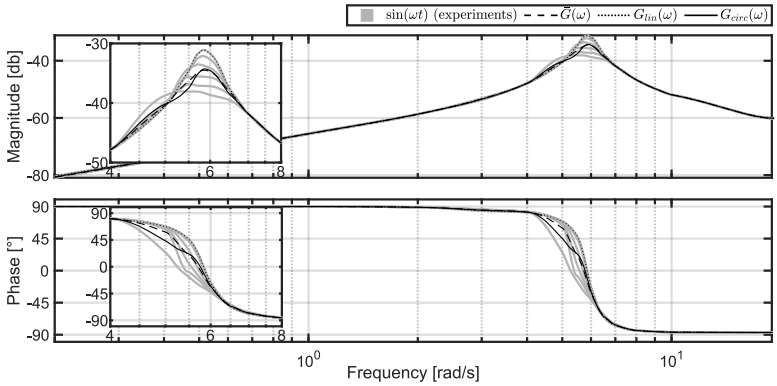

Figure 2.12: ETFE and Nominal models based on $\hat{G}(\omega)$, $G_{lin}(\omega)$, and $G_{circ}(\omega)$

same information, including the ETFEs and the three nominal model candidates, is shown in Fig. 2.13 on a polar (Nyquist) plot.

The uncertainty bound, based on the formulation presented in Section 2.6.2.2, is obtained for the three nominal model candidates, with results as shown in Fig. 2.14. Comparing the uncertainty magnitude corresponding to the three different nominal models, $\hat{G}(\omega)$, $G_{lin}(\omega)$, and $G_{circ}(\omega)$, it is clear that selection of the centre of

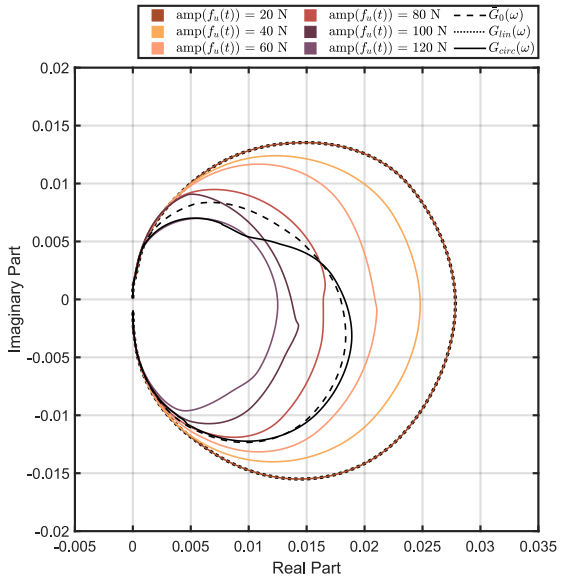

Figure 2.13: ETFEs and nominal models based on $\hat{G}(\omega)$, $G_{lin}(\omega)$, and $G_{circ}(\omega)$ in polar form.

the minimum radius circles as a nominal model ($G_{circ}(\omega)$) results in a significantly smaller multiplicative uncertainty bound, $|\Delta_m|$. The ETFEs, the three different nominal models, and their corresponding uncertainty regions are also represented in the Nyquist (polar) domain, shown in Fig. 2.15.

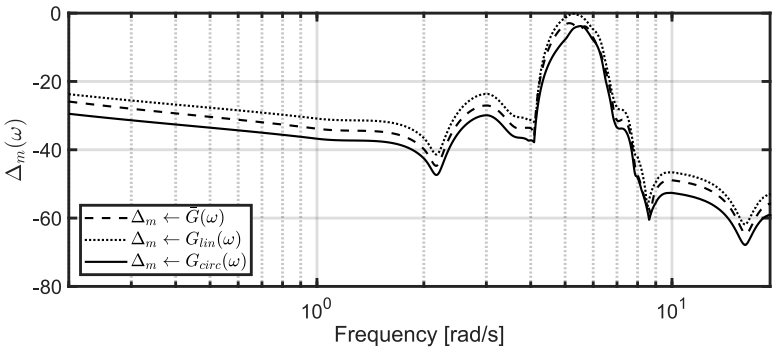

Figure 2.14: Uncertainty size $|\Delta_m|$ using multiplicative uncertainty structure for three different nominal models $\hat{G}(\omega)$, $G_{lin}(\omega)$, and $G_{circ}(\omega)$.

2.8.3 Sample robust control results

The control part of this study is based on the assumption of full knowledge of the wave excitation force. Wave excitation force tests are simulated in a CFD environment, as detailed in Section 2.3.1.2. The WEC structure is exposed to the irregular incident waves of a JONSWAP spectrum with a significant wave height of $Hs = 0.1$m, peak period of $T_p = 1.94$s, and steepness parameter $\gamma = 3.3$. This

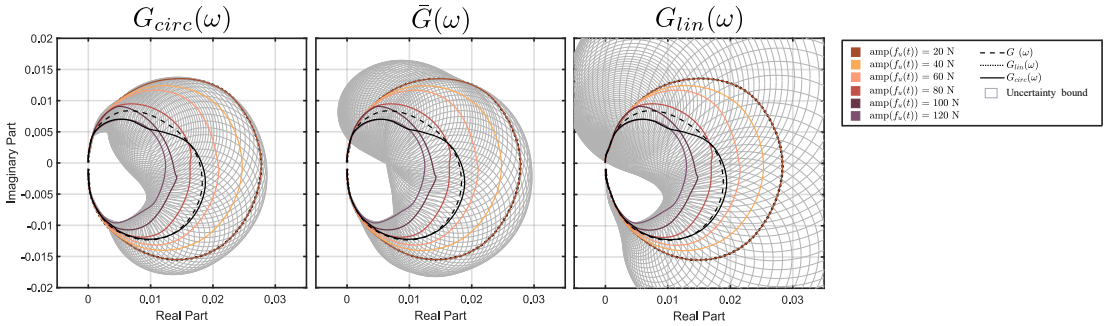

Figure 2.15: ETFEs, Nominal models based on $\hat{G}(\omega)$, $G_{lin}(\omega)$, and $G_{circ}(\omega)$, and their corresponding uncertainty, in polar form.

condition represents realistic, scaled conditions at the AMETS test site in Bellmullet, Co. Mayo, off the West Coast of Ireland [100], which has challenging wave conditions, consistent with the generation of nonlinear hydrodynamic fluid/device interaction. (To retain deep water conditions of the AMETS site, the Froude scaling with a scaling factor of 1/30th is applied [101].) The time-domain representation of the wave excitation force, extracted from the numerical simulation data, together with the approximated excitation force using 63 frequency components, is shown in Fig. 2.16. A good agreement between the approximated excitation $\tilde{f}_{ex}(t)$ and experimental excitation wave force $f_{ex}(t)$ can be observed.

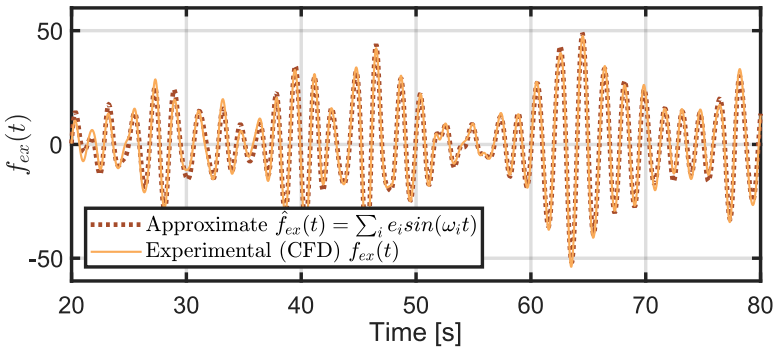

Figure 2.16: Experimental and approximated wave excitation force

The robust controller is designed based on the nominal models, G_{circ} (the nominal model corresponding to the smallest uncertainty size (Fig. 2.14)) and $G_{test}(\omega)$, where $G_{test}(\omega)$ is a generic test model contained in the family of systems, represented by the set of circular boundaries. In addition, two solutions for the optimal control forces are computed:

- $u_o(t)$ is computed using the nominal approach, i.e. using the nominal model, $G_{circ}(\omega)$.

- $u_r(t)$ is computed using the robust approach, based on experimental test models, $H^i(\omega)$.

The sin and cos frequency component coefficients of the optimal control inputs, $u_o(t)$ and $u_r(t)$ are shown in Fig. 2.17. Note that, in general, the components corresponding to $u_o(t)$ have a greater amplitude than $u_r(t)$. For assessment of the

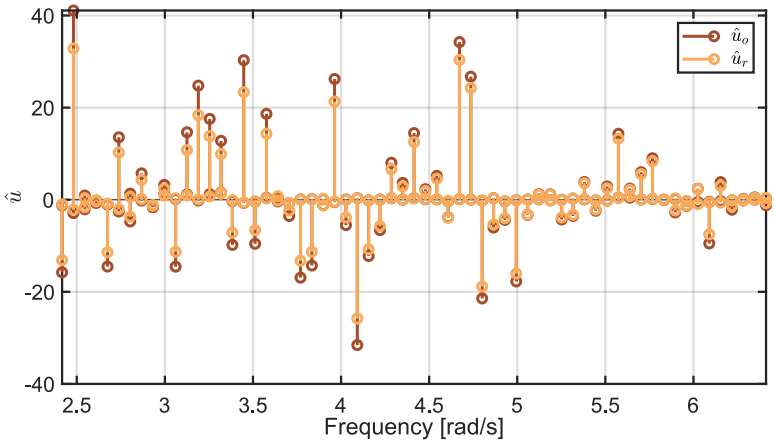

Figure 2.17: Frequency components of the optimal control inputs

control performance, the following steps are taken:

1. $u_o(t)$ is applied to $G_{circ}(\omega)$ and $G_{test}(\omega)$, and
2. $u_r(t)$ is applied to $G_{circ}(\omega)$ and $G_{test}(\omega)$.

Fig. 2.18 shows the time trace of absorbed energy when $u_o(t)$ and $u_r(t)$ are applied to $G_{circ}(\omega)$ and $G_{test}(\omega)$.

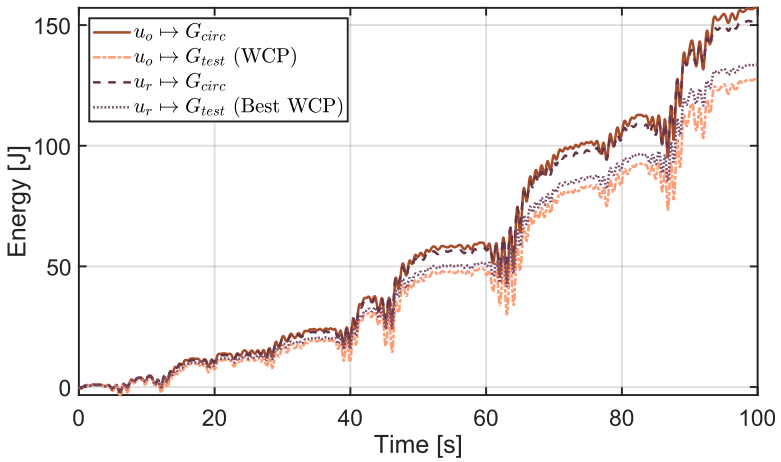

Figure 2.18: Time trace of the absorbed energy, applying different control input forces to the different nominal models.

- The solid red line represents the absorbed energy when $u_o(t)$ is applied to the nominal model $G_{circ}(\omega)$. This case is the ideal performance, where the optimal control input using nominal model $G_{circ}(\omega)$ is applied to the same nominal system.

- The orange dashed line represents the absorbed energy when $u_o(t)$ is applied to the nominal model $G_{test}(\omega)$. In particular, as the test model has been specifically selected, this case is the worst performance, where the optimal control input using the nominal model $G_{circ}(\omega)$ is applied to the nominal model $G_{test}(\omega)$.

- The dark purple dashed line represents the absorbed energy when $u_r(t)$ is applied to the nominal model $G_{circ}(\omega)$. In this case, the performance of the system has improved and absorbed energy of the system has moved closer to the absorbed energy for ideal performance.

- The purple dashed line represents the absorbed energy when $u_r(t)$ is applied to the nominal model $G_{test}(\omega)$. This case is the best worse-case performance for energy absorption.

Comparing the results of applying $u_r(t)$ to the two different nominal models, the impact of the correct selection of nominal model and uncertainty bound is highlighted. In robust control, applying $u_r(t)$, where the nominal model is based on the centre of the minimum radius circles ($G_{circ}(\omega)$), which corresponds to a small size of uncertainty bound, improves the control performance. Fig. 2.18 shows that the mean generated power, using the robust approach, is always non-negative, which is in accordance with the principle of non-consumption of power using robust approaches. In this study, nominal control also results in a positive mean absorbed energy, but in the general (non-robust) case, negative mean power 'production' can occur, for mismatched control/system models [23].

2.9 Conclusions

This study proposes a framework for estimating uncertainty in WEC systems with applications in robust control. With the objective of obtaining high-fidelity results from a CFD-based NWT, mesh refinement has been applied to the NWT setup proposed in [94], resulting in improved ETFE resolution considering the same experiments. The main contribution of this study is the synthesis of input signal types, and post-processing towards the aim of reducing conservatism in the WEC uncertainty description with the following results:

- Sinusoidal signals: Computing an ETFE with individual sinusoidal input signals and their corresponding output signals results in a high level of fidelity in terms of a low-variability ETFE, and satisfying the asymptotic nature of the phase response with minor errors which are addressed by applying ETFE refinement. It has been shown that there is no value in applying a BPF for the experiments showing distortion in the output signal. The major drawback for the experiments with individual sinusoidal signals is the high computational cost (relatively long simulation time).

- Chirp signal: The ETFEs obtained from LFM up-chirp input signals, and their corresponding output signals, show high variability, resulting in a large uncertainty region, while distorting the passive nature of the asymptotic ETFE properties. ETFEs obtained from input/output signals by pre-distorting the LFM up-chirp input signal, by modulating the input amplitude, resulted in a less variable ETFE, at low frequency. However, the resulted ETFE, computed from amplitude modulated LFM up-chirp signal, is not as smooth as the ETFE obtained from sinusoidal input signals. Moreover, the ETFE obtained from a NLFM down-chirp resulted in a highly variable ETFE at resonance and at high frequency. It has been shown that application of a BPF to the input/output signals is problematic, due to the difficulty of correct initialization of the filter output, resulting in unwanted additional transient behaviour artefacts.

- Multisine: ETFEs obtained from non-harmonic multisine signal show high variability. The application of Schroder's minimisation method to a multisine signal, with user selected frequencies, results in a highly-variable ETFE, with distortion of the amount of time spent at each frequency as a likely explanation. Thus, it can be concluded that achieving a balance between minimisation of the crest factor, and concentrating on the particular frequencies (non-harmonic multisine), is virtually impossible.

In the NWT experiments, proper input signal selection, application of ETFE refinement, and quantifying uncertainty by representative nominal model selection and uncertainty region estimation, results in a passive system representation and small uncertainty region, which improves robust control performance. The comparison of the overall energy absorption from this study and [94] highlights the improvement in the resulting controller performance.

Acknowledgement

The authors would like to acknowledge funding by Maynooth University of a *John and Pat Hume Doctoral (WISH) Award* for Mahdiyeh Farajvand and Science Foundation Ireland through the *Research Centre for Energy, Climate and Marine (MaREI)* under Grant 12/RC/2302_P2. The authors also gratefully acknowledge the Irish Centre for High-End Computing (ICHEC) for the provision of HPC facilities and support.

CRediT authorship contribution statement

Mahdiyeh Farajvand: Conceptualization, Methodology, Investigation, Formal analysis, Software, Writing - original draft, Writing - review & editing, Visualization. **Valerio Grazioso:** Conceptualization, Methodology, Investigation, Formal analysis, Software. **Demián García-Violini:** Methodology, Formal analysis, Software, Writing - review & editing. **John V. Ringwood:** Conceptualization, Writing - review & editing, Supervision, Funding acquisition, Project administration.

3

Representative linearised models for a wave energy converter using various levels of force excitation

Contents

3.1 Abstract

In guiding the progression, development, and operation of wave energy converters (WECs) in a more efficient way, mathematical analysis and understanding of the dynamic process is essential. Mathematical WEC models, obtained either by numerical analysis or physical modelling, form the basis of most (model-based) energy maximising control strategies available in the literature, where experiment design and system identification methodology directly impact the resulting model. This study, using an experimental-based WEC model (which can be used for linear control design), investigates the dynamic behaviour of a WEC by analysing the dominant poles of the system, generated using fully nonlinear computational fluid dynamics (CFD)-based numerical wave tank (NWT) experiments. The aim is to effectively track the dominant dynamics of the WEC, using different force-input amplitude levels in the NWT setup, and perform a comparison with the classical linear boundary-element-methods (BEM) equivalent methodology. Thus, the presented case studies are shown to agree with previously proposed model assessment of linear WEC models, based on a free-decay NWT setup. In addition, the representative WEC models determined as part of this study can be used for WEC controller design, either singly, or using a form of model/controller gain scheduling.

3.2 Introduction

Considerable modelling and testing is required for the development, optimisation, and power production assessment of wave energy converters (WECs). It is essential to accurately model WECs, and to measure, estimate, and monitor their dynamics in order to design effective (model-based) energy maximising control strategies, while preventing device damage due to undamped oscillations, or excursions beyond physical constraints, during operation. Developing a representative WEC model to describe body motion, wave-structure interaction, and the dynamics of different energy conversion stages is fundamental. Commonly used WEC models for control strategies are typically based on linear hydrodynamic models, either obtained from linear potential flow theory or data-driven system identification methodologies. Linear WEC models, based on boundary element methods (BEM), result in computationally attractive models commonly used for model-based control strategies, where the frequency-dependent hydrodynamic parameters are obtained under the assumption of inviscid, irrotational, and incompressible flow and *small body motion* (relative to the body dimension) around the equilibrium point. However, linear models, developed under these assumptions, and small wave

amplitude/steepness, are in conflict with the requirement of exaggerated device oscillations, as a consequence of the optimal energy-maximisation conditions [27]. In contrast, nonlinear approaches for mathematical modelling of WECs, reviewed in [90], point to techniques which can capture nonlinear hydrodynamic (and other) effects, and/or provide high fidelity data. Nonlinear WEC hydrodynamic effects can be handled using different strategies, namely, *partially* nonlinear methods, based on expansion of the linear model by including some nonlinear effects [102], *weakly* nonlinear methods, based on simplification of the fully nonlinear formulation [103], and *fully* nonlinear models [104]. Among modelling techniques in the field of WECs, computational fluid dynamics (CFD)-based analysis, capable of fully capturing hydrodynamic nonlinearities (consistent with the Navier-Stokes equations), is useful for high-fidelity modelling of WECs, but at great computational expense [105]. Nevertheless, CFD-based numerical wave tank (NWT) models have shown to be powerful tools, providing high-fidelity time-domain analysis of WECs, and power production assessment [34, 48].

In order to produce computationally simpler models, while considering WEC nonlinearity, recent efforts have aimed at the development of representative linear models, using system identification methodologies, from nonlinear NWT experiments, where the design of the NWT testing setup for data generation, and the employed system identification techniques, impact the resulting identified WEC model. This can be viewed as a data-based form of model reduction. For instance, [94] developed a framework to identify a nominal linear model for application of a robust control strategy from force-input CFD-based NWT (CNWT) experiments, following an empirical transfer function estimate (ETFE) methodology, essentially using a black-box identification method. Similarly, [106] proposed a solution for parameter identification of a state-space WEC representation from a series of (zero-input) decay tests in a CNWT setup. The study in [50] uses a linear modelling approach for WECs, combining high-fidelity CNWT simulations, system identification, and BEM-based modelling methods.

There is motivation to apply system identification strategies to wave energy modelling to characterise the movement of the WECs. The study in [41] considers system identification techniques and model validation procedures to calculate the WEC dynamics based on data from wave tank experiments. The FOAMM toolbox [67] provides an identification technique capable of computing parametric WEC models, which can characterise the system dynamics. This toolbox systematically implements a moment-matching [26] based identification strategy from nonparametric frequency-domain data.

The novelty of the present study is to model the state-space form of a WEC system and investigate the *dominant* dynamics, particularly considering *force-input* experiments in the CNWT setup. The FOAMM toolbox is used to implement the frequency-domain identification through the moments (key frequencies) of the ETFEs calculated from input/output data. Compared to similar studies in the literature, which use system identification based *free-decay* experiments in a CNWT setup [50], and basically focus only on parameters connected with inertia, restoring, and damping forces, the current study with appropriate selection of input force levels, covering the main range of frequencies and amplitudes of the device, is capable of determining a sufficiently representative model of the total system dynamics. Furthermore, as the force inputs acting on the WEC system for the system identification process are basically applied through the power take-off (PTO) system, the identified linear models can be used for linear model-based WEC control design. A comparison of the dominant dynamics from the force-input experiments with a BEM-based linear model is also performed, as a baseline. The overview of the sequences of steps to perform the dominant dynamics assessment from CNWT and WAMIT setups is outlined in Fig.3.1.

The NWT considered for the experiments is a modified version of the setup presented in [94] for system identification tests. Sinusoidal input signals, covering the most significant frequency range of the device and full input and output signal ranges, are used to provide the data for the system identification process.

Using different levels of input amplitude forces, WEC models are identified at each amplitude level and the dominant dynamics of the system, most notably the resonance frequency and pole location trends, have been tracked. Finally, a comparison of the dynamical behaviour of the system obtained with the presented study, using *force-input* NWT experiments, with equivalent *free-decay* NWT experiments as presented in [50], have been drawn.

The remainder of the paper is laid out as follows. Initially, standard linear modelling assumptions, as well as essential properties of WEC systems, are recalled in Section 3.3. The NWT specifications, used as the experimental setup, are provided in Section 3.4. Next, the experiment type, i.e. force-to-velocity experiments, used to obtain data for the system identification procedure, is detailed in Section 3.5. The system identification methodology applied to the generated data is presented in Section 3.6. The case study, including NWT features, the input force signals, and the results of the system identification and dominant pole analysis, follows in Section 3.7 and, finally, overall conclusions from the study are drawn in Section 3.8.

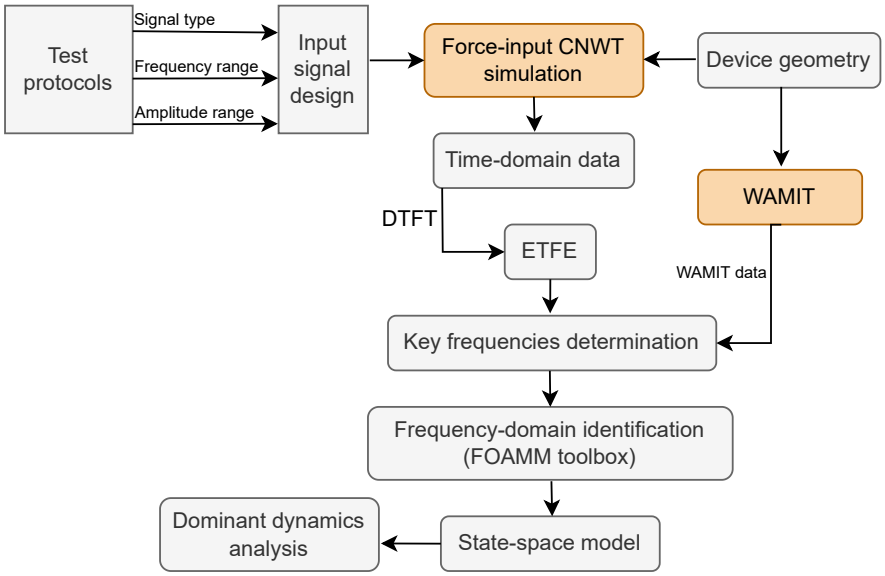

Figure 3.1: Overview of the sequences of steps to perform dominant dynamic assessment from CNWT and WAMIT setups.

3.3 Linear models for wave energy systems

Mathematical WEC models, under the assumption of linearity, are commonly studied using linear potential flow theory and the well-known Cummins' equation [87], where the motion of a single degree of freedom (DoF) floating structure, in the time domain, can be expressed as:

$$(m + m_\infty)\ddot{y}(t) = f_{\text{ex}}(t) - f_u(t) - k_{\text{h}}y(t) - h_{\text{r}} \star \dot{y}(t), \tag{3.1}$$

where $y(t)$, $\dot{y}(t)$, and $\ddot{y}(t)$ are the device displacement, velocity, and acceleration, respectively, with '$\star$' representing convolution. $f_{\text{ex}}(t)$ is the wave excitation force, produced by the action of incoming waves, $f_{\text{r}}(t)$ is the radiation force, arising from device motion in the fluid ($h_{\text{r}}(t)$ the radiation impulse response function), $f_u(t)$ is the control input applied by means of the PTO system, and k_{h} the hydrostatic stiffness, related to buoyancy/gravity forces. $m \in \mathbb{R}^+$ is the mass of the device and $m_\infty = \lim_{\omega\to+\infty} A_{\text{r}}(\omega)$ is the added mass at infinite frequency, where $A_{\text{r}}(\omega)$ and $B_{\text{r}}(\omega)$ are the so-called radiation added-mass and damping, respectively, defined from Ogilvie's relations [107] as:

$$\begin{aligned} A_{\text{r}}(\omega) &= m_\infty - \tfrac{1}{\omega}\int_0^{+\infty} h_{\text{r}}(t)\sin(\omega t)dt, \\ B_{\text{r}}(\omega) &= \int_0^{+\infty} h_{\text{r}}(t)\cos(\omega t)dt. \end{aligned} \tag{3.2}$$

Eq. (3.2) fully characterises the Fourier transform of $h_{\text{r}}(t)$, i.e.

$$H_{\text{r}}(\omega) = B_{\text{r}}(\omega) + \jmath\omega\left[A_{\text{r}}(\omega) - m_\infty\right], \tag{3.3}$$

where $h_r(t)$ and $H_r(\omega)$ denote a Fourier transform pair. Using Eq. (3.3), the model in Eq. (3.1) can be compactly expressed [61], in the frequency domain, as follows:

$$V(\omega) = \frac{1}{Z_i(\omega)} \left[F_{\mathsf{ex}}(\omega) - F_u(\omega) \right], \tag{3.4}$$

where

$$Z_i(\omega) = B_{\mathsf{r}}(\omega) + \jmath\omega \left(m + A_{\mathsf{r}}(\omega) - \frac{k_{\mathsf{h}}}{\omega^2} \right). \tag{3.5}$$

Considering the force-to-velocity mapping in the Laplace domain [21]:

$$G(s) = \left. \frac{s}{s^2(m + m_\infty) + s\hat{H}_{\mathsf{r}}(s) + k_{\mathsf{h}}} \right|_{s=\jmath\omega} \approx \frac{1}{Z_i(\omega)}, \tag{3.6}$$

where $H_{\mathsf{r}}(\omega)$ is commonly computed using boundary-element methods, such as WAMIT [108], and $\hat{H}_{\mathsf{r}}(s) \approx H_{\mathsf{r}}(\omega)$, for $s = \jmath\omega$, with $\hat{H}_{\mathsf{r}}(s)$ a stable linear time-invariant (LTI) system.

Cummins' equation can be implemented numerically directly by numerical convolution, or by first approximating the convolution term in state-space sub-system form and then calculating the state-space representation of Eq. (4.1), according to the study in [50]:

$$\dot{x}(t) = Ax(t) + B\mathrm{u}(t), \quad y(t) = Cx(t) + D\mathrm{u}(t), \tag{3.7}$$

In Eq. (3.7), $x(t)$ is the state vector and the function $\mathrm{u}(t)$, defined as $\mathrm{u}(t) = f_{ex}(t) - f_u(t)$, is the input of the system. A, B, C, and D are the state (dynamic), input, output, and direct transmission matrices, respectively. Matrix D is a null matrix (zero matrix), as $G(\jmath\omega)$ in Eq.(6) is strictly proper (for real (physical) WEC systems the matrix D is the null matrix).

3.3.1 WEC systems essential properties

After defining the WEC model, it is crucial to consider the fundamental properties which are key drivers for dynamic system analysis and synthesis. Fundamentally, WECs are characterised by the properties of stability and passivity [59].

3.3.1.1 Stability

Maintaining the stability of WEC structures exposed to external loading with different frequencies and amplitudes is one of the main priorities. Stability analysis of WECs has been carried out using different strategies. [60] stabilises unstable identified models by means of reflecting the unstable poles in the imaginary axis (reflecting from the right-hand side to the left-hand side of the complex plane) and reconstructing the model. Another methodology for guaranteeing stability is proposed in [50] by applying constraints on the model parameters.

3.3.1.2 Passivity

Passivity (related to stability of systems), is a particular case of 'dissipativity', arising from an intuitive interpretation of system behaviour. The concept is formalised based on the physical energy process of the system, assuming that any increase in the system energy is purely from external sources. Passivity for LTI systems can be guaranteed with the phase range saturated to $\pm 90^{\circ}$ degrees *for the complete spectral domain*, based on Bode plot shaping, or with a positive real transfer function for all frequencies [62, 59];

$$G(\jmath\omega) + G^{H}(\jmath\omega) > 0, \ \forall\omega \in \mathbb{R}, \tag{3.8}$$

where the symbol H denotes the self-adjoint matrix (Hermitian), and equivalently for SISO systems:

$$\mathbb{R}\mathrm{e}\left(G(\jmath\omega)\right) > 0, \ \forall\omega \in \mathbb{R}, \tag{3.9}$$

so the entire Nyquist plot lies in the right-half plane. Then, the transfer function is given, using the state-space representation in Eq. (3.7), as follows:

$$G(s) = C\left(sI - A\right)^{-1} B + D, \tag{3.10}$$

while the passivity of the system (Eqs. (3.7) and (3.10)) is guaranteed with a passive sub-state space representation for the radiation structure, in Eqs. (3.2) and (3.3) [59]. A recent practical passivisation methodology, considering the passivity of nominal linear and uncertainty models for a WEC, is proposed by [63] for the application of a robust spectral-based control methodology.

3.4 Numerical wave tank

The three-dimensional NWT setup considered for this study uses a point absorber-type WEC. To simplify the NWT illustration, analysis, and identification test, the WEC structure consists of a single degree of freedom, only oscillating in heave, which also eliminates potential effects of motion coupling. For the specific application of system identification tests, the tank is designed with equal spans in the x and y-directions (perpendicular to the tank depth, in the z-direction), and the buoy is located in the centre of the tank corresponding to $(x, y, z) = (0, 0, 0)$. To avoid reflections of the WEC-induced waves, the tank is equipped with wave absorbers, at the left and right boundaries ($x = \pm L/2$), consistent with the operation of the NWT in a wave flume mode [27]. The tests are performed by applying a defined external input force ($f_u(t)$)

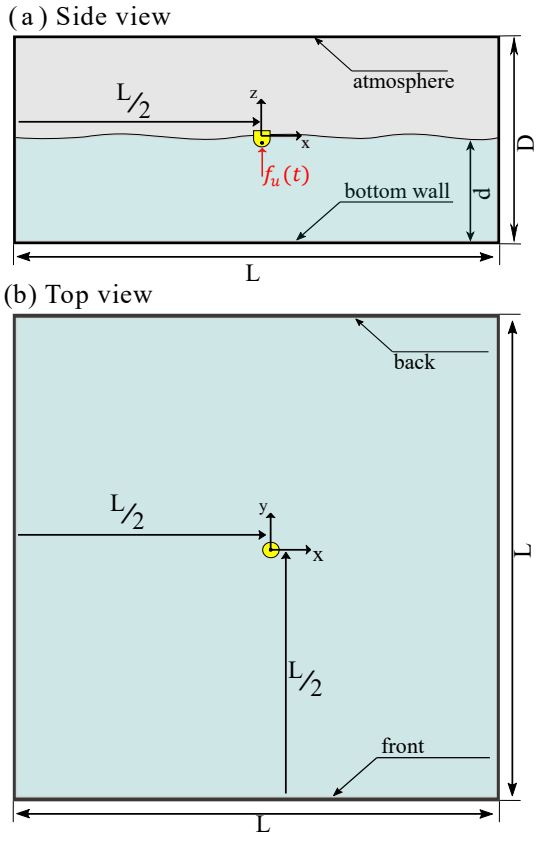

Figure 3.2: Schematic of the numerical wave tank for (a) Side view (b) Top view.

directly to the WEC to induce WEC motion. The side view and top view of the NWT are shown in Fig. 3.2 (a) and (b), respectively, where L is the tank length in x- and y-directions, D and d are the tank, and water, depths, respectively. The tank length is designed to be six wavelengths of the most significant radiated waves (occurring at peak frequency of the radiation damping of the WEC), under the assumption of deep-water conditions. The symmetry configuration of NWT in both the x- and y-directions allows the CFD simulation to be carried out on a *quarter of the full NWT*, with a significant reduction in computation time. NWT mesh generation uses the *blockMesh* utility supplied with OpenFOAM, with finer meshes around the WEC boundary, gradually getting coarser towards the NWT boundary. NWT simulation is implemented using the mesh-based CFD method via numerical solution of the Navier-Stokes (NS) equations [94] in OpenFOAM.

3.5 Force-to-velocity experiments

In this study, the input/output data, for system identification and dynamical assessment of the WEC structure, are taken from the CNWT, with the buoy motion resulting from a defined external input (PTO) force, applied directly to the WEC.

Due to the nonlinear nature of the fluid/structure interaction, the input force is designed in a way to cover the complete range of frequencies and amplitudes corresponding to typical scaled (Froude scaling with a scaling factor of 1/30th, emulating the full-scale conditions at the AMETS test site in Bellmullet, Co. Mayo, off the West Coast of Ireland [101]) operational conditions, in order to obtain a complete hydrodynamic representation of the system. Consequently, exciting the system by applying the input force (PTO force), $f_u(t)$, generates a corresponding output (velocity), $v(t)$, in the time domain, both of which are used to identify the so-called *force-to-velocity* mapping. In this study, a frequency-domain representation, from the time-domain input/output data of the NWT simulations, is obtained through calculation of the discrete-time Fourier transform (DTFT) of input and output signals, at the frequencies at which the spectral analysis is required.

3.6 System Identification Method

The objective of system identification is to model the system from the measured input/output signals. The identification procedure can produce either parametric or non-parametric models where, in the parametric case, the dynamic behaviour of the system is described by partial, or ordinary, differential equations. In the non-parametric case, the system response is obtained directly, or indirectly, from experimental data, in time- (impulse response) or frequency-domain (frequency response). A frequency-domain empirical transfer function estimate (ETFE), representing the system frequency response, offers a non-parametric representation of the system dynamics, computed by dividing the DTFT of the output with $F_u(\omega)$, the known DTFT of the input, as:

$$\mathrm{ETFE}(\omega) = \frac{\mathrm{DTFT}(v[n])}{F_u(\omega)} \tag{3.11}$$

Note that, in Eq.(3.11), the discrete-time Fourier transform is employed, since the (sinusoidal) frequency is known, with just the amplitude and phase to be determined. Furthermore, the DTFT of the input signal, $F_u(\omega)$, is trivial (user defined sinusoidal input signal with known amplitude and phase), so these parameters are substituted directly.

The DTFT calculates a frequency-domain representation of a signal at a single frequency point. The DTFT of a sequence of N equispaced samples of a finite discrete-time series signal $v[n]$[1] ($v[n] = v(nT_s)$ where T_s is sampling period),

[1] From now on, the notation [] refers to discrete samples

considering a sequence of N samples, where $0 \leq n \leq N-1$, is depicted as $V(e^{j\omega})$ with ω being the real frequency variable ($0 \leq \omega \leq 2\pi$), defined as

$$V(e^{j\omega}) = \sum_{n=0}^{N-1} v[n]w[n]e^{-j\omega n}, \tag{3.12}$$

where $w[n]$ is a window function. Note that, in calculating a short-term Fourier transform, it is customary to employ a non-rectangular window function to reduce the effect of spectral leakage, caused by the abrupt start and finish of the data record. The choice of window function is discussed further in Section 3.6.1.

Regarding parametric models, a useful classification [66], considering the connection of the model to physical (parametric) quantities, is:

- White-box, where all the parameters of the physical system are estimated from the data,
- Grey-box (and the sub-classes of off-white, smoke-grey, steel-grey and slate-grey), where the generic model structure has some connection to the physical model at various levels, and
- Black-box, where the model structure, capable of reproducing the experimental output data, excited with the same input, cannot be physically interpreted, which means that its states have no connection to the physical world.

In general, no hydrodynamic models are truly white-box, in that there is no direct relationship between the physical system parameters and the hydrodynamic 'coefficients', which are usually provided in non-parametric frequency-, or time-domain, as in (3.5). However, hydrodynamicists may be more comfortable with the individual determination of the non-parametric hydrodynamic quantities corresponding to added mass (A_r) and radiation damping (B_r). For a system identified purely from data, the models are usually limited to black- or, at best, grey-box, where some information about the likely order of the model can be used to specify the structure of the parametric model.

3.6.1 Window function

A non-rectangular window function is used both to alleviate the effect of spectral leakage due to abrupt termination of the short-term data segment (at both ends), while also minimising the effect of the leading transient in the output signal. A well-known window function, used in conjunction with a short-term Fourier transform, is the Tukey window (tapered cosine window) which is generated by convolving a

cosine lobe with a rectangular window. The time-domain representation of the Tukey window [65] is:

$$w[n] = \begin{cases} 1, & 0 \leq |n| \leq (1-\alpha)\frac{N}{2} \\ 0.5\Big[1 + \cos\Big(\frac{\pi(n-(1-\alpha)\frac{N}{2})}{\alpha\frac{N}{2}}\Big)\Big], & (1-\alpha)\frac{N}{2} \leq |n| \leq \frac{N}{2} \end{cases} \tag{3.13}$$

where α $(0 \leq \alpha \leq 1)$ is a parameter controlling the gradual change between a rectangular window ($\alpha = 0$) and a Hanning window ($\alpha = 1$). The application of the Tukey windowing directly affects the magnitude of the signal in the spectral domain. To compensate for the amplitude distortion due to windowing, an amplitude correction factor is applied, based on a gain calculation by dividing the amplitude of the *known* sinusoidal input signal by magnitude of the Tukey-windowed sinusoidal signal in spectral domain.

3.6.2 Moment-based system Identification

A particular, frequency-domain, system identification strategy, specifically oriented to WEC modelling, is the FOAMM [67] MATLAB toolbox, which identifies a parametric model (in state-space form) for WEC dynamics, based on a moment-matching approach. A notable feature is the ability to pre-specify particular key frequency points at which exact matching between the parametric model and the non-parametric ETFE is achieved, which can include the device resonant frequency. In addition, the asymptotic behaviour of the model can also be guaranteed by matching at extreme (low/high) frequency values. The FOAMM toolbox, based on finite-order hydrodynamic approximation by moment-matching, is a user-friendly platform allowing parametric system identification for either the radiation convolution term in (3.1), or the complete force-to-motion WEC dynamics in (3.5) [67]. In this study, the FOAMM toolbox is used to identify a state-space model for the complete (force-to-motion) WEC dynamics.

3.7 Case study

The structure considered for this study is a point absorber-type WEC with the physical properties shown in Fig. 3.3. The buoy has an axisymmetric cylindrical geometry, with both radius and height of 0.25m, and a hemispherical bottom with radius 0.25m. The mass of the device is 43.67kg, and the centre of the mass is located at a vertical distance of 0.191m from the bottom-most point of the buoy. For CNWT simulation, the buoy is located at the centre of a 6m deep tank with a water depth of 3m as shown in Fig. 3.2. The tank spans a length of $L = 14$m

in the x- and y–directions, designed to be six wavelengths of the waves occurring at the peak frequency of the radiation damping of the WEC $(4.56$ rad/s), obtained from NEMOH [109]. The NWT setup is a modified version of that used in [94], with further mesh refinement applied to ensure the fidelity of the NWT simulation. The smallest buoy displacement resulting from the input force is used to design the mesh sizes around the buoy, with a minimum cell dimension of 0.0054m (3 cells per smallest displacement, induced by the smallest force amplitude at high frequency asymptote), giving a total number of NWT cells of 4.06 million. (For a screen shot of the spatial discretisation and computational mesh of the NWT, the intrested reader is referred to [29]).

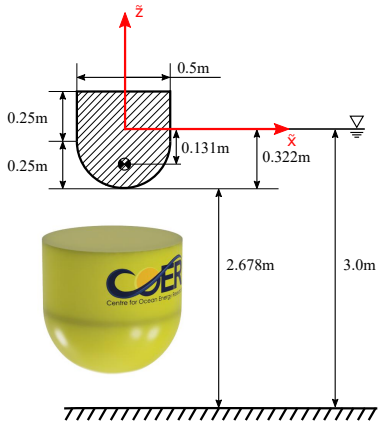

Figure 3.3: Schematic of the considered WEC structure

The input excitation force is monochromatic sinusoidal, $f_u(t) = A\sin(\omega t)$, where A and ω are the amplitude and frequency of the sinusoids, respectively. Considering the limitations of the NWT dimensions, and the simulation duration, pure sinusoidal signals have been shown to provide high-fidelity representation of the system in terms of ETFE (for a detailed input signal synthesis to characterise dynamical uncertainty in WEC systems, the interested reader is referred to [29]), which is a result of spending sufficient time at each frequency (low frequency variation ratio, i.e. high signal spectral permanency.) However, a relatively long experimentation time is required to cover the complete amplitude and frequency space. In this study, the sinusoidal excitation signals comprise a total of 96 individual experiments, combining the amplitude set $A_i = \{20, 40, 60, 80, 100, 120\}$N with frequencies $\Omega_j \in \{0.2, 1, 2, 3, 4, 4.5, 5, 5.5, 6, 6.5, 7, 8, 9, 10, 18.89\}$rad/s, plus a specific resonance frequency tailored to each amplitude set. This selection of frequencies and amplitudes gives a smooth representational transition between the ETFE points corresponding to discrete values of amplitude/frequency. The frequency range covers the complete dynamical range (with respect to the resonance frequency), and the amplitude

range selection, ranging from linear behaviour (smallest amplitude) to amplitudes almost forcing the device out of the water (largest amplitude) and intermediate values, covers a full dynamical characterisation of the nonlinear system. Moreover, the amplitude set A_i perfectly covers the the amplitudes corresponding to scaled (scaling factor of 1/30th) operational conditions at the AMETS test site [101] with the maximum excitation force amplitude of 60N [27]. Each experiment is driven by a finite set of N time-domain samples of input signals (exciting force signals) that generate a corresponding set of N output samples (which in this case are heave velocities). The NWT simulation interval of the sinusoidal experiments is $[0, 25]$s which guarantees enough spectral permanency time at each frequency and avoids wave reflections [94]. By way of example, input/output time domain analysis for two sample experiments, with an amplitude of 20N and frequencies of 1 rad/s and 5.84 rad/s (the resonance frequency of the system corresponding to a 20N input amplitude force), is presented in Fig. 3.4. The transient response

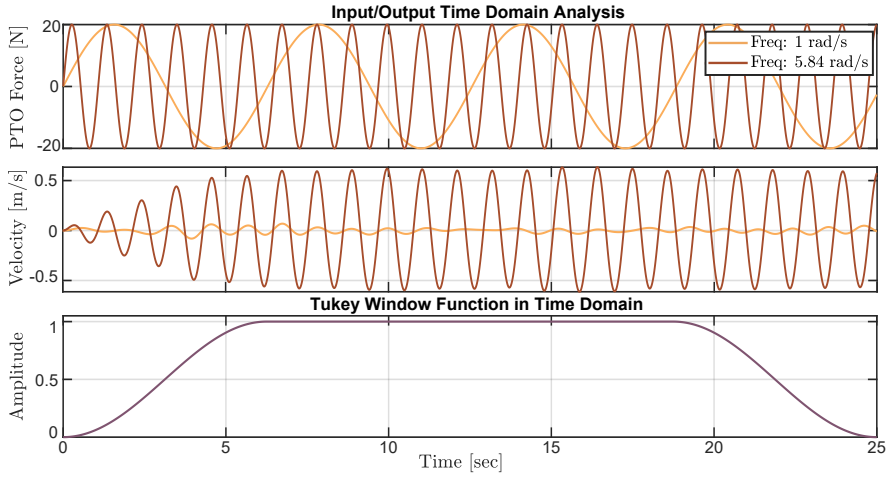

Figure 3.4: Time traces of the input/output signals in the CNWT for sinusoidal input signals with amplitude of 20N and frequencies of 1rad/s and 5.84rad/s, along with Tukey ($\alpha = 0.5$) window profile.

in the velocity time trace corresponding to a 20N input signal, at 5.84 rad/s, is mitigated by the application of a Tukey window. Considering the longest transient response among the output time-domain signals from the 96 experiments, a Tukey window according to Eq. (3.13) with $\alpha = 0.5$ is applied, also shown in Fig. 3.4. Each series of experiments generates a single frequency point in the ETFE (Eq. (3.11)) of the system, obtained from the calculation of the DTFT of the output signal $v(t)$ and the known amplitude and phase of the sinusoidal input signal ($f_u(t)$). ETFEs, covering the complete amplitude range A_i, and their corresponding frequency ranges, with further ETFE refinement (based on the physical principles articulated

in Section 3.3.1) are obtained based on: A) ETFE phase components are corrected to 90° and -90° at the low and high-frequency asymptotes, respectively, and B) The system phase is forced within ±90° degrees *for all frequencies*, respecting the passive nature of the system.

The ETFEs, and their interpolation across frequency points using piecewise cubic Hermite interpolating polynomials (PCHIPs), are shown in Fig. 3.5.

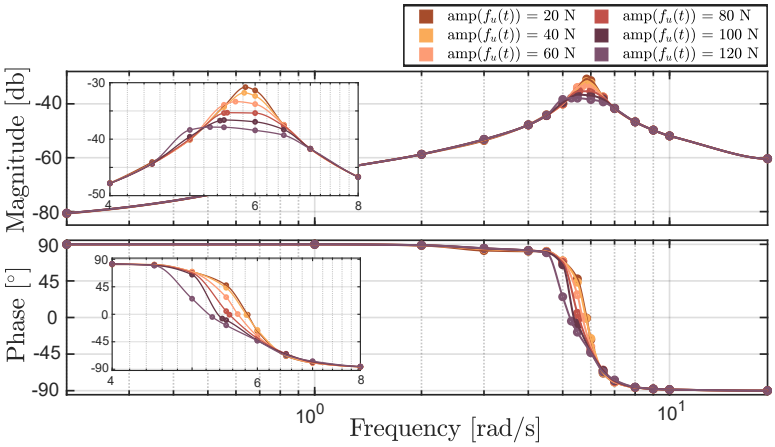

Figure 3.5: ETFEs of the CNWT experiments using sinusoidal input signals with 6 amplitude levels.

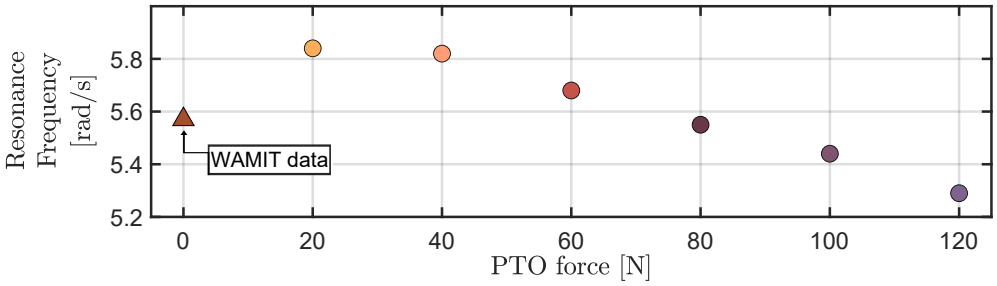

Figure 3.6: Resonance frequency corresponding to different amplitude levels of input signals.

Due to nonlinearity, different levels of input signal amplitude result in different ETFEs. One major characteristic observed from the determined ETFEs is an increasing trend of the bandwidth, and a decreasing trend of the peak frequency response (resonance frequency), as the amplitude of the input signal increases. It can be concluded that, as the amplitude of the input force gets larger, the resonance frequency decreases, and the damping ratio increases. The resonance frequency, corresponding to each amplitude level (from CNWT data), is presented in Fig. 3.6, showing a decreasing resonance frequency trend with increasing input signal amplitude. The results of the resonance frequencies from force-input experiments are also compared with the resonance frequency from WAMIT

data (effectively zero input amplitude) in Fig. 3.6. Note that the resonance frequency obtained from WAMIT (infinitesimally small amplitude) data violates the expected resonance frequency trend, suggesting that a WAMIT model may not provide a representative model of the system, even at relatively low excitation amplitudes. (However, due to extreme computational effort and higher mesh resolution requirement, the convergence towards the 0N point is not resolved beyond the $amp(f_u(t)) = 20$N point.)

3.7.1 System Identification Results

State-space representations of the WEC system, at different force levels, are obtained using the FOAMM [26] toolbox, where three 'cardinal' points of each ETFE, i.e., low-frequency asymptote, resonance frequency, and high-frequency asymptote, are selected manually as inputs to the FOAMM toolbox. The order of the output system will be twice the number of selected frequencies (6^{th} order in this case) with exact frequency matching based on the selection of the desired set of frequencies (e.g. the resonance frequency) in the manual mode. By way of example, the state, input, and output matrices of the state-space model according to Eq. (3.7), obtained for an $80N$ input level, are:

$$A = \begin{bmatrix} -692.92 & 693.12 & -692.92 & 692.92 & -692.92 & 692.92 \\ -640.69 & 640.49 & -640.49 & 640.49 & 640.49 & 640.49 \\ -0.51 & 0.51 & -0.51 & 6.01 & -0.51 & 0.51 \\ -7.05 & 7.05 & -12.55 & 7.05 & -7.05 & 7.05 \\ -19.00 & 19.00 & -19.00 & 19.00 & -19.0 & 37.89 \\ -13.96 & 13.96 & -13.96 & 13.96 & -32.85 & 13.96 \end{bmatrix},$$

$$B = [692.92 \quad 640.49 \quad 0.51 \quad 7.05 \quad 19.00 \quad 13.96]^\top,$$

$$C = [0.00 \quad 0.00 \quad 0.01 \quad -0.01 \quad 0.00 \quad 0.00],$$

respectively, with corresponding pole pairs:

Pole pairs of the 6^{th} order system
-0.51 ± 5.50i
-12.46 ± 12.21i
-12.48 ± 12.36i

The frequency response of the obtained parametric model using the FOAMM toolbox (solid-red), (which will be used to perform the dominant dynamical assessment), along with the target frequency response (dashed-blue), and the interpolated frequencies (green-dots), for all the input amplitude forces, are shown in Fig. 3.7. The identified system fits well with the actual system, for low input amplitudes, and the error between actual and identified models, calculated in terms of the

Mean Absolute Percentage Error (MAPE), gets larger as the input amplitude increases, recognising the increasing difficulty of fitting a linear model for greater input amplitudes. The same identification procedure is applied to a WEC model obtained from WAMIT (zero-input signal) in order to compare the results. The MAPE between actual and identified models, corresponding to each input amplitude level, is presented in Table 3.1. Note that the MAPE value, corresponding to each input amplitude level, depends on the manual selection of the desired (matching) frequency points chosen in the FOAMM toolbox.

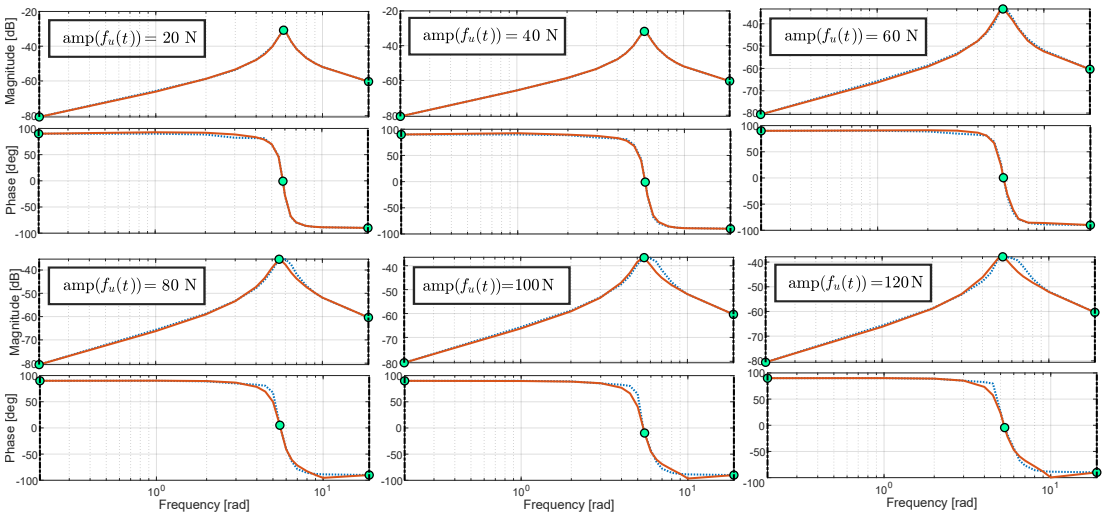

Figure 3.7: The frequency response of the obtained parametric model using FOAMM toolbox (solid-red), along with the target frequency response (dashed-blue), and the interpolated frequencies (green-dots) for all the input amplitude forces.

Table 3.1: The MAPE between actual and identified $6th$ order models corresponding to each input amplitude level .

Input signal amplitude [N]	MAPE
0 (WAMIT)	0.000895
20	0.029779
40	0.027002
60	0.075799
80	0.115651
100	0.155575
120	0.164085

3.7.2 Dominant pole analysis

The identified systems in Section 6.2. are used to locate the least damped (slowest) poles, which most affect the behaviour of the dynamic system. For a stable linear system, the relative dominance of the poles is determined by the ratio of the real parts of the poles nearest the $j\omega$ axis, where the suggested value is $3-5$ in [110] and [111], and 10 in [112]. As the requirement that a ratio > 3 may not be fulfilled, the ratio of the real parts of the poles > 5 is assigned where the pole (or complex pair) with the smallest real part, i.e. closest to the imaginary axis, is the dominant pole (or complex pair), and other poles may be regarded as relatively insignificant. A pole dominancy condition for each input amplitude level (including three pairs of complex conjugate poles for each of the 6^{th} order identified models) is considered. Pole dominance, for the models corresponding to each input amplitude level, is calculated by the ratio of the real parts of the two pole pairs closest to the imaginary axis, with results listed in Table 3.2. For the models obtained with input force amplitudes of $20N$, $40N$, $60N$, and $120N$ the closest pole pairs to the imaginary axis cannot be truly considered as dominant poles, but the pole dominancy condition is satisfied for the models corresponding to 0N (the WAMIT model), 80N and 100N input amplitudes. There is no clear trend of pole dominance with respect to the input signal amplitude, which can be possibly due to the obtained identification error, computed in terms of MAPE, between the target and identified frequency responses. In particular, for some cases, the identification error is larger in the region around resonance while, for other cases (higher input forces), the error is more significant at the extremes of the frequency range, considered for error computation, as represented in Fig. 3.7.

Poles closer to the imaginary axis represent slower modes, indicating a lower damping effect. The least damped pole pairs (closest pole to the imaginary axis), corresponding to the identified models of all input amplitude levels, along with the dominant pole pair obtained from the WAMIT model, are presented in Fig. 3.8. Since the magnitude of the real part of the least damped poles of the models show an increase as the input amplitude force increases, it can be concluded that larger input amplitudes correspond to stronger damping (possibly due to viscous effects). Note that a linearised viscous damping effect can be approximated using Lorentz linearisation [113].

Note that the least damped pole locations, corresponding to the smallest input amplitude force (close to a truly linear model), is very similar to the dominant pole of the WAMIT model, indicating the relative accuracy of the WAMIT model for representing the WEC model excited with very small input amplitude forces. However, the WAMIT model fails to provide a representative model of the system

dynamics when the device is subject to high input amplitude forces, typical of a WEC in power production mode. However, the convergence of the CFD-derived pole locations on the WAMIT poles, for small input amplitude provides a degree of validation of the modelling method, and is similar to results obtained for free-response tests [50].

In Fig. 3.8, a gentle trend in the values of the imaginary components of the least damped poles can be observed, essentially related to the oscillatory frequency in the response. The trend of the imaginary component of the least damped poles is similar to the resonance frequency trend presented in Fig. 3.6, i.e. the imaginary component of the least damped poles decreases as the input amplitude increases, and a discrepancy of the trend is observed with the zero-input data, obtained from the WAMIT model. In a 2^{nd} order system, the imaginary component of the pole corresponds to the value of $\omega_n \sqrt{1-\zeta^2}$ (the damped 'natural' frequency), where ω_n is the natural frequency of the device, related to the resonance frequency of the system ($\omega_n \sqrt{1-2\zeta^2}$) (depicted in Fig. 3.9 in three-dimensions), and ζ is the damping factor. In this study, there is no clear relationship between the imaginary components of the least damped poles and the resonance frequencies obtained from ETFEs (Fig. 3.6). A possible explanation related to the error of approximating the system model using the FOAMM toolbox, and the fact that the least damped poles are not truly dominant poles for all models. Imaginary component values, for the least damped poles corresponding to input signal amplitudes, are presented in Table 3.3.

Table 3.2: Pole dominance assessment for system models corresponding to different input amplitude levels.

Force amplitude $[N]$	Ratio of the real parts of the poles	Pole dominance
0 (WAMIT)	12.56	✓
20	3.92	×
40	4.51	×
60	2.04	×
80	24.12	✓
100	5.07	✓
120	4.46	×

One particularly significant result obtained in this study is the similarity of the trend of the least damped poles location of the force-input CNWT experiments and WAMIT model (Fig. 3.8) to the dominant poles location trend obtained from free-decay CNWT experiments and a BEM presented in [50] (Fig. 14). This provides some level of cross validation, though both sets of results are obtained using different stimulii (forced input Vs non-zero initial condition).

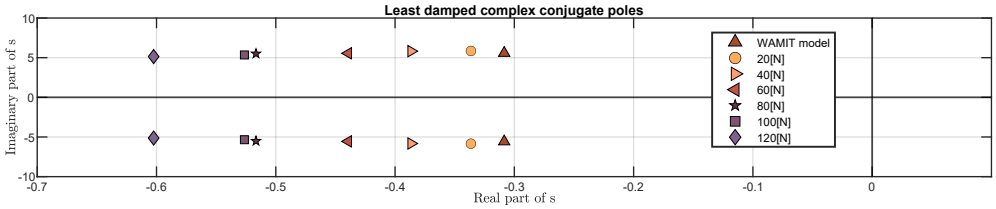

Figure 3.8: Location in the complex-plane of the least damped model poles.

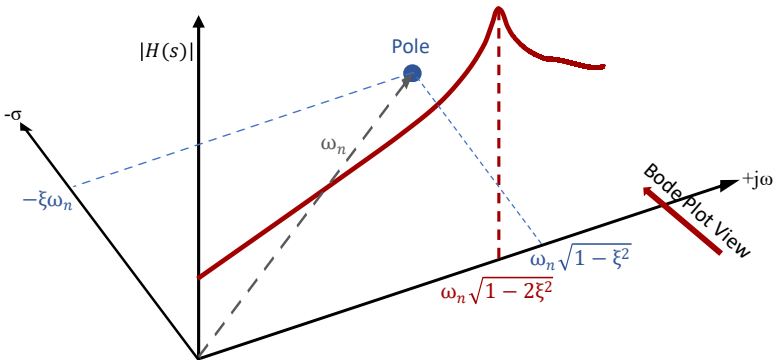

Figure 3.9: 3D view of pole diagram and Bode plot

Table 3.3: Imaginary components of the dominant poles corresponding to input signal amplitudes.

Input signal amplitude $[N]$	Imaginary part of the least damped poles
0 (WAMIT)	5.580
20	5.845
40	5.819
60	5.554
80	5.508
100	5.343
120	5.136

3.8 Conclusion

In this study, representative linearised WEC models are investigated by performing system identification using force input (PTO force) CNWT experiments. Considering the true complexity of real WEC models (viz the NS equations), force-input experiments, with careful design of input signals to cover the full range of frequencies and amplitudes likely to be encountered during system operation, are capable of providing a sufficiently *representative linear* model set that can be used for dynamical assessment of WECs, and for model-based control design, using either a single representative model, or some form of gain scheduling [114], interpolating

between models/controllers. The following conclusions can be drawn regarding the dominant dynamical assessment of the WEC system:

- Analysis of the resonance frequency of the system, from the ETFE results of the input-force CNWT experiments and WAMIT data, shows an increasing trend in resonance frequency as the amplitude of the input force decreases, with a small deviation in the trend due to a less representative model obtained from WAMIT data.
- Investigation of the least damped poles of the system sheds light on two important dynamical behavioural aspects of the system: *A)* The real part of the least damped poles gets closer to the imaginary axis, indicating a lower damping effect, as the amplitude of the input-force decreases, and *B)* The imaginary part of the least damped poles is related to the resonance frequency, and thus shows the same trend as the resonance frequency.
- The trend obtained from the force-input CNWT experiments (and WAMIT model), for the real part of the least damped poles of the system, is very similar to the results obtained from the free-decay CNWT experiments (and BEM model) reported in [50].

Finally, a dominant 2^{nd} order WEC model has been shown to have utility in the design of relatively simple controllers for WECs [115], while variations in real parts of poles can be traced to implications for sensitivity and robustness [30].

Acknowledgement

The authors would like to acknowledge funding by Maynooth University of a *John and Pat Hume Doctoral (WISH) Award*, for Mahdiyeh Farajvand, and Science Foundation Ireland through the *Research Centre for Energy, Climate and Marine (MaREI)* under Grant 12/RC/2302_P2, for John Ringwood. The authors also gratefully acknowledge the Irish Centre for High-End Computing (ICHEC) for the provision of HPC facilities and support.

CRediT authorship contribution statement

Mahdiyeh Farajvand: Conceptualization, Methodology, Investigation, Formal analysis, Software, Writing - original draft, Writing - review & editing, Visualization. **Demián García-Violini:** Methodology, Formal analysis, Software, Writing - review & editing. **John V. Ringwood:** Conceptualization, Writing - review & editing, Supervision, Funding acquisition, Project administration.

4

Non-parametric multi-linear frequency-domain modelling of a wave energy device from experimental data

Contents

4.1 Abstract

In experimental wave tank tests of wave energy converter (WEC) devices, uncertainty sources arising from the inherent nature of the dynamical system, or disturbance sources due to external factors, are inevitable. It is essential to employ proper signal processing techniques to mitigate effects due to external disturbances to establish realistic WEC models from experimental tests. Careful estimation of a range of representative linearised models, or determination of a nominal model and associated uncertainty region, overcomes the limitations of a single linear model (using first principles) by covering the complete dynamic operational space of the device. In pursuit of this goal, the current study analyses physical wave tank data using force-input experiments obtained from an experimental campaign (at Aalborg University) involving a 1/20 scale Wavestar prototype device. In the frequency

domain, non-parametric multi-linear hydrodynamic WEC models are characterised, serving as a starting point for model-based linear WEC robust controller synthesis. Specific focus is directed towards the quantification of uncertainty and external disturbance, specifically tailored to the wave tank under study. Effective data pre-processing steps (in the time-domain) and post-processing steps (in the frequency-domain), adopted for chirp type signals, are applied to mitigate disturbances while preserving the underlying physical system behaviour. Moreover, data contamination levels at different operating conditions of the system are quantified to highlight the contamination dominancy that can be tolerated to obtain realistic multi-linear WEC models. Finally, as an application example of non-parametric multi-linear WEC models obtained from this study, a single nominal model and uncertainty bound are determined that could provide the basis for (linear) robust WEC control.

4.2 Introduction

Wave energy converter (WEC) mathematical models find diverse applications, such as performance prediction, device optimisation, power production assessment, and as a basis for model-based control design. WEC models can be developed through numerical simulations, full-scale tests, or laboratory-scale tests, each presenting distinct methodologies, complexities, and challenges. These diverse modelling routes yield models characterised by a range of accuracy and levels of uncertainty with consequences for (model-based) control strategies [30, 31]. Among different methods, linear WEC models (using first principles), only being valid for small motions around the equilibrium point, and thus violating the required exaggerated motion for WEC energy maximisation [27], fail to represent proper WEC behaviour under control actions. While the determination of models from data (using either physical or numerical experiments) has been shown to be an effective route to derive representative (linear and nonlinear) WEC models [41, 42, 43]. In wave tank experiments, the selection of test signals determines the valid operational space of the model [68], ensuring it meets the dynamic requirements of a control system. Nevertheless, many parameters can cause uncertainty in the data-driven models capturing the nonlinear dynamics of the power conversion chain (different conversion stages) of a WEC that may hinder the lack of adequate WEC models for efficient (model-based) control strategies. In numerical modeling, the limitations of the governing equations in describing the physics, the level of approximation of the numerical methods, and numerical implementation (e.g. numerical wave tank model setup, grid generation) are the main contributors of uncertainty sources

[33]. In physical wave tank (PWT) tests, scale effects (e.g. viscosity), measurement uncertainty (direct measurements, calibration), tank setup biases (boundaries, facilities), model effects (geometry, installation, mooring lines, power take-off) are the main sources of uncertainty [116].

In the field of WECs, various studies have considered uncertainty at different stages. To briefly summarise, in [72], quantitative uncertainty bounds in different wave and environmental conditions are provided, resulting in a considerable impact on minimising uncertainty in power and mooring line tension predictions. The study in [73] quantifies the uncertainty associated with numerical ocean wave simulations using a stochastic framework based on generalised polynomial chaos. Inaccuracies stemming from (limitations of) linearity assumption for modelling the motion response amplitude operator of a semisubmersible platform are taken into account, based on the Bayesian inference method, in [38]. The influence of (phase) control of WECs, on the numerical uncertainty (spatial discretization, temporal, and iterative errors) in CFD simulation for passive control of WECs, is investigated by [117]. Uncertainty of a WEC plant dynamics is investigated in [97], using generalised polynomial chaos, for uncertainty quantification, while the study by [96] estimates the dynamic uncertainty in an online manner, followed by computationally efficient robust adaptive optimal control, suitably coping with modelling uncertainties. A recent study on the determination of representative linear models, and quantification of uncertainty region using high-fidelity numerical wave tank (NWT) experiments, with a special focus on input signal synthesis and signal processing techniques with the aim of reducing conservatism of the controller, is presented by [29]. It is worth noting that canonical frameworks for uncertainty quantification can be used to adequately address certain control studies, such as $\mathcal{H}_\infty$-based designs. Particularly, a multiplicative uncertainty scheme is used in [118] to quantify the uncertainty level, relative to the magnitude of the system, in an energy maximization control problem using the spectral methodology introduced by [23]. For a more detailed discussion, the interested readers are referred to [118].

PWTs are one of the most important test setups undertaken for the physical evaluation of performance, model validation, and control. Considering different wave conditions and WEC types, WEC *model validation*, focussing on the accuracy of numerical models [52, 53, 55, 54], and *model invalidation*, enabling the independent analysis of dynamic uncertainty and external noise within experimental datasets, by comparing simulated responses with experimental data [56] have been topics of focus for some researchers. It is of paramount importance to have knowledge of the uncertainty associated with numerical models, in order to obtain accurate results for model validation. The contamination nature, the range of tests that can be

performed, and the range of post-processing techniques that can be applied, differ significantly in NWT and PWT tests. It is generally believed that agreement between simulation and experiments is usually good in small to moderate sea states, see [38, 36, 37], with discrepancy increasing in severe sea states, or in wave conditions that excite resonances (due to non-linear effects). Such discrepancies can result in overestimation of the dynamic response, and energy absorption [36]. Nevertheless, some studies have noted large experimental uncertainty at low levels of excitation as in [40], where the dominant level of (non-hydrodynamic) experimental load measurements contaminates data at low-speed foil velocity of a WEC, or as in the study [39], where deviation between simulation and experiment (absorbed energy) results for a linear time-invariant controller (LiTe-Con) is dominant in small sea states, which is explained by low signal-to-noise ratios. Another study, investigating uncertainty in experimental tests can be found in [79], highlighting the essence of uncertainty due to measurement errors and filter (applied to the measured data) characteristics in PTO friction damping force and mooring line force measurements, although, precise quantification is not provided.

Consistent across all the noted studies is the implicit understanding that fidelity of the WEC models plays a crucial role in accurate performance evaluation, model validation, and control of WECs, but there is a paucity of evidence defining which uncertainty sources exert significant influence in PWT testing and their characteristics at different operating conditions, as well as the techniques that could be used to eliminate the artifacts from captured data toward obtaining accurate WEC model characteristics.

Within this context, the current study considers a PWT setup with a point absorber WEC, using chirp-type force-input experiments, which is a well-established signal type for system identification wave tank testing [29]. Representative linearised WEC models (referred as multi-linear WEC models in this study) are derived using chirp signals at different amplitude levels in PWT testing. Uncertainty and external noise are characterised at different operating points inherent to the experimental settings, within the two-step force transmission chain (see Section 4.4). A particular filtering technique, based on the Savitzky–Golay (SG) filter, which proved to be suitable to smooth noisy data, without introducing phase lag [119, 120, 121], is proposed in an innovative manner of a nonlinearly varying window length, in order to regulate the cut-off frequency of the filter in accordance with the linearly varying frequency of the chirp-type signals. This novel method successfully excludes high-frequency contamination from chirp-type signals (without introducing phase shift) and overcomes the disadvantages of previously proposed filtering methods for chirp-based signals [29]. One of the main contributions of this study is the

detection and removal of outliers occurring in load cell measurements and the proposal of appropriate autoregressive (AR) bi-directional model extrapolation to fill in the gaps in the recorded data, given the predominantly sinusoidal (chirp) nature of the excitation signals contaminated with external disturbance sources. Moreover, appropriate post-processing techniques (in the frequency-domain) are applied to preserve the physical characteristics of the WEC system and to extract useful information from the multi-linear WEC models obtained from PWT testing under study. Additionally, frequency-domain post-processing techniques are used to preserve the WEC system's physical characteristics and extract useful information from the multi-linear WEC models obtained from PWT testing. To point out the dominancy of contamination at different operating points, quantitative results are presented which should be considered in realistic WEC modelling. Finally, with a view to robust WEC control, a nominal model and uncertainty bound are quantified, emphasising the differences of the resulting nominal models before and after the application of pre- and post-processing techniques.

The layout of the remainder of this paper is as follows: Initially, dynamic characteristics of WECs, including modelling considerations and an overview of the parameters that may cause uncertainty in PWT tests are presented in Section 4.3. Next, in Section 4.4, the PWT setup and experiment design for the current study are presented. Section 4.5 details data pre-processing (in time-domain) and data post-processing (in frequency-domain) techniques deemed appropriate for the current experimental test. Section 4.6 covers all the steps toward the final empirical transfer function estimate (ETFE) calculation results and reports the qualitative and quantitative results. The potential application of the multi-linear models to a robust WEC control strategy is covered in Section 4.7 and, finally, overall conclusions from the study are drawn in Section 4.8.

4.3 WEC dynamic characteristics

Dynamic characteristics of WEC systems, including linear modelling fundamentals and properties, as well as the list of general contamination sources in experimental wave tank tests, are covered in this section.

4.3.1 Modelling considerations

The fluid-structure interactions experienced by a WEC system are typically modeled using potential flow theory, with the WEC referenced from its still water level (SWL) in an undisturbed wave field and immersed in an assumed infinite-depth sea.

The dynamics of WEC structures, under the assumption of linearity, i.e. small displacements, and linearised hydrodynamic coefficients (using linear potential theory) are commonly modelled using an integro-differential equation proposed by Cummins [87]:

$$(m + m_\infty)\ddot{y}(t) = f_{\mathsf{ex}}(t) - f_u(t) - k_{\mathsf{h}}y(t) - h_{\mathsf{r}} * \dot{y}(t) \tag{4.1}$$

The linear superposition of contributory forces of Cummins' equation comprises the inertial, radiation (with $h_{\mathsf{r}}(t)$ being the radiation impulse response function), hydrostatic (with k_{h} being the hydrostatic stiffness), and excitation ($f_{\mathsf{ex}}(t)$), produced by the action of incoming waves, forces. In Eq. (4.1), $m \in \mathbb{R}^+$ is the mass of the device and m_∞ is the added mass at infinite frequency. $y(t)$, $\dot{y}(t)$, and $\ddot{y}(t)$ are the device displacement, velocity, and acceleration, respectively.

The properties of (internal) stability and passivity are intrinsic characteristics of a physical WEC system [59]. The internal stability of Cummins equation is guaranteed if the parameters are properly defined based on the physical property of the WEC device [61]. Passivity, informally described as a characteristic of a system that cannot produce energy, arises from an intrinsic physical property of the system. Passivity in LTI systems is verified with a positive real transfer function for all frequencies [62, 59].

Linear WEC models can be interpreted in the frequency domain under the assumption of periodic motion. Considering the measurable finite set of input signals, generating a corresponding set of output signals (which can be heave motion, in this case), the WEC model can be characterised by following standard frequency-domain techniques, including the so-called empirical transfer function estimate (ETFE). By considering the mapping $f(t) \rightarrow y(t)$ ($(f(t), y(t))$ as the input-output pair, defined in the time-domain), the ETFE can be computed as:

$$H(j\omega) = \frac{Y(j\omega)}{F(j\omega)} \tag{4.2}$$

where $F(j\omega)$ and $Y(j\omega)$ are the Fourier transforms of $f(t)$ and $y(t)$, respectively.

4.3.2 Uncertainty and external disturbance sources in PWT tests

Considering the PWT experiments, we classify the uncertainty and external disturbance sources into three categories: Electromechanical effects, hydrodynamic effects, and structural effects.

4.3.2.1 Electromechanical effects

The fidelity of signals going through/controlled by electromechanical components is an important ingredient of the precision of the ETFE. To better identify the data contamination sources from the electromechanical part, it is important to consider each component and its characteristics. Some sources of uncertainty, external disturbance, or nonlinearity associated with electromechanical components are listed below:

- *Sensors*: Noise is ubiquitous in sensor readings (uncorrelated with variations in sensor input) that can degrade the useful information of the data. The signal-to-noise ratio (SNR) is a metric used to compare the level of the true signal component to the level of the noise embedded in the signal. The SNR for time domain signals can be obtained by the ratio of the root mean square (RMS) of the signal to the RMS of the (unwanted) noise. In terms of dB, the SNR is computed as

$$\mathrm{SNR} = 20\log(\mathrm{RMS}_{\mathrm{signal}}/\mathrm{RMS}_{\mathrm{noise}}) \tag{4.3}$$

  The saturation limits of the sensor should also be considered as a possible source of error, where the data exceeds the measurement limit of the sensor.

  An important source of data contamination (especially from load cell readings) are *outliers* or *impulse spikes* which can be caused by random events, including movement of the frame that holds the sensor, possibly due to reflected waves in the load cell [122]. Outliers generally have an impulsive characteristic, rising sharply to a peak, with a more gradual decay, which is superimposed on the main signal.

- *Linear motor*: Two major nonlinear phenomena, force ripple and friction, associated with linear motors affect the precision of the motor output. Force ripples, arising from the structure of the motor (i.e. cogging forces associated with discrete magnet placement), and friction may introduce problems with position control and tracking error, respectively [123].

4.3.2.2 Hydrodynamic effects

In PWT tests, the initial test conditions [56], such as residual waves, or reflected waves from the side walls of the tank during the experiments, can cause contamination. Some physical properties of the water (e.g. viscosity), and nonlinearities arising from complex hydrodynamic interactions, including drag, flow separation, and vortex shedding [88], can contribute to hydrodynamic perturbation sources in PWT tests.

4.3.2.3 Structural effects

One of the major uncertainty sources in PWT testing arises from the positioning system or mooring system, depending on the WEC type. The mounting structure (gantry) may undergo vibration when the WEC experiences high input forces [124], resulting in additive artifacts to the measured signals. WEC systems with mooring lines have a high level of uncertainty, which includes difficulty with scaling the elastic and mass characteristics of prototype lines, the instrumentation (e.g. load cells) of the mooring line, the exact location of anchor points, as detailed by [33].

4.4 Physical wave tank (PWT) and WEC

In this article, the particular WEC under investigation is a Wavestar prototype system [57, 125], a well-established point absorber type WEC, consisting of a rotational arm connected to a hemispherical floater, described with the PTO system, mounting structure, motion sensors, load cell, and location of the centre of gravity of the device (C_g) in Fig. 4.1. The considered WEC prototype is a 1/20th scale model, with the properties and dimensions listed in Table 4.1, where the moment of inertia and centre of gravity are labeled as MoI and C_g, respectively.

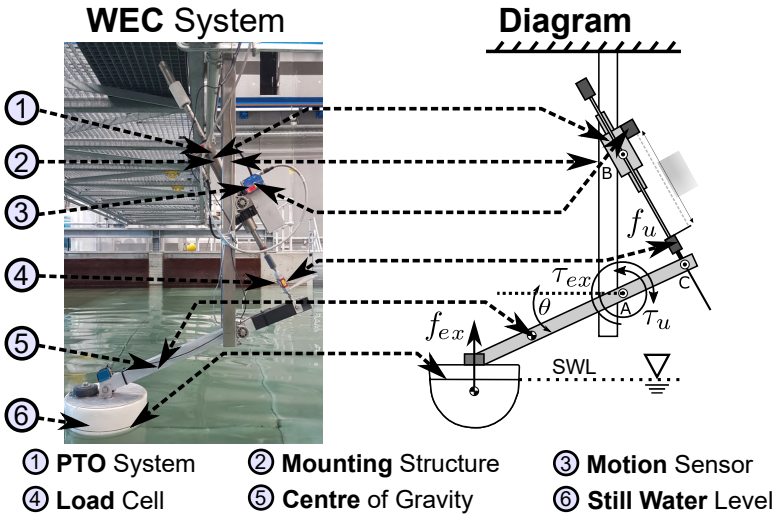

Figure 4.1: Components of the experimental WEC system (photograph of the WEC system on the left and schematic diagram on the right)

As shown in Fig. 4.1, the floater is connected to a fixed reference frame through two joints (joints A and B) and a mobile joint (joint C) with translational displacement indicated by x_m, while the rotational motion is indicated by the angle θ. The floater arm stands at approximately 30° with respect to the horizontal reference plane in its equilibrium position, indicated as SWL in Fig. 4.1. The WEC device is actuated with

Table 4.1: Model dimensions, relative to the still water level (SWL), and mass properties for the 1/20th scale Wavestar device.

Parameter	Value [Unit]
Float Mass	3.075 $[kg]$
Float MoI (at C_g)	0.001450 $[kg \cdot m^2]$
Float Draft	0.11 $[m]$
Float Diameter (at SWL)	0.256 $[m]$
Arm Mass	1.157 $[kg]$
Arm MoI (at C_g)	0.0606 $[kg \cdot m^2]$

a linear motor (equipped with a corresponding driver), acting as a PTO system, a force sensor, a position laser sensor, and an input/output data acquisition board, manufactured by National Instruments. The linear motor and driver are capable of producing a force of up to ± 200 N, which covers the purpose of this study. The force sensor is an S-beam Futek LSB302 300lb load cell, with an SGA analogue strain gauge amplifier, which provides a high-fidelity force measuring system. The position laser sensor used is a MicroEpsilon ILD-1402-600, also a high-performance system. The position of the PTO system is measured with a (motion) laser sensor (labeled as 3 in Fig- 4.1). It must be noted that, although the linear position of the PTO system is measured, the angular position, as considered in the model as the output, can be easily derived using basic trigonometric relationships.

The experimental data in this study is acquired during physical wave tank tests in the wave basin at Aalborg University, Denmark. The tank measurements are 13 m in length and 8.4 m in width, with a water depth of 0.9 m. The wave tank is schematically depicted in Fig. 4.3, including its main dimensions and components.

The prototype device is mounted on a supporting structure, in the form of a bridge for commissioning and operation, spanning the full width of the tank. The bridge can be seen in Fig. 4.1, located in the upper-left corner of the picture. The wave tank has a wave absorption system to reduce wave reflections, while a wave maker, generally used to generate waves, is also utilised to actively absorb waves and reduce reflections.

To better identify the nonlinearity, uncertainty, and external noise/disturbance sources contaminating the data in the experimental setup under study, the two-stage force transmission chain (indicated with different shadowed areas), as illustrated in Fig. 4.2, is considered. The perturbation signal d_f, represents all the forces considered, for the purpose of the first stage of the chain, as exogenous.

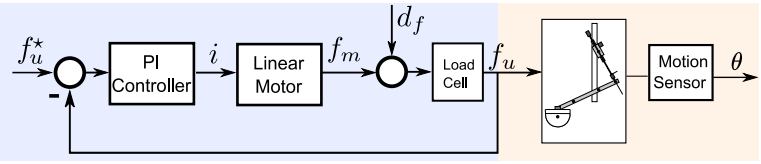

Figure 4.2: Two-stage chain: $f_u^\star \rightarrow f_u$ mapping (stage 1: blue shadowed area) and $f_u \rightarrow \theta$ mapping (stage 2: orange shadowed area)

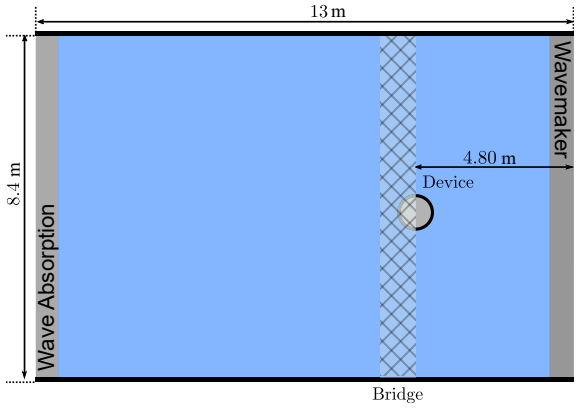

Figure 4.3: Schematic of the experimental wave tank for identification tests

1. *Reference force-to-actual force mapping*: This stage includes the proportional-integral-based (PI-based) controller to track a force set point, a linear motor containing its own internal controller for the current tracking loop (having the current, i, as the input, and motor force, f_m, as the output) which acts as the PTO system in this study, and load cell (as illustrated in Fig. 4.2). Any contamination from the electromechanical components influences this part of the transmission chain.

2. *Actual force-to-motion mapping*: This step is the process of generating WEC motion from the applied actual force (f_u) (Fig. 4.2)), which contains uncertainty sources associated with hydrodynamic and structural parts.

4.4.1 Excitation signals

In the PWT setup under study, the buoy is excited using force inputs (through the PTO system), in the absence of any incoming waves. Chirp-based signals are of particular interest for performing identification tests in the wave tank to characterise the dynamical behaviour of the system, since the complete frequency range of interest can be covered (reducing the number of required experiments compared to single-frequency sinusoidal signals). A linear frequency-modulated chirp signal has the instantaneous frequency $f(t)$ changing with time, as $f(t) = ct + f_0$ (f_0 is the initial

frequency and c, the chirp rate), measured in Hz. The corresponding time-domain function for a sinusoidal linear chirp can be formulated as [126]:

$$x(t) = A\sin\left(\phi_0 + 2\pi\left(\frac{c}{2}t^2 + f_0 t\right)\right), \quad \text{for } t \geq 0, \tag{4.4}$$

with amplitude A, and initial phase ϕ_0. The chirp rate (constant for linear chirp signal) can be obtained by taking the first derivative of $f(t)$.

4.5 Data processing

In this study, data pre-processing and post-processing refer to signal-processing techniques applied before and after ETFE calculation, respectively, with an aim to get authentic ETFEs and extract useful information. The pre- and post-processing framework is shown in Fig. 4.4, and detailed in the following:

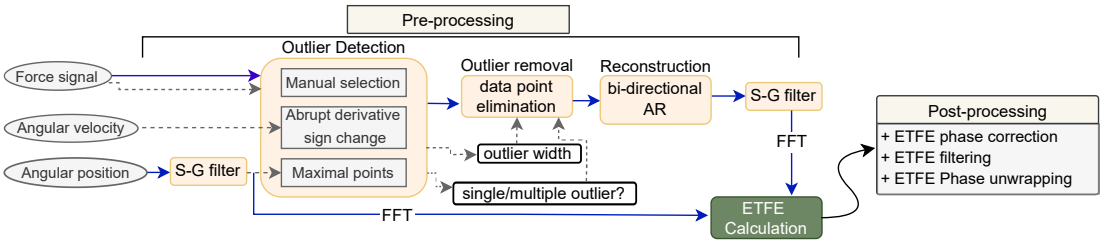

Figure 4.4: Framework for pre and post-processing steps.

4.5.1 Data pre-processing

Data pre-processing in this study involves signal-processing techniques applied to time-domain data (before ETFE calculation). This helps to extract useful information from signals often contaminated with external disturbance. Considering the nature of the contamination typically being of high-frequency content, we propose a low-pass filtering approach to recover the signal. Despite availability of various frequency-domain filtering techniques, filtering chirp-type signals (considered in this study) is challenging, due to their time-varying frequency nature. As an example, the difficulty associated with the correct initialisation of the filter, resulting in unwanted transient behavior effects introduced by the implementation of a moving band-pass filter to chirp-type experiments, has been articulated in [29]. The filtering method proposed in this study excludes the high-frequency components, without introducing phase shift. Moreover, due to force data contamination by outliers, introduced by the load cell, the methodology for the detection and removal of outliers is presented as follows:

4.5.1.1 Savitzky–Golay (S-G) filter

S-G filter [81], widely used in signal processing applications for data smoothing, is a shift-invariant, finite-impulse-response low-pass filter, based on a local polynomial regression to a set of input samples in a least-square sense, with each point of the signal replaced by the value of the polynomial at that point. Given a discrete signal for a group of 2M + 1 samples, $\{y[n]\}_{n=-M}^{M}$, (M points to the left and M points to the right of a given data point), the polynomial can be computed as:

$$p(x) = \sum_{k=0}^{N} a_k x^k, \tag{4.5}$$

where N is the polynomial order, and the polynomial coefficients (a_k) are computed such that the mean-squared approximation error,

$$\epsilon_N = \sum_{n=-M}^{M} \left(\sum_{k=0}^{N} a_k x[n]^k - y[n] \right)^2, \tag{4.6}$$

is minimised (frame length is $2M + 1$).

The frequency-domain characteristics of the SG are detailed by [82, 127], where a reasonably acceptable approximation for the 3 dB cut-off frequency of the SG filter in terms of the indicated range of frame length and polynomial order can be calculated as:

$$f_c = \frac{N+1}{3.2M - 4.6}, \qquad M \geq 25 \; and \; N < M. \tag{4.7}$$

where f_c is the normalised cut-off frequency.

Considering the particular application of the S-G filter to a linear chirp signal, various parametric designs can be considered:

1. **Standard S-G filter**: A standard S-G filter, with a fixed window length and order, has a unique cut-off frequency. For application of a standard SG filter to a chirp-type signal, a specific parameter selection should be considered to design a filter with a cut-off frequency above the frequency range of the signal. A disadvantage of using a standard S-G filter for a chirp signal is the inability to properly filter the high-frequency components, as the instantaneous frequency of the signal changes.

2. **Moving SG filter**: A moving SG filter can be considered with a fixed order but varying window length (and cut-off frequency) filter. For the linear chirp-type signal, the following moving S-G filter designs are analysed:

(a) **Fixed order and linearly varying cut-off frequency**: For a fixed-order filter, the varying window length can be obtained by tuning the cut-off frequency of the filter based on the instantaneous frequency of the chirp signal. Considering the cut-off frequency of the filter (in the frequency domain) corresponds to the point at which the filter attenuation reaches -3 dB relative to its maximum amplitude response, the cut-off frequency of the filter should be selected at a value higher than the maximum signal frequency to ensure adequate signal preservation. This method of SG filter parameter design may result in a window length requirement exceeding the number of signal samples.

(b) **Fixed order and *linearly* varying window length**: A varying filter can be designed by linearly changing the window length, considering the first and last zero-crossing points, and fitting the SG polynomial based on the number of chirp periods. A disadvantage of this design option lies in the fact that there is an increasing number of oscillations of the chirp signal in a linearly varying window, introducing difficulty by considering a fixed filter order.

(c) **Fixed order and *nonlinearly* varying window length**: Considering the nonlinear variation of the successive zero crossing distances of a linear chirp signal in the time domain, an appropriate design for the SG filter could be a selection of a nonlinearly varying window length, based on the zero crossing distance variations and selection of a proper fixed order (N in Eq. (4.5)) for polynomial fitting. The appropriate set of SG parameters can be calculated by analysis of the convergence of the cut-off frequency of the moving filter and the instantaneous frequency of the chirp signal.

4.5.1.2 Outlier removal

Measurement force records from load cells frequently contain *outliers* which degrade the meaningful information of the data. It is important to examine the influence of outliers, the level of contamination on the data, and problems associated with missing data due to outlier occurrence and, if required, detect the outliers and apply appropriate data-cleaning approaches. Some details regarding the procedure of outlier detection and removal and data reconstruction are presented in the following:

1. **Outlier detection**: The outlier characteristics (mentioned in Section 4.3.2.1) generally allow visual inspection for their detection. Nevertheless, manual selection of outliers is not always possible or effective. Some widely used techniques for

outlier detection are based on statistics, such as standard deviation around the mean (when the standardised residual exceeds a specific threshold value [83]) and median absolute deviation [84]; however, these statistics can be ineffective in the presence of a high level of data contamination. Moreover, outlier detection techniques may fail in the presence of multiple outliers. Outliers can also have a connection with the physical behaviour of the test setup components, for example in [122], where the occurrence of outliers from recorded force data from a load cell coincides with the motion of the beam attached to the load cell (possibly caused by reflected waves in the load cell and/or relaxation of the strain gauges).

2. **Outlier removal**: After the detection of the nature of the outlier (single/multiple) and the exact location of the outlier peak, data points can be removed. Due to the diverse characteristics of the outliers (variable number of samples), and their shape (e.g. asymmetric with respect to the peak), special care should be taken in the proper identification of the outlier time range.

3. **Reconstructing the missing points of the signal**: The treatment of missing data due to outlier removal can be handled using different principles. Static interpolation methods, e.g. linear, nearest neighbor, and splines have been extensively studied and shown to be effective in missing data reconstruction for the case of oversampled signals [85]. However, their accuracy may be acceptable for slowly varying low-frequency signals [128], and pose problems to reconstructing missing points of a signal with larger gaps, contamination, or rapid frequency variation. Identification of missing data for heavily disturbed data, or a signal with low oversampling, has been addressed by [129], which increases the complexity of dealing with missing data. Concatenating the data records where different experiments on the same plant exist, is another way to estimate the missing data points studied by [130]. The most efficient methods to reconstruct the data gaps are model-based, where some prior information on the characteristics of the signal is used to reconstruct the data. In this study, an estimation method, based on local autoregressive (AR) modelling which is an appropriate choice for many locally stationary signals and deals with both noise-like and harmonic signals is utilised [86].

   - *Bi-directional autoregressive model*: This technique replaces the gaps in a signal by estimates extrapolated from a local autoregressive (AR) model

$$x[n] = \sum_{k=1}^{q} a_k x[n-k] + a_0 + \epsilon[n], \tag{4.8}$$

using the average of forward and backward prediction (available data points on both sides of the missing data). In Eq. (4.8), $x[n]$ is the predicted signal sample based on previous signal samples, and a_k are the parameters of the autoregressive model of order q. $\epsilon[n]$ is white noise. A widely used criterion for order selection of autoregressive models is Akaike information criterion (AIC) [131], where the order resulting in a minimal final prediction error is selected, considering a prescribed sufficiently wide range of possible orders.

4.5.2 Data post-processing

Data post-processing which, in this study, refers to signal-processing techniques applied to ETFE computation, is applied with the aim of enforcing the physical characteristics of the WEC system. The post-processing techniques utlised are described as follows:

- **ETFE phase correction**: Passivity, a physical feature of the system must be always satisfied (Section 4.3.1). A possible post-processing method to enforce passivity can be applied by restricting the phase of the ETFE (in this study motion-to-force mapping) to $[-180\ 0]^\circ$ for all frequencies.

- **ETFE filtering**: The moving average method is a widely used statistical filter in the time domain (equivalent to a low-pass filter in the frequency domain), which is based on the calculation of the average of a specified number of adjacent time domain data points in a sequence. An appropriate window size should be selected for moving the average filter to achieve a balance between artifact reduction and signal preservation.

- **Phase unwrapping of the ETFE**: Phase wrapping is defined as phase jumps (modulo 2π), between consecutive frequency bins in the phase of the ETFE which arise from specific software implementation of the fast Fourier transform calculation, or from significant levels of noise or distortion present in the signal. A post-processing technique to deal with phase wrapping can be applied to remove phase jumps, improving visualisation, by adding/subtracting 2π to the phase calculation, at appropriate points.

4.6 ETFE calculation results

This section provides all the pre- and post-processing steps (Fig. 4.4), specific to the PWT setup, to the final ETFE calculation, along with qualitative and quantitative results. Considering the diagram in Fig. 4.2, the available time-domain data are the reference force ($f_u^\star$), measured force (f_u), measured angular motion (θ), and angular velocity ($\dot{\theta}$). The time-domain experiments are performed over the interval $[0\ 140]$ s using linear up-chirp (Eq. (4.4)) input forces, in a frequency range of $[0.06\ 75.3]$ rad/s (chirp rate of 0.0856), and amplitude set $A_i = \{2.5, 5.0, 7.5, 10.0, 12.5, 15.0, 17.5, 20.0\}$ N (Newton) covering the complete dynamical characterisation of the WEC system.

4.6.1 Example qualitative results

Considering the two-stage mapping according to Fig. 4.2, the mapping $f_u^\star(t) \rightarrow f_u(t)$ (defined as H_1), and the mapping $f_u(t) \rightarrow \theta(t)$ (defined by H_2), are calculated using Eq. (4.9) as follows:

$$H_1(j\omega) = \frac{F_u(j\omega)}{F_u^\star(j\omega)}, \quad H_2(j\omega) = \frac{\Theta(j\omega)}{F_u(j\omega)}, \tag{4.9}$$

where $F_u^\star(j\omega)$, $F_u(j\omega)$, and $\Theta(j\omega)$ represent the Fourier transforms of $f_u^\star(t)$, $f_u(t)$, and $\theta(t)$, respectively. Prior to ETFE calculation in Eq. (4.9), pre-processing steps are considered.

4.6.1.1 Data pre-processing

1. **Outlier removal**: Analysing the time-domain data, outliers are detected to occur (in f_u) at time instances of the maximal points of θ, and abrupt derivative changes between the maximal points of $\dot{\theta}$. This correlation is detailed in Fig. 4.5, showing two time portions of $\dot{\theta}$, f_u, and θ corresponding to the data at $max(f_u^\star) = 2.5$ N. The yellow highlights show the window where the outliers occur. In particular cases, multiple outliers occur, as in the case of a triple outlier in the force signal at $max(f_u^\star) = 20$ N, as presented in Fig. 4.6, as well as the highlighted time portions in the $\dot{\theta}$ and θ plots. It is observed that there is a correlation between triple outlier occurrence and continuous abrupt derivative sign changes in $\dot{\theta}$ and saturated behaviour of θ.

   After detection of the exact location of outlier peaks using manual selection, abrupt derivative changes in $\dot{\theta}$, and maximal points of θ, the outlier type (single/multiple) is determined and, by calculating the width of the outlier range, the appropriate data points can be removed.

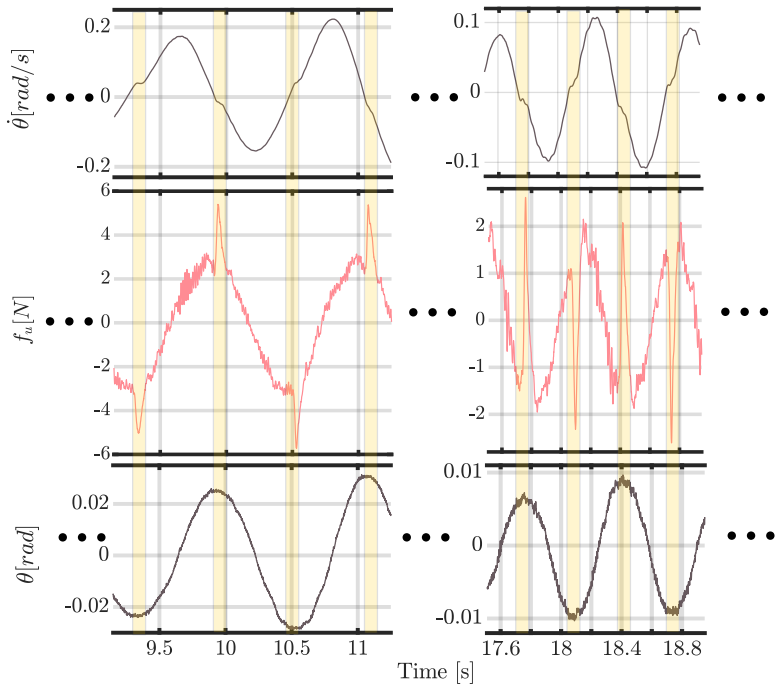

Figure 4.5: Outlier occurrence (middle plots) correlation with abrupt derivative changes between the maximal points of $\dot{\theta}$ (upper plots), and maximal points of θ (lower plots). ($max(f_u^\star) = 2.5$ N)

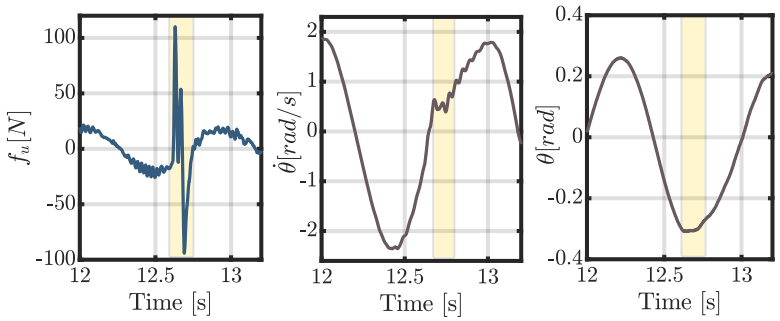

Figure 4.6: Multiple outlier occurrence at $max(f_u^\star) = 20$ N and its correlation with continuous abrupt derivative sign changes of $\dot{\theta}$ and saturated behaviour of θ

After outlier removal, the missing data points of the signal are reconstructed. System identification techniques, due to complexity, and data records concatenating, due to the limitation of having single test records for each case (detailed in Sec. 4.5.1.2 (item 3)), are not considered in this study. In Fig. 4.7, the measured force signal (at $max(f_u^\star) = 2.5$ N), as well as three methods (two interpolation methods, and model-based bi-directional AR) for data reconstruction, are shown. Considering the noisy nature of the signal, and the large number of missing points, a basic *linear interpolation* method fails to appropriately reconstruct the data. In particular, if the gap occurs around maximal points, linear interpolation can lead to underestimation of the amplitude of the original signal. *Piecewise*

Cubic Hermite Interpolating Polynomial (PCHIP) [129], is another method that can be used; however, as it can be seen in Fig. 4.7, in the case of the noisy signal, they fail to properly reconstruct the gaps, and even the estimated curvature sign can be incorrect (right hand zoomed section). The yellow line, representing the PCHIP interpolation, overlaps with the red line, which corresponds to the linear interpolation, in the zoomed-in plot on the left in Fig. 4.7. Finally, the bi-directional AR method, which has been shown to be powerful in reconstructing large gaps, frequency-varying signals, and noisy signals, is utilised showing proper data reconstruction method for the gaps of the signals in the current study. For the bi-directional AR reconstruction, a maximum frame length of 20 sample points, and an order based on minimising AIC have been utilised.

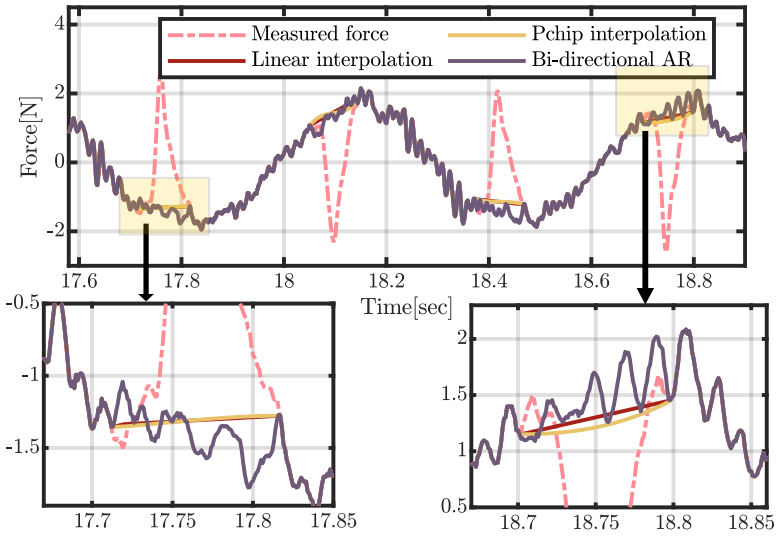

Figure 4.7: Comparison of three methods (linear interpolation, PCHIP, and bi-directional AR) for reconstructing gaps in the data.

2. **SG filtering**: SG filter is utilised as a pre-processing technique, with a nonlinearly varying window length and fixed order (Sec. 4.5.1.1.2(c)), considering the characteristics of the chirp signal (Sec: 4.6). In order to determine appropriate parameters for the SG filter, different combinations of the window length and order are considered, and the resulting cut-off frequency vectors (f_cs) are presented in Fig. 4.8, as well as the instantaneous frequency of the chirp signal, with characteristics given in Section 4.6, as a reference. Considering Eq. (4.7), decreasing the order, or increasing the window length, will decrease f_c. Accordingly, to decrease f_c (to the frequency of the chirp signal), different choices of the window length (considering the number of zero crossing (Z_n)), and the smallest order (N) to fit the polynomial based on the number of cycles in the window length, are considered. Based on the results shown in Fig.

4.8, increasing Z_n, and keeping the order as small as possible, noticeably decreases f_c. However, by further increasing Z_n (> 8), f_c cannot decrease further. This occurs since the interval between zero crossings varies nonlinearly, and increasing Z_n (and consequently increasing the order to fit the polynomial order) does not have a significant effect on f_c.

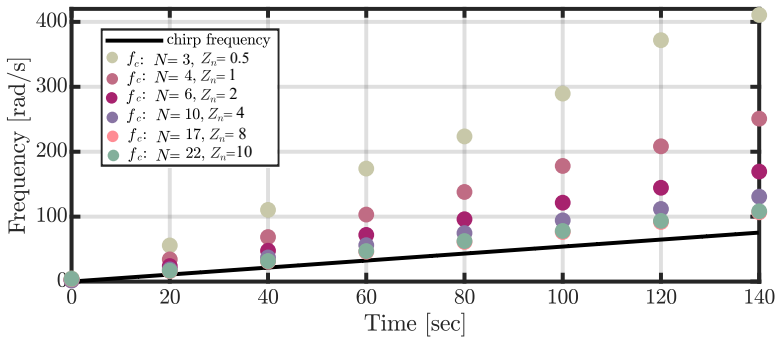

Figure 4.8: SG filter cut-off frequency analysis for different combinations of order (N) and window length (based on the number of zero crossing (Z_n)) for a linear chirp signal. The solid black line shows the instantaneous frequency of the chirp signal with characteristics given in Sec. 4.6

For a more detailed analysis of the SG filter parameters, different combinations of N and Z_n are considered at the instantaneous frequency of the chirp signal, at $t = 70$ s ($f = 37.7$ rad/s) in a 3D plot in Fig. 4.9. The blue dot in Fig. 4.9, which corresponds to an f_c for $N = 17$ and $Z_n = 8$, shows proximity to the instantaneous frequency of the chirp (shown with the flat black plane), which also confirms the results presented in Fig. 4.8. Considering that f_c is obtained from the -3 dB attenuation point of the frequency response of the filter, an exact frequency match is not ideal and f_c should have a higher value than the signal frequency.

Based on parameters $N = 17$, and $Z_n = 8$, Fig. 4.10 shows the resulted f_c of the SG filter, as well as the instantaneous frequency of the chirp signal (with units on the left vertical axis). Moreover, the window length variations (independant variable) based on the number of samples for the design parameter of $Z_n = 8$, are shown with units on the right vertical axis.

In this study, moving window SG filtering is applied to both f_u and θ at all input amplitude levels. For f_u signals, outlier removal (4.6.1.1 (item 1)) is applied prior to SG filtering; note the dramatic effect in Fig. 4.11 at force level of $max(f_u^\star) = 2.5$ N. In the time interval $[0\ 40]$ s, the pink solid line is the measured force signal (f_u), the SG filtered force (f_u^{SG}) is shown with a pink dashed line, while the force with outliers removed (f_u^{RO}) and the SG filtered force with outliers removed ($f_u^{SG,RO}$) are shown using solid and dashed grey lines, respectively. Comparing f_u and

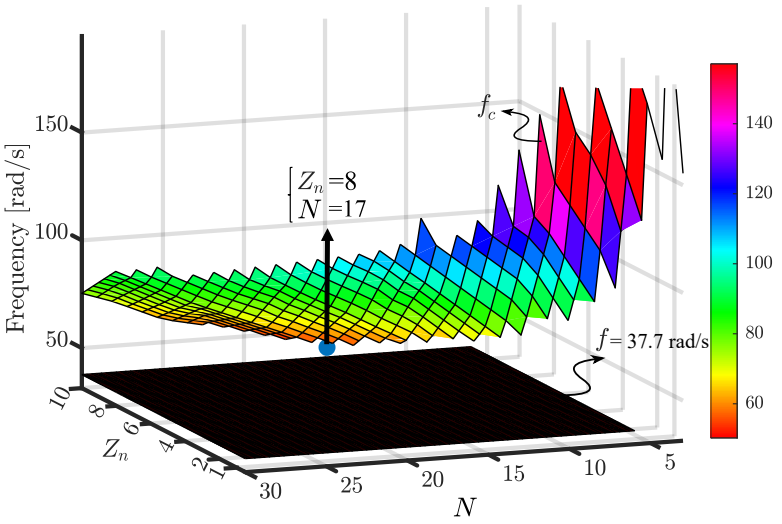

Figure 4.9: SG filter cut-off frequency analysis for different combinations of N and Z_n at an instantaneous frequency of 37.7 rad/s (2D black plane), for a chirp signal with characteristics given in Sec. 4.6)

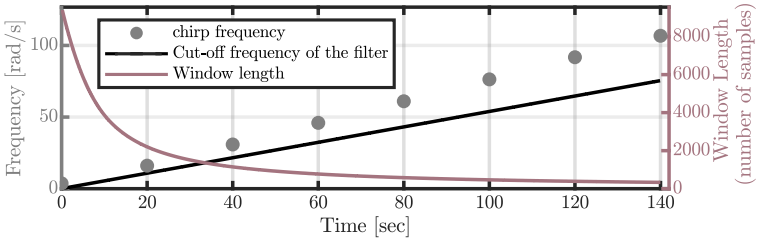

Figure 4.10: Window length variation of the moving SG filter (units shown on the right horizontal axis), and the resulting cut-off frequency of the filter compared with the instantaneous frequency of the chirp signal (units shown on the left horizontal axis).

f_u^{SG} in Fig. 4.11, it can be seen that SG filtering (f_u^{SG}) removes high-frequency components (e.g. noise); however, due to distortion caused by outliers, the amplitude of f_u^{SG} can be overestimated (e.g. see the zoomed part (a) when outliers occur at the peaks of the signal and share the same polarity, upward at maxima and downward at minima), the phase of f_u^{SG} can be shifted (e.g. the zoomed part (b) when outliers occur between the peaks of the signal), or the amplitude of f_u^{SG} can be underestimated (e.g. the zoomed part (c) when outliers occur at the peaks of the signal with opposite polarity, upward at minima and downward at maxima). Comparing f_u^{SG} and $f_u^{SG,RO}$ emphasises the importance of outlier removal before SG filtering to preserve the amplitude and phase of the original signal (f_u).

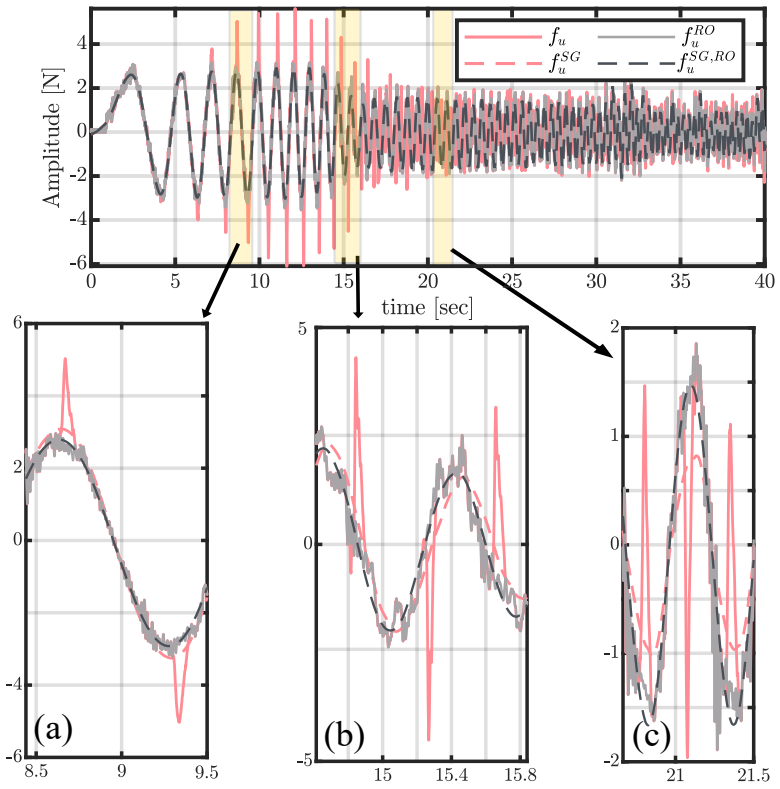

Figure 4.11: Pre-processing in the time domain at $max(f_u^\star) = 2.5$) N. Comparison of f_u, f_u^{RO}, f_u^{SG}, and $f_u^{SG,RO}$.

4.6.1.2 Data post-processing

Data post-processing refers to the signal processing techniques employed after ETFE calculation, including ETFE phase correction employed by forcing the phase limit to the range of $[-180\ 0]^\circ$, phase unwrapping, and frequency-domain ETFE filtering (using a moving average filter with six adjacent data points) as detailed in Sec. 4.5.2 (an example of the effects of the post-processing techniques on ETFE phase will be shown later (Fig. 4.18)).

4.6.1.3 Final ETFE results

The final ETFE results for the two-stage chain (Fig. 4.2), after applying pre- and post-processing techniques, are presented in this section. In Fig. 4.12, the first stage of the chain (force-to-force) mapping using $f_u^\star$ and $f_u^{SG,RO}$, for all input amplitude levels, is shown. From the magnitude plot, it can be concluded that the actual force fails to track the amplitude of the reference force at all input levels, showing more amplitude drop, and variation, as the input amplitude level decreases. Moreover, the phase plot shows the failure of the actual force to track the phase of the reference signal, with larger phase shifts at lower input amplitude levels.

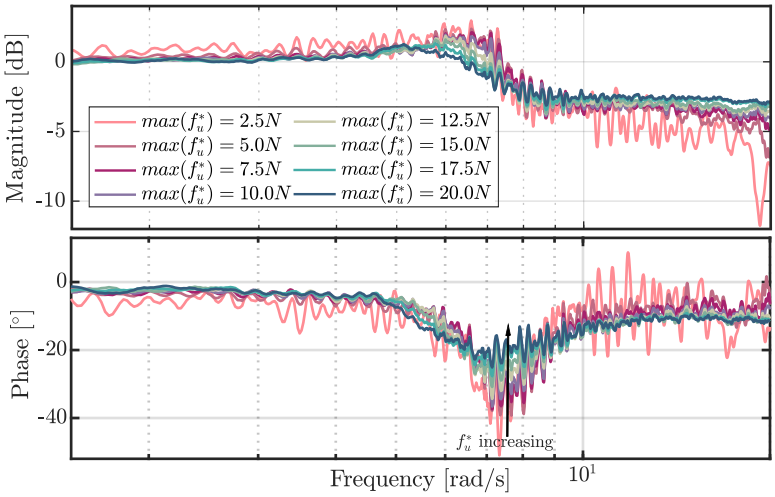

Figure 4.12: $f_u^\star$-to-$f_u^{SG,RO}$ mapping at all input amplitude forces after data pre- and post-processing.

In Fig. 4.13, the second stage chain (motion-to-force) mapping, using $f_u^{SG,RO}$ and θ^{SG}, at all input amplitude levels is shown. Due to the nonlinearity of the WEC system, different input amplitude levels result in different ETFEs. The major ETFE characteristics in this study are consistent with those analysed in a NWT setup using the same experiment type (force input amplitudes) in [68], most noticeably, increasing trend of the bandwidth, and a decreasing trend of the resonance frequency, as the amplitude of the input signal increases. The resonance frequency, corresponding to each amplitude level, is obtained by the peak point in the magnitude plot, or the phase plot where it crosses $-90°$. The ETFEs shown in Fig. 4.13, can be well-approximated (for instance using FOAMM toolbox [67]) using a 6^{th} order parametric model, and matching the frequency points at low- and high asymptotes, and resonance frequency [68].

4.6.2 Quantitative overall results

This section provides a quantitative measure of the noise, outliers, reflections, and structural vibration contaminating the data at different levels of input amplitude.

4.6.2.1 Noise quantification

To provide a quantitative measure of the noise corresponding to each output signal (θ), the SNR (Eq. (4.3)) is calculated as the ratio of the normalised RMS (NRMS) of the signal to the NRMS of the noise (NRMS=RMS/number of samples). Since it is difficult to separate noise from the signal, the portion of the signal in the time interval of $[60\ 140]$ s from the experiment at $max(f_u) = 2.5$ N, which includes the poorest

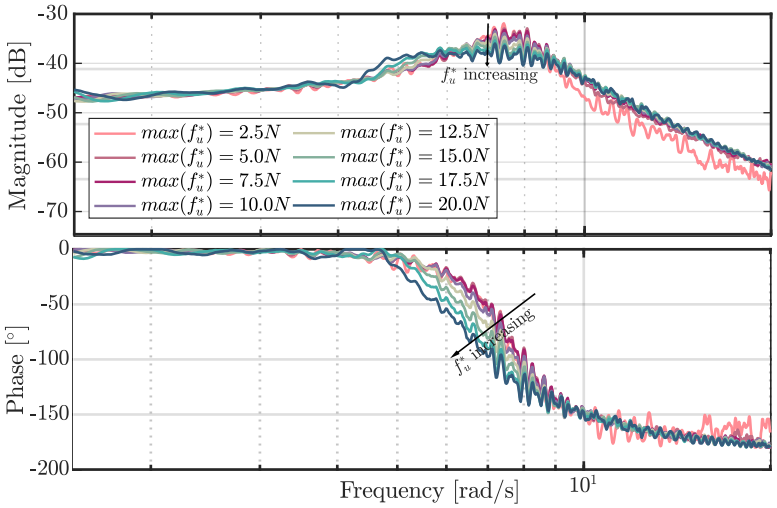

Figure 4.13: ETFEs at all input amplitude forces after data pre- and post-processing.

SNR, is considered for the calculation of the NRMS of the noise at all experiments. During this portion of the signal, the buoy motion is virtually still, since the frequency of the excitation signal is far from the resonance frequency of the buoy, and the amplitude of the excitation signal is small. Moreover, the artifacts, possibly from reflection and structural vibration are minimal at the smallest input amplitude level, and the data mostly corresponds to sensor measurement noise. The SNR, for all input force levels, in dB is shown in Fig. 4.15 (light gray color), showing a poor SNR at small input levels, and having a generally increasing trend with increasing input amplitude levels; however, it can be seen that there is a certain threshold at $max(f_u) = 12.5$ N beyond which SNR cannot be effectively improved.

4.6.2.2 Outlier quantification

Several methods can be used to provide a quantitative measure of the outlier amplitude/power, compared to the signal amplitude/power, to determine their level of contamination :

- **Outlier removal quantification**: The ratio of the power of the signal with outliers (f_u) to the power of the signal without outliers (f_u^{RO}) is a potential metric used to quantify the effect of outlier removal. However, this method is not ideal, since outliers can both increase and decrease signal power, depending on their location. (A positive outlier can occur both at maxima (contribute to an increase in the power), or minima (contribute to a decrease in the power.)

- **Peak-to-peak ratio (PPR)**: PPR is the ratio of the NRMS of the peaks of $f_u - f_u^{RO}$ (signal with outliers minus the signal without outliers) to the NRMS of the peaks

of the SG filtered signal (f_u^{SG}), and is a potential metric to quantify the effect of outliers. A block diagram, explaining the steps for PPR calculation, is shown in Fig. 4.14.

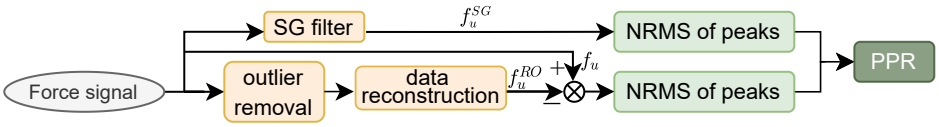

Figure 4.14: Block diagram for PPR calculation steps.

PPR, provides a useful metric to quantify the effects due to outliers, as has been shown earlier in Fig. 4.5, where the amplitude of f_u^{SG} can be overestimated/underestimated when large excursions in signal amplitude occur due to outliers. Moreover, considering the amplitude deviation of the signal due to outliers provides more sensible quantification results than considering their additive power and, since the outliers occur over a very short time interval, their power is much less compared to the power of the signal and fails to provide a good understanding of their quantitative impact. PPR results, for different input amplitude levels, are shown in Fig. 4.15 (dark grey color). It can be seen that there is a general increasing trend of PPR as the input amplitude level increases. However, at the highest input amplitude level ($max(f_u^\star) = 20$ N), the PPR level is very low (high level of contamination by outliers), which is due to multiple and large outliers shown in Fig. 4.6.

4.6.2.3 Reflection and structural vibration quantification

In the experiments, sinusoidal oscillations are present at time intervals when the frequency of the input force is much higher than the resonance frequency of the device, and no response in the output is expected. The oscillations, with frequencies of approximately 6.5 and 73 rad/s, with more noticeable magnitude at ($max(f_u^\star) = 20$ N), are most probably due to reflection (close to the resonance frequency of the device), and vibration of the mounting structure, respectively [124]. Such effects can be quantified, based on knowledge of their frequency contents. To this end, the portion of the time domain output signals in the interval of $[80\ 140]$ s, where the frequency of the excitation force is beyond the dynamical range of the device (the buoy movement is due to perturbations), is considered for all the experiments. A spectral domain analysis of this portion of the time signals shows considerable power at the peaks of the reflected waves (close to the resonance frequency of the device (6.28 rad/s)), and resonance frequency of the mounting structure (at 73 rad/s) [124]. In order to quantify the power corresponding to reflection and structural vibration, (two separate) band-pass filtering, with the centre frequencies equal to the

reflection and resonance frequency of the mounting structure, is applied. In order to provide quantitative results corresponding to the effects of reflection and structural vibration, transformation from the frequency domain to the time domain is applied to isolate the reflections, and structural vibrations, and the NRMS is calculated in Fig. 4.15, (light and dark purple color, respectively), with the units shown on the right vertical axis. The results show an increasing trend of the reflection and structural vibration NRMS, as the amplitude of the input force increases.

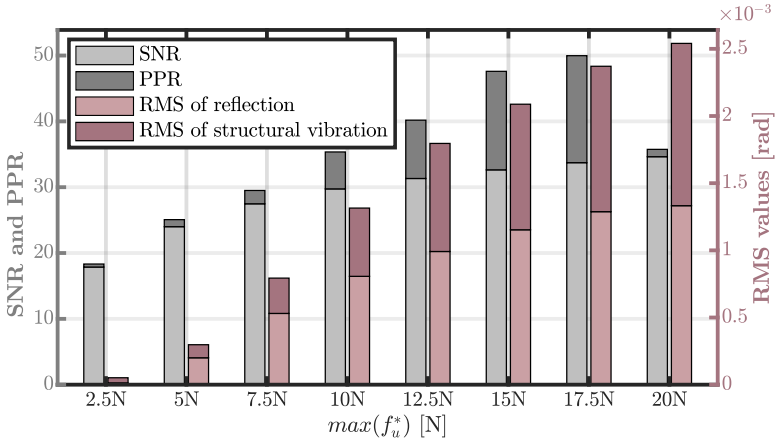

Figure 4.15: Quantitative results: SNR (dB) and PPR with the amplitudes shown on the left vertical axis (high values are desirable), and RMS of the reflection and structural vibration with the units shown on the right vertical axis (low levels are desirable).

To sum up the quantitative results for different operating points (Fig. 4.15), SNR and PPR are generally dominant at small input amplitude levels, with the contamination due to noise and outliers are mitigated in the pre-processed data. Note (in Fig. 4.15) the increasing trend in reflection RMS with increasing input amplitude level. Finally, data contamination from the structural components (Section 4.3.2.3), even though dominant at high input amplitude levels, contains high-frequency components (harmonics of 73 rad/s), which does not affect the operating frequency range of the WEC model.

4.6.2.4 Total distortion measures

In this section, the term *total distortion* is used in order to provide quantitative results which captures all distortion components including intrinsic nonlinearities and exogenous disturbance in the measured signals. Typically, total harmonic distortion is measured using sinusoidal signals, which contain energy at only a single spectral component (frequency), allowing any energy observed at other frequencies in the output to be attributed to nonlinearities or time-varying behaviours in the system. However, chirp signals, which distribute energy across multiple frequencies, have

been considered, which complicates the task of distinguishing distortion components from the input signal. Additionally, the experimental setting resulted in signals highly contaminated with noise and exogenous dynamic behaviours uncorrelated with the input signals, making the task even more challenging. Therefore, the term *total distortion* has been adopted to measure the power of unwanted signal components in relation to the fundamental signal's power, in analogy to the approach used for calculating total harmonic distortion plus noise (THD+N), a well-defined metric used for sinusoidal signals [132]. More specifically, for the measured force signals, total distortion is calculated as the ratio of the RMS value of the distortion ($f_u^{SG,RO} - f_u$) to the RMS of the fundamental (f_u) signal. Despite its drawbacks (distributed spectral content, varying frequency, exogenous factors, etc.), as previously discussed, total distortion analysis is presented here for the sake of completeness, offering a comprehensive overview from all perspectives. The results of the percentage total distortion for quantification of the distortion components in the measured force signal are presented in Table 4.2. Based on the results, the total distortion has a decreasing trend by increasing the input amplitude level, with a discontinuity occurring at the input amplitude level of 20N, most possibly due to a large distortion from outliers as per the results of PPR presented in Fig. 4.15.

Table 4.2: The total distortion of the actual signal at different levels of input amplitudes.

Input amplitude level	2.5N	5N	7.5N	10N	12.5N	15N	17.5N	20N
Total distortion	43.5%	27.0%	19.0%	15.1%	13.1%	12.1%	11.5%	31.5%

4.6.3 ETFE Comparisons

In order to highlight the effects of the different pre- and post-processing techniques, and their consequences on the results, some ETFE comparisons are provided in this section.

To analyse the effect of pre-processing (including outlier removal and SG filtering) techniques on the ETFE, the case of $max(f_u^\star) = 2.5$ N is highlighted, where the levels of noise and outliers are very dominant. In Fig. 4.16, three ETFEs, including ($f_u \rightarrow \theta$), ($f_u^{SG} \rightarrow \theta^{SG}$), and ($f_u^{SG,RO} \rightarrow \theta^{SG}$) are shown. Comparing the $f_u \rightarrow \theta$ (measured input to measured output) mapping with $f_u^{SG} \rightarrow \theta^{SG}$ (SG filtered input to SG filtered output), the advantage of applying an SG filter can be seen by the decrease in ETFE of magnitude and phase variance, while retaining the original

signal phase contents. The comparison of $f_u^{SG,RO} \rightarrow \theta^{SG}$ (where the outliers are removed prior to SG filtering) with $f_u^{SG} \rightarrow \theta^{SG}$ highlights the deleterious effect of outliers both on magnitude and phase of the ETFE.

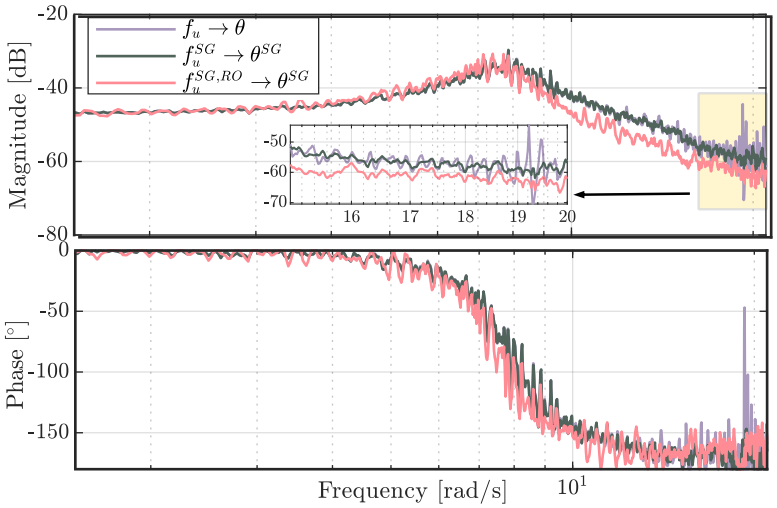

Figure 4.16: ETFEs comparison using measured input and output (f_u and θ), SG filtered input and SG filtered output (f_u^{SG} and θ^{SG}), and SG filtered removed outliers input and SG filtered output ($f_u^{SG,RO}$ and θ^{SG}) at $max(f_u^{\star}) = 2.5$ N.

Another example to highlight the beneficial pre-processing effect on ETFEs is shown in Fig. 4.17, where the mappings of $f_u^{\star} \rightarrow f_u$ and $f_u^{\star} \rightarrow f_u^{SG,RO}$, at $max(f_u^{\star}) = 20$ N, are compared, showing considerable reduction in variance of the mappings following pre-processing, which includes removal of dominant contamination by triple outlier occurrence. Pre-processing helps both to extract useful information (in Fig. 4.17, magnitude at high frequencies) and reduce the uncertainty bound, which will be discussed in Sec. 4.7.

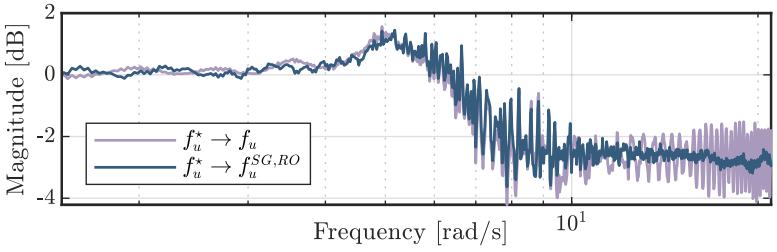

Figure 4.17: Magnitude of force-to-force mapping: comparison of $f_u^{\star} \rightarrow f_u$ mapping and $f_u^{\star} \rightarrow f_u^{SG,RO}$ (at $max(f_u^{\star}) = 20$ N).

Finally, to emphasise the effects of data post-processing techniques, ETFE (phase) comparisons are included in Fig. 4.18. At $max(f_u^{\star}) = 20$ N, the final ETFE result using raw input/output signals (before pre- and post-processing) is compared with ETFE^{SP}, where pre- and post-processing techniques have been applied. At

frequencies around 2 and 4.3 rad/s, and high-frequency asymptote, the effect of ETFE phase correction (to force the phase limit in the range of $[-180\ 0]^{\circ}$) can be noticed. Moreover, in both ETFE results, phase unwrapping is applied (where phase wrapping occurs). Finally, ETFE filtering smoothes the results over the full frequency range; however, in Fig. 4.18, the ETFE variance is decreased due to pre-processing, and ETFE filtering (post-processing).

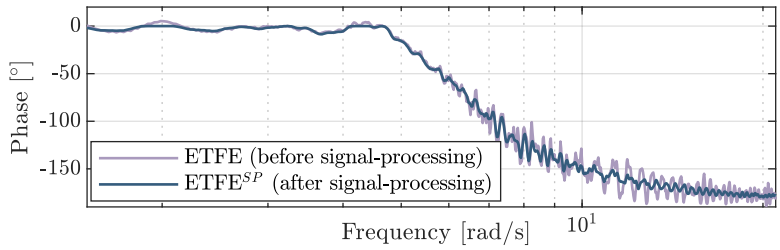

Figure 4.18: Comparison of ETFE phases ($max(f_u) = 20$ N), before and after post-processing.

4.7 Application to robust WEC control

A particularly important potential application of the multi-linear WEC modelling is to determine an adequate single nominal model and quantify the uncertainty bound from the family of models for robust control design of WECs. The different techniques for nominal model determination, with consequences on the resulting control performance, as well as the importance of uncertainty size on the conservatism of the controller approach, are detailed by [23], with an example case of employing CFD-based numerical tank experiments to obtain a representative nominal model and small uncertainty bound studied by [29].

Using the final ETFE (ETFE^{SP}) results after applying the full suite of signal processing techniques (results shown in Fig. 4.13), the uncertainty bound using the lower and upper limits of the ETFE ranges, and the corresponding nominal model (G_N^{SP}), calculated as an average of ETFE^{SP} for different input force levels, are presented in Fig. 4.19 which can be used for robust control design. To highlight the effect of data pre- and post-processing techniques on the uncertainty bound and nominal model, ETFE^{SP} and G_N^{SP} are compared with ETFE bound calculated using raw input and output signals, and the corresponding G_N. In Fig. 4.19, it is clear that the effect of pre- and post-processing produces a smoother (and likely more accurate) representative G_N^{SP}, while the bounds on ETFE^{SP} are more uniform around G_N^{SP}. Using raw data for nominal model calculations can impact the performance of the model-based controller. This is because artifacts in the data may lead to

an overestimation of the model's magnitude, according to the results of this study. Moreover, a high level of fluctuations in the nominal model obtained from row data can obscure the meaningful information.

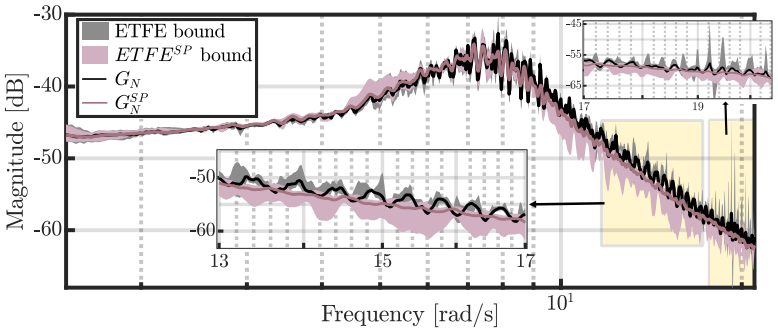

Figure 4.19: Nominal model and ETFE bounds using raw (G_N and ETFE, respectively) and processed data (G_N^{SP} and ETFE^{SP}, respectively).

4.8 Conclusions

In this study, emphasis is given to determining the most accurate non-parametric multi-linear frequency-domain model of a WEC using force-input experiments (chirp-type input force from PTO), by detecting the uncertainty and external disturbance sources in a PWT and applying appropriate data-processing techniques to exclude such artifacts from the calculated ETFEs. First, the ETFE results highlight the effect of pre-processing techniques, including SG filtering (of input and output signals) and outlier removal (from input signals). These techniques decrease the variance in ETFE magnitude and phase while retaining the original signal phase content (as shown in Figs. 4.16 and 4.17). Subsequently, the impact of post-processing activities has been highlighted (an example shown in Fig. 4.18), by decreasing the high variable ETFE and preserving the physical properties of the WEC device. The pre- and post-processing techniques return the most realistic WEC models, which can be used as adequate models for linear control designs. Furthermore, robust control can be implemented by the determination of a nominal model and quantification of uncertainty bound using multi-linear models obtained from this study. Moreover, the following conclusions are drawn from this study:

- Considering the relatively poor performance of the force tracking loop (shown in Fig. 4.2 and the results of the force-to-force mapping in Fig. 4.12), which causes excursions (phase and amplitude) between the reference force and actual force, it is important to correctly select a set of appropriate input/output signals based

on the required characteristics of the WEC model, i.e., consider *Actual force-to-motion mapping* for ETFEs characterising the hydrodynamic WEC model, and consider *Reference force-to-motion mapping* for ETFE characterising complete WEC model (including PTO).

- The contamination level at the different force levels must be considered carefully as dominancy of the contamination level (e.g. noise and outliers in small input amplitude force level), may lead to misestimation of the WEC system model. (Some quantitative results specific to the PWT under study are presented in Fig. 4.15).

- Regarding data contamination by outliers, special consideration should be taken to remove the effect. In the application of WECs, the occurrence of outliers can be due to different factors and their corresponding consequences. For example, outliers can contaminate the significant wave height (H_s) records [134, 133], mooring load measurements using load cells [135], or the output WEC power, as articulated in [136].

- In a design of a moving filter for chirp-type signals, a specific consideration should be taken for the selection of the window length, as the duration of oscillations (or distance between zero crossing points) varies nonlinearly with time.

Several limitations should be noted in this study. Data collection was constrained to an experimental campaign provided, limiting the ability to conduct additional validation tests. Further experiments, could help for accurate characterisation of contamination, for example, data recording using position laser sensors in zero input condition tests (fixed buoy position) to ensure noise characterisation. Moreover, the nonlinear behaviour appearing in the data, could not be definitively attributed to specific physical behaviors. Even though backlash was considered a candidate, it was not possible to categorise it. Extensive experimental tests for proper characterisation of data contamination, and addressing their sources is an important avenue for future research.

Acknowledgement

The authors would like to acknowledge funding by Maynooth University of a *John and Pat Hume Doctoral (WISH) Award*, for Mahdiyeh Farajvand, and Science

Foundation Ireland through the *Research Centre for Energy, Climate and Marine (MaREI)* under Grant 12/RC/2302_P2, for John Ringwood.

CRediT authorship contribution statement

Mahdiyeh Farajvand: Conceptualization, Methodology, Investigation, Formal analysis, Software, Writing -original draft, Writing - review & editing, Visualization. **Demián García-Violini:** Methodology, Formal analysis, Supervision, Writing - review & editing. **John V. Ringwood:** Conceptualization, Writing - review & editing, Supervision, Funding acquisition, Project administration.

5

Conclusions and future perspectives

The primary findings and conclusions of this thesis are summarised in Section 5.1, while potential areas for future research are discussed in Section 5.2.

5.1 Main conclusions

This thesis contributes to developing representative linear WEC models (multilinear WEC model), derived from nonlinear data obtained through high-fidelity CFD-based NWT simulations and PWT experiments. These models effectively capture potential nonlinearities and comprehensively represent the dynamics of WECs during operation, making them suitable as the foundation for model-based control strategies. A critical component of this work is the meticulous consideration of uncertainty sources inherent to each type of test and the application of data processing techniques to minimise data contamination, leading to more accurate WEC characterisations. By reducing uncertainty in the models derived from NWT and PWT experiments, this work provides more realistic representations of WEC dynamics, supporting future validation studies through more reliable comparisons between numerical and experimental models. The multilinear WEC models developed from NWT tests are used to identify parametric models, through which the dominant dynamic properties are analysed and their variations across different operating conditions are examined. Furthermore, due to their significant potential in robust WEC control applications, a nominal linear model and associated uncertainty bounds are derived from the multilinear WEC models and synthesised for

enhanced control performance. These findings are also applicable to the multilinear WEC models developed from PWT testing.

The main conclusions drawn from this research are summarised below, highlighting the key findings from the three included papers and their interconnected contributions to the field.

- **Effectiveness of data-driven WEC models**: The derivation of WEC models from both physical and high-fidelity numerical experiments using force-input tests, combined with a careful selection of input signals to cover the full frequency and amplitude range, is an effective approach for obtaining accurate linear WEC models suitable for dynamic assessment and control design. However, significant uncertainties inherent to each experiment type can critically impact model accuracy and control design. This highlights the importance of carefully identifying and mitigating these uncertainties to improve model accuracy and minimise uncertainty, thereby enhancing the effectiveness of robust WEC control.

- **Passivity violation in WEC systems**: The passivity property of WEC systems can be compromised in both physical and high-fidelity numerical experiments. For physical data, contamination—such as noise and outliers— can pose a risk to passivity. In numerical experiments, the simulation processes can introduce errors that result in non-passive system characteristics. To preserve the physical realism of WEC models, it is crucial to address these issues. In this study, passive conditions are ensured by applying a post-processing technique within the valid range of ETFE phases.

- **Dominant dynamics of linearised WEC models**: Understanding the dynamics of WEC models is crucial for guiding the progression and development of WEC technologies. The dominant dynamics of linearised WEC models under different operating conditions can be effectively tracked, with key parameters such as the resonance frequency, which can be derived from ETFE results, and the location of dominant poles, obtainable from the state-space representation of WEC systems using parametric system identification techniques like the FOAMM toolbox. Analysis of the dominant dynamics of WECs from NWT testing, compared with WAMIT data, reveals a decreasing trend in resonance frequency, indicating an increasing damping effect as the amplitude of the input force decreases (detailed in Chapter 3). This behavior has also been observed in previous studies analysing the dynamics of WEC models obtained from free-decay NWT testing [50]. A similar investigation can be conducted for ETFEs from PWT testing.

- **Contamination level prevalence across operating conditions**: The level of data contamination (for instance noise, outlier in PWT testing) at various force levels must be carefully considered, as the dominance of contamination can be particularly significant under specific operating conditions, potentially leading to misestimation of the WEC system model. Chapter 4 provides quantitative results detailing data contamination from various sources, including noise, outliers, reflection, and structural vibration, at different operating points specific to the PWT under study. These results reveal varying trends—both increasing and decreasing—in contamination levels, along with their corresponding impact on data accuracy.

- **Specific considerations in processing chirp-type signals**: Chirp signals are extensively used in this study for system identification tests in both NWT and PWT (Chapters 2 and 4) due to their ability to cover the full frequency range, which is directly linked to the system's frequency response. Additionally, chirp signals facilitate the exploration of amplitude-related nonlinearities by using multiple chirp signals at varying amplitudes, enabling the characterisation of a multi-linear WEC model—an essential step in developing a nominal linear model with defined bounds for robust WEC control.

  However, the frequency-varying nature of chirp signals requires specific considerations in their processing. For example, implementing a moving filter that adapts to the chirp's instantaneous frequency is essential for effectively mitigating artifacts within the specific window of the varying frequency of the chirp signal. The application of a BPF to chirp signal experiments (as detailed in Chapter 2) highlights the challenge of correctly initialising the filter output, which can introduce unwanted transient artifacts. To address this, Chapter 4 presents an innovative application of a moving SG filter—a low-pass filter—designed based on the nonlinearly varying zero-crossing points of the signal, which are directly linked to the duration of oscillations. This design, with a fixed filter order tailored to the characteristics of chirp signals, offers a more effective approach and should be considered in future designs of moving filters for chirp-type signals.

- **Role of data-processing in enhancing model realism**: Data processing plays a critical role in enhancing the realism of WEC models. Pre-processing techniques focus on removing artifacts from time-domain signals, ensuring the retention of the original signal's phase and amplitude while reducing variance in the resulting ETFE magnitude and phase. Post-processing, applied in the

frequency domain, is crucial for preserving the physical properties of the WEC device while reducing the variability in ETFE results. These techniques yield models that are not only realistic but also well-suited for linear robust control design, thanks to accurate nominal model characterisation and minimised uncertainty.

- **A conclusion from the thesis**: The three papers included in this thesis collectively contribute to the development of comprehensive multilinear WEC models derived from wave tank experiments, capturing potential nonlinearities during WEC operation, and providing a deeper understanding of WEC dynamics and the application of linearised models in WEC control. Paper I underscores the importance of high-fidelity CFD-based NWT experiments, highlighting the need for careful input signal design and post-processing to achieve a representative nominal model with reduced uncertainty, essential for effective robust control. Paper II builds upon this by demonstrating the utility of force-input experiments for system identification, illustrating how variations in input force amplitude influence the dominant dynamics of WEC models. Paper III addresses the practical challenges associated with physical wave tank testing, with a particular focus on data contamination and the critical role of pre- and post-processing techniques in achieving accurate, multi-linear WEC models.

  Collectively, these studies establish a robust framework for WEC model development and control design, emphasising the critical balance between model fidelity, uncertainty management, and practical considerations in both numerical and physical testing environments. The conclusions drawn from this research not only enhance the realism of WEC models but also provide valuable insights for future advancements in linear WEC control implementation.

5.2 Future perspectives

The work presented in this thesis opens up several directions for further research and investigation:

- Considering the concept of gain scheduling—a widely accepted approach for managing nonlinear system dynamics—the multilinear WEC models developed in this study can be effectively used to create an optimal set of models. By employing a fuzzy interpolation scheme, this approach combines the

simplicity of linear modeling with a smooth interpolation mechanism between different models or controllers. This results in a composite model with high fidelity across the full operational range, making it well-suited for model-based control through gain scheduling.

- Given the thesis's key contribution to ETFE calculations, which relies on the assumptions of periodic motion and linear behaviour of the WEC system, it would be beneficial to calculate total harmonic distortion. This calculation would help attribute any energy observed at non-harmonic frequencies in the output to potential nonlinearities or time-varying behaviors within the system. The use of frequency-varying chirp signals as excitation in PWT testing in this study, where the energy is distributed across a wide range of frequencies, complicates the differentiation of harmonic distortion components from the input signal. To facilitate a clearer analysis of total harmonic distortion, conducting additional experiments with purely sinusoidal signals would be advantageous. This would allow for a more straightforward identification and quantification of distortion, providing deeper insights into the system's nonlinear characteristics.

- The data collection for the study presented in Chapter 4 was constrained to an experimental campaign at Aalborg University, limiting the scope for additional validation tests. Conducting extensive experimental tests to accurately characterise data contamination and identify its sources is a crucial area for future research. For example, recording data with position laser sensors during zero-input condition tests (with the buoy in a fixed position) could provide precise noise characterisation. Moreover, the nonlinear behavior observed in the data could not be conclusively linked to specific physical phenomena. While backlash was considered a possible cause, it could not be definitively identified, warranting further investigation in future experiments.

- The identification of uncertainty and external disturbances in PWT testing (as discussed in Chapter 4) focuses on a single point-absorber WEC, where some unknown nonlinear behaviours remain. In the case of WEC arrays, the interactions between multiple devices introduce greater complexity, potentially increasing the levels of contamination and uncertainty affecting the models. This highlights the need for further research to address the unique challenges associated with uncertainty in WEC array experiments.

Bibliography

[1] European Commission, "2050 long-term strategy." https://climate.ec.europa.eu/eu-action/climate-strategies-targets/2050-long-term-strategy_en (Accessed on 4 July 2024).

[2] European Union, "Energy roadmap 2050." https://ec.europa.eu/energy/sites/ener/files/documents/2012_energy_roadmap_2050_en_0.pdf (Accessed on 4 July 2024).

[3] S. Potrč, L. Čuček, M. Martin, and Z. Kravanja, "Sustainable renewable energy supply networks optimization–the gradual transition to a renewable energy system within the European Union by 2050," *Renewable and Sustainable Energy Reviews*, vol. 146, p. 111186, 2021.

[4] European Parliament, "Energy supply and security." https://www.europarl.europa.eu/RegData/etudes/BRIE/2018/630275/EPRS_BRI(2018)630275_EN.pdf (Accessed on 4 July 2024).

[5] European Commission, "Offshore renewable energy." https://energy.ec.europa.eu/topics/renewable-energy/offshore-renewable-energy_en (Accessed on 4 July 2024).

[6] G. Mork, S. Barstow, A. Kabuth, and M. T. Pontes, "Assessing the global wave energy potential," in *International Conference on Offshore Mechanics and Arctic Engineering*, vol. 49118, pp. 447–454, Shanghai, 2010.

[7] K. Gunn and C. Stock-Williams, "Quantifying the global wave power resource," *Renewable Energy*, vol. 44, pp. 296–304, 2012.

[8] B. Reguero, I. Losada, and F. Méndez, "A global wave power resource and its seasonal, interannual and long-term variability," *Applied Energy*, vol. 148, pp. 366–380, 2015.

[9] L. Rusu and E. Rusu, "Evaluation of the worldwide wave energy distribution based on era5 data and altimeter measurements," *Energies*, vol. 14, no. 2, p. 394, 2021.

[10] European Space Agency, "Climate Change Initiative for Sea State: Project Website and Data Access." https://climate.esa.int/en/projects/sea-state/. (Accessed on 4 July 2024).

[11] J. Cruz, *Ocean wave energy: current status and future prespectives*. Springer Science & Business Media, 2007.

[12] B. Drew, A. R. Plummer, and M. N. Sahinkaya, “A review of wave energy converter technology,” in *Proceedings of the Institution of Mechanical Engineers, Part A: Journal of Power and Energy*, vol. 223, pp. 887–902, London, 2009.

[13] B. Guo, T. Wang, S. Jin, S. Duan, K. Yang, and Y. Zhao, “A review of point absorber wave energy converters,” *Journal of Marine Science and Engineering*, vol. 10, no. 10, p. 1534, 2022.

[14] Y. Li and Y.-H. Yu, “A synthesis of numerical methods for modeling wave energy converter-point absorbers,” *Renewable and Sustainable Energy Reviews*, vol. 16, no. 6, pp. 4352–4364, 2012.

[15] E. Al Shami, R. Zhang, and X. Wang, “Point absorber wave energy harvesters: A review of recent developments,” *Energies*, vol. 12, no. 1, p. 47, 2018.

[16] J. V. Ringwood, “Wave energy control: status and perspectives 2020,” *IFAC-PapersOnLine*, vol. 53, no. 2, pp. 12271–12282, 2020.

[17] K. Budar and J. Falnes, “A resonant point absorber of ocean-wave power,” *Nature*, vol. 256, no. 5517, pp. 478–479, 1975.

[18] R. H. Hansen, “Design and control of the powertake-off system for a wave energy converter with multiple absorbers,” *Department of Energy Technology, Aalborg University*, 2013.

[19] J. Hals, J. Falnes, and T. Moan, “Constrained optimal control of a heaving buoy wave-energy converter,” *Journal of Offshore Mechanics and Arctic Engineering*, vol. 133, no. 1, p. 011401, 2010.

[20] F. Fusco and J. V. Ringwood, “A simple and effective real-time controller for wave energy converters,” *IEEE Transactions on Sustainable Energy*, vol. 4, no. 1, pp. 21–30, 2012.

[21] D. García-Violini, Y. Peña-Sanchez, N. Faedo, and J. V. Ringwood, “An energy-maximising linear time invariant controller (LiTe-Con) for wave energy devices,” *IEEE Transactions on Sustainable Energy*, vol. 11, no. 4, pp. 2713–2721, 2020.

[22] N. Faedo, G. Scarciotti, A. Astolfi, and J. V. Ringwood, “Energy-maximising control of wave energy converters using a moment-domain representation,” *Control Engineering Practice*, vol. 81, pp. 85–96, 2018.

[23] D. Garcia-Violini and J. V. Ringwood, “Energy maximising robust control for spectral and pseudospectral methods with application to wave energy systems,” *International Journal of Control*, vol. 94, no. 4, pp. 1102–1113, 2021.

[24] N. Faedo, S. Olaya, and J. V. Ringwood, “Optimal control, MPC and MPC-like algorithms for wave energy systems: An overview,” *IFAC Journal of Systems and Control*, vol. 1, pp. 37–56, 2017.

[25] N. Tom and R. W. Yeung, "Nonlinear model predictive control applied to a generic ocean-wave energy extractor," *Journal of Offshore Mechanics and Arctic Engineering*, vol. 136, no. 4, 2014.

[26] N. Faedo, Y. Peña-Sanchez, and J. V. Ringwood, "Finite-order hydrodynamic model determination for wave energy applications using moment-matching," *Ocean Engineering*, vol. 163, pp. 251–263, 2018.

[27] C. Windt, N. Faedo, M. Penalba, F. Dias, and J. V. Ringwood, "Reactive control of wave energy devices–the modelling paradox," *Applied Ocean Research,*, vol. 109, p. 102574, 2021.

[28] A. Mérigaud and J. V. Ringwood, "Improving the computational performance of nonlinear pseudospectral control of wave energy converters," *IEEE Transactions on Sustainable Energy,*, vol. 9, no. 3, pp. 1419–1426, 2017.

[29] M. Farajvand, V. Grazioso, D. García-Violini, and J. V. Ringwood, "Uncertainty estimation in wave energy systems with applications in robust energy maximising control," *Renewable Energy,*, vol. 203, pp. 194–204, 2022.

[30] J. V. Ringwood, A. Mérigaud, N. Faedo, and F. Fusco, "An analytical and numerical sensitivity and robustness analysis of wave energy control systems," *IEEE Trans. on Control Systems Technology,*, vol. 28, no. 4, pp. 1337–1348, 2019.

[31] H. A. Said, D. García-Violini, N. Faedo, and J. V. Ringwood, "On the ratio of reactive to active power in wave energy converter control," *IEEE Open Journal of Control Systems*, vol. 3, pp. 14–31, 2023.

[32] M. Farajvand, D. García-Violini, and J. V. Ringwood, "Non-parametric multi-linear frequency-domain modelling of a wave energy device from experimental data," *Available at SSRN 4776686*.

[33] W. Qiu, J. S. Junior, D. Lee, H. Lie, V. Magarovskii, T. Mikami, J.-M. Rousset, S. Sphaier, L. Tao, and X. Wang, "Uncertainties related to predictions of loads and responses for ocean and offshore structures," *Ocean Engineering*, vol. 86, pp. 58–67, 2014.

[34] C. Windt, J. Davidson, E. J. Ransley, D. Greaves, M. Jakobsen, M. Kramer, and J. V. Ringwood, "Validation of a CFD-based numerical wave tank model for the power production assessment of the wavestar ocean wave energy converter," *Renewable Energy,*, vol. 146, pp. 2499–2516, 2020.

[35] W. Wang, M. Wu, J. Palm, and C. Eskilsson, "Estimation of numerical uncertainty in computational fluid dynamics simulations of a passively controlled wave energy converter," *Proceedings of the Institution of Mechanical Engineers, Part M: Journal of Engineering for the Maritime Environment,*, vol. 232, no. 1, pp. 71–84, 2018.

[36] A. Babarit, J. Hals, M. J. Muliawan, A. Kurniawan, T. Moan, and J. Krokstad, "Numerical benchmarking study of a selection of wave energy converters," *Renewable Energy*, vol. 41, pp. 44–63, 2012.

[37] M. Durand, A. Babarit, B. Pettinotti, O. Quillard, J. Toularastel, and A. Clément, "Experimental validation of the performances of the searev wave energy converter with real time latching control," in *The 7th European Wave and Tidal Energy Conference (EWTEC), Porto*, 2007.

[38] J. Mas-Soler and A. N. Simos, "A Bayesian wave inference method accounting for nonlinearity related inaccuracies in motion RAOs," *Applied Ocean Research*, vol. 99, p. 102125, 2020.

[39] D. García-Violini, Y. Peña-Sanchez, N. Faedo, C. Windt, F. Ferri, and J. V. Ringwood, "Experimental implementation and validation of a broadband LTI energy-maximizing control strategy for the Wavestar device," *IEEE Transactions on Control Systems Technology*, vol. 29, no. 6, pp. 2609–2621, 2021.

[40] G. Olbert and M. Abdel-Maksoud, "High-fidelity modelling of lift-based wave energy converters in a numerical wave tank," *Applied Energy*, vol. 347, p. 121460, 2023.

[41] G. Bacelli, R. G. Coe, D. Patterson, and D. Wilson, "System identification of a heaving point absorber: Design of experiment and device modeling," *Energies,*, vol. 10, no. 4, p. 472, 2017.

[42] S. Giorgi, J. Davidson, M. Jakobsen, M. Kramer, and J. V. Ringwood, "Identification of dynamic models for a wave energy converter from experimental data," *Ocean Engineering*, vol. 183, pp. 426–436, 2019.

[43] E. Pasta, N. Faedo, G. Mattiazzo, and J. V. Ringwood, "Towards data-driven and data-based control of wave energy systems: Classification, overview, and critical assessment," *Renewable and Sustainable Energy Reviews*, vol. 188, p. 113877, 2023.

[44] W. Sheng, "Wave energy conversion and hydrodynamics modelling technologies: A review," *Renewable and Sustainable Energy Reviews*, vol. 109, pp. 482–498, 2019.

[45] M. Penalba and J. V. Ringwood, "A review of wave-to-wire models for wave energy converters," *Energies*, vol. 9, no. 7, p. 506, 2016.

[46] B. Guo and J. V. Ringwood, "Geometric optimisation of wave energy conversion devices: A survey," *Applied Energy*, vol. 297, p. 117100, 2021.

[47] L. Papillon, R. Costello, and J. V. Ringwood, "Boundary element and integral methods in potential flow theory: A review with a focus on wave energy applications," *Journal of Ocean Engineering and Marine Energy*, vol. 6, no. 3, pp. 303–337, 2020.

[48] C. Windt, J. Davidson, and J. V. Ringwood, "High-fidelity numerical modelling of ocean wave energy systems: A review of computational fluid dynamics-based numerical wave tanks," *Renewable and Sustainable Energy Reviews,*, vol. 93, pp. 610–630, 2018.

[49] J. M. Domínguez, A. J. Crespo, M. Hall, C. Altomare, M. Wu, V. Stratigaki, P. Troch, L. Cappietti, and M. Gómez-Gesteira, "Sph simulation of floating structures with moorings," *Coastal Engineering*, vol. 153, p. 103560, 2019.

[50] J. Davidson, S. Giorgi, and J. V. Ringwood, "Linear parametric hydrodynamic models for ocean wave energy converters identified from numerical wave tank experiments," *Ocean Engineering,*, vol. 103, pp. 31–39, 2015.

[51] S. A. Hughes, *Physical models and laboratory techniques in coastal engineering*, vol. 7. World Scientific, 1993.

[52] W. Chen, I. Dolguntseva, A. Savin, Y. Zhang, W. Li, O. Svensson, and M. Leijon, "Numerical modelling of a point-absorbing wave energy converter in irregular and extreme waves," *Applied Ocean Research*, vol. 63, pp. 90–105, 2017.

[53] E. Katsidoniotaki, Z. Shahroozi, C. Eskilsson, J. Palm, J. Engström, and M. Göteman, "Validation of a CFD model for wave energy system dynamics in extreme waves," *Ocean Engineering*, vol. 268, p. 113320, 2023.

[54] J. Palm, C. Eskilsson, G. M. Paredes, and L. Bergdahl, "Coupled mooring analysis for floating wave energy converters using CFD: Formulation and validation," *International Journal of Marine Energy*, vol. 16, pp. 83–99, 2016.

[55] P. Schmitt and B. Elsaesser, "On the use of OpenFOAM to model oscillating wave surge converters," *Ocean Engineering*, vol. 108, pp. 98–104, 2015.

[56] D. García-Violini, Y. Peña-Sanchez, N. Faedo, F. Bianchi, and J. V. Ringwood, "A model invalidation procedure for wave energy converters with experimental assessment and implications for control," *Control Engineering Practice*, vol. 143, p. 105778, 2024.

[57] Wavestar Energy. `http://wavestarenergy.com/` (Accessed on 5 Feb 2022).

[58] W. Sheng, R. Alcorn, and T. Lewis, "Physical modelling of wave energy converters," *Ocean Engineering*, vol. 84, pp. 29–36, 2014.

[59] T. Pérez and T. Fossen, "Time-vs. frequency-domain identification of parametric radiation force models for marine structures at zero speed," *Modeling, Identification and Control,*, vol. 29, no. 1, pp. 1–19, 2008.

[60] T. Perez and T. I. Fossen, "Practical aspects of frequency-domain identification of dynamic models of marine structures from hydrodynamic data," *Ocean Engineering,*, vol. 38, no. 2-3, pp. 426–435, 2011.

[61] J. Falnes, *Ocean waves and oscillating systems: linear interactions including wave-energy extraction*. Cambridge Univ. Press, 2002.

[62] H. K. Khalil, *Nonlinear control*. Pearson Higher Ed, 2014.

[63] D. García-Violini, M. Farajvand, C. Windt, V. Grazioso, and J. V. Ringwood, "Passivity considerations in robust spectral-based controllers for wave energy converters," in *2021 XIX Workshop on Information Processing and Control (RPIC)*, pp. 1–6, San Juan, Argentina, 2021.

[64] J. Davidson, S. Giorgi, and J. V. Ringwood, "Identification of wave energy device models from numerical wave tank data—part 1: Numerical wave tank identification tests," *IEEE Transactions on Sustainable Energy*, vol. 7, no. 3, pp. 1012–1019, 2016.

[65] K. M. Prabhu, *Window functions and their applications in signal processing*. Taylor & Francis, 2014.

[66] L. Ljung, "Perspectives on system identification," *Annual Reviews in Control*, vol. 34, no. 1, pp. 1–12, 2010.

[67] Y. Pena-Sanchez, N. Faedo, M. Penalba, G. Giuseppe, A. Mérigaud, C. Windt, D. G. Violini, W. LiGuo, and J. Ringwood, "Finite-order hydrodynamic approximation by moment-matching (FOAMM) toolbox for wave energy applications," in *European Wave and Tidal Energy Conference Proceedings (EWTEC),Naples*, pp. 1448–1:1448–9, 2019.

[68] M. Farajvand, D. García-Violini, and J. V. Ringwood, "Representative linearised models for a wave energy converter using various levels of force excitation," *Ocean Engineering*, vol. 270, p. 113635, 2023.

[69] N. Faedo, G. Mattiazzo, and J. V. Ringwood, "Robust energy-maximising control of wave energy systems under input uncertainty," in *Proc. European Control Conference (ECC 2022)*, pp. 614–619, London, 2022.

[70] M. Atlar, R. Anzbock, M. Leer-Andersen, J. Jang, H. Kai, and E. Carillo, "Specialist committee on surface treatment, final report and recommendations to the 26th ITTC," in *26th International Towing Tank Conference (ITTC)*, Newcastle, 2011.

[71] J. Orphin, J.-R. Nader, and I. Penesis, "Uncertainty analysis of a wec model test experiment," *Renewable Energy*, vol. 168, pp. 216–233, 2021.

[72] B. Robertson, H. Bailey, and B. Buckham, "Resource assessment parameterization impact on wave energy converter power production and mooring loads," *Applied Energy*, vol. 244, pp. 1–15, 2019.

[73] B. Yildirim and G. E. Karniadakis, "Stochastic simulations of ocean waves: An uncertainty quantification study," *Ocean Modelling*, vol. 86, pp. 15–35, 2015.

[74] T. IEC, "62600; wave, tidal and other water current converters—part 103: Guidelines for the early stage development of wave energy converters—best practices and recommended procedures for the testing of pre-prototype devices," *International Electrotechnical Commission: Geneva, Switzerland*, 2018.

[75] D. R. Noble, S. Draycott, T. A. Davey, and T. Bruce, "Design diagrams for wavelength discrepancy in tank testing with inconsistently scaled intermediate water depth," *International Journal of Marine Energy*, vol. 18, pp. 109–113, 2017.

[76] G. Giannini, I. Temiz, P. Rosa-Santos, Z. Shahroozi, V. Ramos, M. Göteman, J. Engström, S. Day, and F. Taveira-Pinto, "Wave energy converter power take-off system scaling and physical modelling," *Journal of Marine Science and Engineering*, vol. 8, no. 9, p. 632, 2020.

[77] International Towing Tank Conference, “Uncertainty analysis, instrument calibration.” Available online: https://www.ittc.info/media/7979/75-01-03-01.pdf (accessed on 24 March 2020).

[78] International Towing Tank Conference, “Uncertainty analysis for a wave energy converter.” Available online: https://www.ittc.info/media/8135/75-02-07-0312.pdf (accessed on 24 March 2023).

[79] Z. Shahroozi, M. Göteman, and J. Engström, “Experimental investigation of a point-absorber wave energy converter response in different wave-type representations of extreme sea states,” *Ocean Engineering*, vol. 248, p. 110693, 2022.

[80] M. L. Celesti, F. Ferri, and N. Faedo, “Experimental modelling uncertainty quantification for a prototype wave energy converter,” in *2024 European Control Conference (ECC)*, pp. 1546–1551, Stockholm, 2024.

[81] A. Savitzky and M. J. Golay, “Smoothing and differentiation of data by simplified least squares procedures.,” *Analytical Chemistry*, vol. 36, no. 8, pp. 1627–1639, 1964.

[82] R. W. Schafer, “On the frequency-domain properties of savitzky-Golay filters,” in *2011 Digital Signal Processing and Signal Processing Education Meeting (DSP/SPE)*, pp. 54–59, Sedona, AZ, USA, 2011.

[83] G. Buzzi-Ferraris and F. Manenti, “Outlier detection in large data sets,” *Computers & Chemical Engineering*, vol. 35, no. 2, pp. 388–390, 2011.

[84] P. Shrestha, Y. Park, H. Kwon, and C.-G. Kim, “Error outlier with weighted median absolute deviation threshold algorithm and FBG sensor based impact localization on composite wing structure,” *Composite Structures*, vol. 180, pp. 412–419, 2017.

[85] Y. Rolain, J. Schoukens, and G. Vandersteen, “Signal reconstruction for nonequidistant finite length sample sets: a "KIS" approach,” in *IMTC/98 Conference Proceedings. IEEE Instrumentation and Measurement Technology Conference. Where Instrumentation is Going (Cat. No. 98CH36222)*, vol. 2, pp. 1217–1222, St. Paul, MN, USA, 1998.

[86] M. Kahrs and K. Brandenburg, *Applications of digital signal processing to audio and acoustics*. Springer Science & Business Media, 1998.

[87] W. E. Cummins, “The impulse response function and ship motions,” *Schiffstechnik,*, vol. 47, pp. 101–109, 1962.

[88] M. Penalba and J. V. Ringwood, “A high-fidelity wave-to-wire model for wave energy converters,” *Renewable Energy,*, vol. 134, pp. 367–378, 2019.

[89] H. A. Wolgamot and C. J. Fitzgerald, “Nonlinear hydrodynamic and real fluid effects on wave energy converters,” *Proceedings of the Institution of Mechanical Engineers, Part A: Journal of Power and Energy*, vol. 229, no. 7, pp. 772–794, 2015.

[90] M. Penalba, G. Giorgi, and J. V. Ringwood, "Mathematical modelling of wave energy converters: A review of nonlinear approaches," *Renewable and Sustainable Energy Reviews*, vol. 78, pp. 1188–1207, 2017.

[91] C. Windt, N. Faedo, D. García-Violini, Y. Peña-Sanchez, J. Davidson, F. Ferri, and J. V. Ringwood, "Validation of a CFD-based numerical wave tank model of the 1/20th scale wavestar wave energy converter," *Fluids,*, vol. 5, no. 3, p. 112, 2020.

[92] M. Richter, M. E. Magana, O. Sawodny, and T. K. Brekken, "Nonlinear model predictive control of a point absorber wave energy converter," *IEEE Transactions on Sustainable Energy,*, vol. 4, no. 1, pp. 118–126, 2012.

[93] G. Bacelli, R. Genest, and J. V. Ringwood, "Nonlinear control of flap-type wave energy converter with a non-ideal power take-off system," *Annual Reviews in Control*, vol. 40, pp. 116–126, 2015.

[94] M. Farajvand, D. García-Violini, C. Windt, V. Grazioso, and J. Ringwood, "Quantifying hydrodynamic model uncertainty for robust control of wave energy devices," in *14th European Wave and Tidal Energy Conference (EWTEC)*, pp. 2251–1:2251–10, Plymouth, 2021.

[95] E. M. Navarro-López and E. Licéaga-Castro, "Combining passivity and classical frequency-domain methods: An insight into decentralised control," *Applied Mathematics and Computation,*, vol. 215, no. 12, pp. 4426–4438, 2010.

[96] J. Na, G. Li, B. Wang, G. Herrmann, and S. Zhan, "Robust optimal control of wave energy converters based on adaptive dynamic programming," *IEEE Transactions on Sustainable Energy,*, vol. 10, no. 2, pp. 961–970, 2018.

[97] G. M. Paredes, C. Eskilsson, and J. P. Kofoed, "Uncertainty quantification of the dynamics of a wave energy converter," in *MARINE 2019-VIII International Conference on Computational Methods in Marine Engineering*, pp. 157–168, Göteborg, Sweden, 2019.

[98] CFD DIrect, "OpenFOAM." `https://www.openfoam.com/`, 2022. Accessed online: 14-Jun-2022.

[99] M. Schroeder, "Synthesis of low-peak-factor signals and binary sequences with low autocorrelation (Corresp.)," *IEEE Transactions on Information Theory,*, vol. 16, no. 1, pp. 85–89, 1970.

[100] R. Atan, J. Goggins, and S. Nash, "A detailed assessment of the wave energy resource at the atlantic marine energy test site," *Energies,*, vol. 9, no. 11, p. 967, 2016.

[101] V. Heller, "Scale effects in physical hydraulic engineering models," *Journal of Hydraulic Research,*, vol. 49, no. 3, pp. 293–306, 2011.

[102] A. Merigaud, J.-C. Gilloteaux, and J. V. Ringwood, "A nonlinear extension for linear boundary element methods in wave energy device modelling," in *International*

Conference on Offshore Mechanics and Arctic Engineering, vol. 44915, pp. 615–621, American Society of Mechanical Engineers, Rio de Janeiro, Brazil, 2012.

[103] L. Letournel, P. Ferrant, A. Babarit, G. Ducrozet, J. C. Harris, M. Benoit, and E. Dombre, "Comparison of fully nonlinear and weakly nonlinear potential flow solvers for the study of wave energy converters undergoing large amplitude motions," in *International Conference on Offshore Mechanics and Arctic Engineering*, vol. 45547, p. V09BT09A002, American Society of Mechanical Engineers, San Francisco, California, USA, 2014.

[104] A. l. Babarit, H. Mouslim, A. Cle´ ment, and P. Laporte-Weywada, "On the numerical modelling of the non linear behaviour of a wave energy converter," in *International Conference on Offshore Mechanics and Arctic Engineering*, vol. 43444, pp. 1045–1053, Honolulu, Hawaii, USA, 2009.

[105] C. Windt, J. Davidson, P. Schmitt, and J. V. Ringwood, "On the assessment of numerical wave makers in CFD simulations," *Journal of Marine Science and Engineering,*, vol. 7, no. 2, p. 47, 2019.

[106] J. A. Armesto, R. Guanche, A. Iturrioz, C. Vidal, and I. J. Losada, "Identification of state-space coefficients for oscillating water columns using temporal series," *Ocean Engineering,*, vol. 79, pp. 43–49, 2014.

[107] T. F. Ogilvie, "Recent progress toward the understanding and prediction of ship motions," in *5th Symp. on Naval Hydr.*, vol. 1, pp. 2–5, Bergen, 1964.

[108] Wamit Inc, "WAMIT User Manual." `http://tinyw.in/7u4T`, 2022. (Accessed online: 2022-04-11).

[109] A. Babarit and G. Delhommeau, "Theoretical and numerical aspects of the open source BEM solver NEMOH," in *11th European Wave and Tidal Energy Conference, Nantes, France (EWTEC2015)*, 2015.

[110] Q.-G. Wang, Z. Zhang, K. J. Astrom, Y. Zhang, and Y. Zhang, "Guaranteed dominant pole placement with PID controllers," *IFAC Proceedings Volumes,*, vol. 41, no. 2, pp. 5842–5845, 2008.

[111] N. N. Nedić, S. L. Prodanović, and L. M. Dubonjić, "Decoupling control of tito system supported by dominant pole placement method," *Facta Universitatis. Series: Mechanical Engineering*, vol. 15, no. 2, pp. 245–256, 2017.

[112] R. C. Dorf and R. H. Bishop, *Modern control systems*. Pearson Prentice Hall, 2008.

[113] G. M. Terra, W. J. van de Berg, and L. R. Maas, "Experimental verification of Lorentz' linearization procedure for quadratic friction," *Fluid Dynamics Research,*, vol. 36, no. 3, p. 175, 2005.

[114] D. J. Leith and W. E. Leithead, "Survey of gain-scheduling analysis and design," *International Journal of Control,*, vol. 73, no. 11, pp. 1001–1025, 2000.

[115] F. Fusco and J. V. Ringwood, "Suboptimal causal reactive control of wave energy converters using a second order system model," in *The 21st Intl. Offshore and Polar Eng. Conf., Hawaii*, ISOPE, 2011.

[116] J. Orphin, J.-R. Nader, I. Penesis, D. Howe, *et al.*, "Experimental uncertainty analysis of an OWC wave energy converter," in *Proceedings of 12th European Wave and Tidal Energy Conference (EWTEC), Cork*, 2017.

[117] C. Eskilsson, W. Wang, M. Wu, and J. Palm, "Estimation of numerical uncertainty in CFD simulations of a passivley controlled wave energy converter," *Proceedings of the Institution of Mechanical Engineers, Part M: Journal of Engineering for the Maritime Environment*, vol. 232, pp. 71–84, 2017.

[118] M. Farajvand, D. García-Violini, C. Windt, V. Grazioso, and J. V. Ringwood, "Quantifying hydrodynamic model uncertainty for robust control of wave energy devices," in *The 14th European Wave and Tidal Energy Conference (EWTEC), Plymouth*, Plymouth, 2021.

[119] W. H. Press and S. A. Teukolsky, "Savitzky-Golay smoothing filters," *Computers in Physics*, vol. 4, no. 6, pp. 669–672, 1990.

[120] M. Schmid, D. Rath, and U. Diebold, "Why and how Savitzky–Golay filters should be replaced," *ACS Measurement Science Au*, vol. 2, no. 2, pp. 185–196, 2022.

[121] W. Dai, I. Selesnick, J.-R. Rizzo, J. Rucker, and T. Hudson, "A nonlinear generalization of the Savitzky-Golay filter and the quantitative analysis of saccades," *Journal of Vision*, vol. 17, no. 9, pp. 10–10, 2017.

[122] D. Wagg, G. Karpodinis, and S. Bishop, "An experimental study of the impulse response of a vibro-impacting cantilever beam," *Journal of Sound and Vibration*, vol. 228, no. 2, pp. 243–264, 1999.

[123] C.-J. Lin, H.-T. Yau, and Y.-C. Tian, "Identification and compensation of nonlinear friction characteristics and precision control for a linear motor stage," *IEEE/ASME Transactions on Mechatronics*, vol. 18, no. 4, pp. 1385–1396, 2012.

[124] M. Farajvand, D. Garcıa-Violini, and J. V. Ringwood, "Characterising uncertainty and external disturbance sources in wave tank experiments for wave energy converter modelling," in *Proc. 15th European Wave and Tidal Energy Conference*, vol. Paper 376, pp. pp 1–10, Bilbao, Sept. 2023.

[125] M. Kramer, L. Marquis, and P. Frigaard, "Performance evaluation of the Wavestar prototype," in *The 9th European Wave and Tidal Energy Conference (EWTEC), Southampton, UK*, 2011.

[126] J. Wang, S. Su, and Z. Chen, "Parameter estimation of chirp signal under low SNR," *Science China. Information Sciences*, vol. 58, no. 2, pp. 1–13, 2015.

[127] R. W. Schafer, "What is a Savitzky-Golay filter?[lecture notes]," *IEEE Signal Processing Magazine*, vol. 28, no. 4, pp. 111–117, 2011.

[128] S. de Waele and P. M. Broersen, "Error measures for resampled irregular data," *IEEE Transactions on Instrumentation and Measurement*, vol. 49, no. 2, pp. 216–222, 2000.

[129] F. N. Fritsch, "Piecewise cubic hermite interpolation package. final specifications," tech. rep., Lawrence Livermore National Lab.(LLNL), Livermore, CA (United States), 1982.

[130] R. Pintelon and J. Schoukens, *System Identification: A Frequency Domain Approach*. John Wiley & Sons, 2012.

[131] H. Akaike, "Fitting autoregressive models for prediction," in *Selected Papers of Hirotugu Akaike*, pp. 131–135, Springer, 1969.

[132] M. Mauerer, A. Tüysüz, and J. W. Kolar, "Distortion analysis of low-thd/high-bandwidth gan/sic class-d amplifier power stages," in *2015 IEEE Energy Conversion Congress and Exposition (ECCE)*, pp. 2563–2571, Montreal, QC, Canada, 2015.

[133] E. B. Mackay, A. S. Bahaj, and P. G. Challenor, "Uncertainty in wave energy resource assessment. Part 2: Variability and predictability," *Renewable Energy*, vol. 35, no. 8, pp. 1809–1819, 2010.

[134] K. Mahmoodi and H. Ghassemi, "Outlier detection in ocean wave measurements by using unsupervised data mining methods," *Polish Maritime Research*, vol. 25, no. 1, pp. 44–50, 2018.

[135] M. Ponomarev, L. Johanning, and D. Parish, "Enhancing precision and reliability of tri-axial load cells for mooring load measurements," in *Proceedings of the 3rd International Conference on Ocean Energy*, vol. 6, Bilbao, 2010.

[136] G. Reikard, B. Robertson, and J.-R. Bidlot, "Wave energy worldwide: Simulating wave farms, forecasting, and calculating reserves," *International Journal of Marine Energy*, vol. 17, pp. 156–185, 2017.